



HAL
open science

Etude de dispositifs piézoélectriques et de leurs interfaces pour la récupération d'énergie

Ya Shan Shih

► **To cite this version:**

Ya Shan Shih. Etude de dispositifs piézoélectriques et de leurs interfaces pour la récupération d'énergie. Energie électrique. Université Paris Saclay (COMUE); National Taiwan University (Taipei), 2018. Français. NNT : 2018SACLN007 . tel-02168673

HAL Id: tel-02168673

<https://theses.hal.science/tel-02168673>

Submitted on 29 Jun 2019

HAL is a multi-disciplinary open access archive for the deposit and dissemination of scientific research documents, whether they are published or not. The documents may come from teaching and research institutions in France or abroad, or from public or private research centers.

L'archive ouverte pluridisciplinaire **HAL**, est destinée au dépôt et à la diffusion de documents scientifiques de niveau recherche, publiés ou non, émanant des établissements d'enseignement et de recherche français ou étrangers, des laboratoires publics ou privés.



Designs for MEMS and Bulk-Sized Piezoelectric Energy Harvesting Systems for Ultra Low Power and Bandwidth Extension

Thèse de doctorat de l'Université Paris-Saclay
préparée à l'ENS Cachan

École doctorale n°000 Electrical, Optical, Bio-Physics and
Engineering EOBE
Spécialité de doctorat : Génie Electrique

Thèse présentée et soutenue à Taipei, le 12 janvier 2018, par

Ya-Shan SHIH

Composition du Jury :

Chih Kung Lee	
Distinguished Professeur, National Taiwan University	Président
Wei-Hsin Liao	
Professeur, The Chinese University of Hong Kong	Rapporteur
Adrien Badel	
Maître de conférences, Université Savoie Mont-Blanc (SYMME)	Rapporteur
Mickael Lallart	
Maître de conférences, INSA Lyon (LGEF)	Examineur
Dejan Vasic	
Maître de conférences, Université de Cergy-Pontoise (SATIE)	Directeur de thèse
Wen-Jong Wu	
Professeur, National Taiwan University	Directeur de thèse
François Costa	
Professeur, Université Paris-Est (SATIE)	Co-Directeur de thèse
Yi-Chung Shu	
Distinguished Professor, National Taiwan University	Examineur

Titre : Etude de Systems de Recuperation d'Énergie de très faible puissance et large bande

Mots clés : piézoélectricité, récupération d'énergie, convertisseur très faible puissance, extension de la bande passante

Résumé : La récupération d'énergie ambiante permet d'alimenter de manière autonome des systèmes de petite taille tels que des neuds de capteurs ou des objets connectés à internet (IoT) en remplacement des batteries. Les sources d'énergie ambiante sont par exemple, l'énergie solaire, le gradient thermique, les forces mécaniques, le rayonnement électromagnétique et la pile microbienne. Les matériaux piézoélectriques permettent de valoriser électriquement l'énergie mécanique de vibration en la convertissant directement en énergie électrique. Les niveaux de puissance assez faible (de quelques μW au mW) ont amené à développer des interfaces électriques de récupération afin d'extraire le maximum d'énergie en améliorant le couplage électromécanique.

Dans ce travail, nous nous intéressons à l'amélioration de dispositif de récupération d'énergie. Deux aspects sont abordés : dans un premier temps l'étude d'un commutateur hybride synchrone électrique-mécanique est faite pour remplacer le transistor MOSFET couramment utilisé, afin de réduire sa consommation d'énergie ; dans un deuxième temps, un travail est mené sur une nouvelle structure mécanique à base de poutres reliées entre elle par des forces de répulsion magnétique. La structure obtenue par cet ensemble de poutres et de type non-linéaire à plusieurs degrés de liberté (MDOF) ce qui permet augmenter la bande passante.

Title : Designs for MEMS and Bulk-Sized Piezoelectric Energy Harvesting Systems for Ultra Low Power and Bandwidth Extension

Keywords : Energy harvesting system, piezoelectric cantilever beam, beam arrays, bandwidth expansion, synchronized switch, low power.

The future trend of Internet of Things (IoT) is bringing energy harvesting in to the core technique due to its requirement of self-power supplying. For best customer interface and eco-friendly issues, additional sensing systems are to be designed small, wireless and self-powering. Energy harvesting provides a way to realize the wireless self-powered system, it enables the device itself to obtain its own energy from their environment. Solar energy, thermal gradient, mechanical forces, are some commonly seen methods to obtain energy from the environment. The piezoelectric energy harvester is chosen to harvest vibrational energy in this study.

In this work, a simple model of the original electrical smart switch driven under ultra-low power is proposed. By using the miniature device to drive the smart switch, the efficiency when low power is provided was examined. To construct an energy harvesting system in a more complete aspect, two newly proposed methods are as below: First, the hybrid-electrical-mechanical switches were utilized to replace the commonly seen electrical smart switches, to reduce its energy consumption such as threshold loss. Secondly, we designed a new mechanical structure for the cantilever array by connecting the beams using magnetic repelling force. In this way, the beams within the array were connected physically, forming a nonlinear multi-degree of freedom (MDOF)-like result.

CONTENTS

誌謝 Acknowledgement	Error! Bookmark not defined.
中文摘要.....	Error! Bookmark not defined.
ABSTRACT.....	Error! Bookmark not defined.
CONTENTS.....	iv
LIST OF FIGURES.....	viii
LIST OF TABLES.....	xii
Chapter 1. Introduction	1
1.2 The Energy Harvesters	6
1.2.1 Radioactive Harvesters	8
1.2.2 Kinetic Energy Harvesters	11
1.2.3 Modeling of Cantilever-Based Energy Harvester	15
1.3 Harvesting with a Broader Bandwidth.....	17
1.3.1 Beam arrays.....	18
1.3.2 Stoppers.....	19
1.3.3 Bistable Structures	20
1.3.4. MDOF structures	23
1.3.5 Up Conversion	28
1.3.6 Active Resonance tuning.....	29
1.4 The Interfacing Circuits	31
1.4.1 Theoretical Modeling of the Interfacing Circuits	35
1.4.2 Autonomous Switches for Self-Powered Systems.....	39

1.4.3 Multiple Beam Circuitry	43
1.5 Dissertation Organization.....	44
Chapter 2. Electric Circuit Losses: Modeling of a Smart Switch Driven in Low	
Voltage	46
2.1 Power Provided with Micro PEH Device.....	46
2.2 The Circuit Loss	49
2.2.1 The Rectifying Loss	49
2.2.2 The Smart Switch Loss	51
2.3 The Loss Experiment.....	60
2.3.1 Driven with voltage too low	60
2.3.2 Driven with voltage in between	61
2.3.3 Driven with enough voltage.....	63
2.4 Discussion	65
Chapter 3. Hybrid Switch on SSH Methods	68
3.1 Design Concepts.....	68
3.1.1 Reed switch introduction	68
3.1.2 Reed switch replacement on SSH techniques	70
3.1.3 Resolving the chatter: snubbers (de-bouncers)	73
3.2 Energy Loss Due to Switching Phase Difference	77
3.3 Experiment and Results.....	81
3.3.1 Experiment Setup.....	81
3.3.2 Chatter Loss and the de-bouncers	86
3.3.3 Loss due to switch delay	92
3.3.4 Working Mechanisms of De-bouncers.....	93

3.3.5 Low voltage driven S-SSHI	95
3.4 Discussion	96
3.4.1 Chatter Loss on P-SSHI and S-SSHI	96
3.4.2 Comparisons of the proposed switching methods	97
3.4.3 Designing the hybrid switched SSH system	99
3.4.4 Comparison to the original smart switch considering the phase difference	101
Chapter 4. Magnetically Connected Array	103
5.1 Design concepts.....	103
5.2 Theoretical Assumption and Simulation	104
5.2.1 Interaction between 2 Beams	105
5.2.2 Interaction between 3 Beams	109
5.3 Experiment	120
5.3.1 Experiment Setup.....	120
5.3.2 Experiment results for symmetric alignment of 3 beams	121
5.3.3 Experiment results for asymmetric alignment	122
5.4 Discussion	134
Chapter 5. Conclusion and Future work.....	135
6.1 Hybrid Switches	135
6.2 Magnetically Connected Arrays	136
6.3 Summary (Impact).....	137
6.4 Future Work.....	137
6.4.1 The hybrid switches on miniaturized systems	138
6.4.2 Magnetically connected beam arrays	140

Table of abbreviations	143
REFERENCES	145

LIST OF FIGURES

Figure 1-1 The world fossil fuel production curve forecast [1].....	1
Figure 1-2 The IoT concepts.....	2
Figure 1-3 The energy harvesting market forecast.....	3
Figure 1-4 Energy harvesting devices in different scale in size corresponding to power output [7] [8] [9, 10].....	7
Figure 1-5 Solar harvesters in different scales	8
Figure 1-6 Thermal Energy Harvester	9
Figure 1-7 A radio frequency energy harvester, acquiring energy 6.5 km from the TV tower.....	10
Figure 1-8 General spring mass damper model for transducers	12
Figure 1-9 Magneto-electrical energy harvester	12
Figure 1-10 Three configurations of the electrostatic energy harvesting	13
Figure 1-11 A piezoelectric cantilever based energy harvester.....	14
Figure 1-12 Working modes of the piezoelectric beam	14
Figure 1-13 Equivalent circuit model of a single beam considering only the first resonance	17
Figure 1-14 A typical voltage output respond to chirping frequency.	18
Figure 1-15 Cantilever array to create broad band [25].....	19
Figure 1-16 Model for stopper in forms of cantilever adopted from [28]	19
Figure 1-17 Results comparisons of different stopper distances on both sides.....	20
Figure 1-18 Bistable energy harvesting concepts	22
Figure 1-19 Output result of buckled-spring-mass systems	23
Figure 1-20 Stacked MDOF Modeling	24
Figure 1-21. Mother-Sibling Model of MDOF PEH redrawn from[23].	25
Figure 1-22 2DOF Structure design and results [44]	26
Figure 1-23 Stress simulation of a 2DOF beam [45]	27
Figure 1-24 Spiral MEMS 2DOF device [46].....	28
Figure 1-25 Up conversion design using electromagnetic energy harvesting [31]	29
Figure 1-26 Tuning by preloading on axial direction	30
Figure 1-27. Magnetic resonance tuner.....	30
Figure 1-28 Different SSH circuits, adopted from [21]	33
Figure 1-29 Normalized harvested powers under constant vibration magnitude. [21].....	34
Figure 1-30 SEH circuit and the power feedback	36

Figure 1-31 SSHI topologies with tagged voltage and current flow	37
Figure 1-32. Reduced power feed-back using SSH techniques (P-SSHI).	37
Figure 1-33 Electrical autonomous switches	41
Figure 1-34 Mechanical switch designs	43
Figure 1-35 Circuit connection for cantilever arrays [83]	44
Figure 1-36 Connecting two beams using OSECE [84]	44
Figure 2-1 Schematic diagrams of the piezoelectric MEMS generator. [10]	47
Figure 2-2 Schematic diagram of bimorph poling and connection.....	47
Figure 2-3 Power and voltage outputs of Micro PEH excited with varying acceleration levels.....	49
Figure 2-4 Diode Analysis using Keithley 2420 source meter	50
Figure 2-5 Rectify loss experiment of IC DB155	51
Figure 2-6 Diagrams showing different states of a SSH switching	55
Figure 2-7 Inversion investigations.....	56
Figure 2-8 The voltage distribution on the smart switch	57
Figure 2-9 Circuit modeling of charging state during SSHI switch	59
Figure 2-10 Bode plot simulation of the model on Matlab.....	60
Figure 2-11 Experimental results of power outputs with voltage inputs less than requirements	61
Figure 2-12 Power output results of transient voltage driven cases using $d_{31}\#2$, from Table 5	62
Figure 2-13 Experimental results of parallel SSHI with power sources enough to drive SSHI.	65
Figure 2-14 Comparison between the harvested power of self-powered SSHI and SHE.....	67
Figure 3-1 The glass sealed reed switch.....	70
Figure 3-2 Reed chattering experiment.....	71
Figure 3-3 Applying reed switch on LF-P-SSHI.....	72
Figure 3-4 Conventional snubbers used in microprocessor controls.....	73
Figure 3-5 Unidirectional reed switch de-bounced on resistor (RDR)...	75
Figure 3-6 Unidirectional reed de-bounced on inductor (RDI)	75
Figure 3-7 Schematic diagram of SCR.....	76
Figure 3-8 Unidirectional SCR de-bouncer	77
Figure 3-9 The cause of switching time difference.....	79
Figure 3-10 Flow chart of experiment concept.....	81
Figure 3-11 Experimental setup	83
Figure 3-12 Reed switch applied on LF-P-SSHI without de-bouncing..	86
Figure 3-13 Energy loss due to switch chattering driven on 0.07 g, beam 1.....	87

Figure 3-14 Current flow of filter snubbed LF-P-SSHI on switching....	88
Figure 3-15 Power output experiments for filtered de-bouncers	89
Figure 3-16 Piezo voltage output when high impedance is loaded at the RDI S-SSHI	90
Figure 3-17 Current flow of SCR snubbed LF-P-SSHI on switching, 0.03g beam 1	90
Figure 3-18 Output of SCR de-bounced comparing to other circuits.....	91
Figure 3-19 SCR malfunctioning waveform with overdriven voltage. ..	91
Figure 3-20 Phase difference relations to P-SSHI and S-SSHI gains.....	93
Figure 3-21 Voltage and current tracking of LF-P-SSHI using RDI	94
Figure 3-22 Voltage and current tracking of LF-P-SSHI using SCR.....	95
Figure 3-23 A low voltage driven experiment using RDI.....	96
Figure 4-1 Design concept of the magnetically connected beams.....	104
Figure 4-2 Magnetic interaction between two beams	106
Figure 4-3 Implementation of the MCK model for simulation.....	107
Figure 4-4 Simulation of the magnetic spring coefficient between beam 1 and 2, k_{12}	108
Figure 4-5 Simulation results of the 2 beam interaction	109
Figure 4-6 Interactions between three beams.....	110
Figure 4-7 PSIM Simulation diagram for 3 beams	111
Figure 4-8 Simulation results for the symmetric 3-Beam alignment.....	112
Figure 4-9 Simulation result of the Dirac response	114
Figure 4-10 Simulation results for asymmetrically aligned 3 beam array	116
Figure 4-11 A new configuration for 3-beam alignments	117
Figure 4-12 Simulation results for the modified beam 1	118
Figure 4-13 Bird view of frequency – distance –voltage for one fixed distance	119
Figure 4-14 Cross section of $D_{12}=D_{13}=0.035$ m;.....	120
Figure 4-15 Experiment setup for magnetic connected beam array	121
Figure 4-16 . Experimental results symmetric 3 beam alignment	121
Figure 4-17 Experiment results of identical distances between beams. $D_{12}=D_{13}=10$ mm.....	126
Figure 4-18 Experiment results of identical distances between beams. $D_{12}=D_{13}=15$ mm.....	128
Figure 4-19 Experiment results of identical distances between beams. $D_{12}=11$ mm, $D_{13}=17$ mm.....	129
Figure 4-20 Experiment results of identical distances between beams. $D_{12}=11$ mm, $D_{13}=17$ mm. Voltage output is correspondent to the scanning frequency. (a) Beam 1 loaded with 6g, on tip, connected using magnetic forces and operated separately. (b) Beam 2 loaded with 21.3g, 25mm	

from tip, connected using magnetic forces and operated separately. (c) Beam 3 loaded with 14.3 g, 25mm from tip, connected using magnetic forces and operated separately. (d) Sum of the voltage output of Beam 1-3, connected together or operated separately. Driven on 0.04g..... 131

Figure 4-21 Experiment results of identical distances between beams. $D_{12}=13\text{mm}$, $D_{13}=9\text{mm}$ 132

Figure 4-22 Experiment results of identical distances between beams. $D_{12}=131\text{mm}$, $D_{13}=9\text{mm}$ 134

Figure 5-1 Experiment setup of the Micro PEH with reed switch SSH 138

Figure 5-2 Experiment results of SCR P-SSHI using micro piezoelectric energy harvester 139

Figure 5-3 Circuit simulation for summing up the harvested power 141

LIST OF TABLES

Table 1 Recreated from [5, 6]	4
Table 2 Energy storage density comparison of kinetic energy harvesting [6]	4
Table 3. Approximate scale definition of the energy harvesting systems ..	7
Table 4 Corresponding parameters between the mechanical and electrical modeling for MCK based PEHs	16
Table 5. Lump parameters derived through a network analyzer for the d_{31} and bimorph devices used in this section	48
Table 6. Experimental results with voltage inputs less than requirements in comparison to estimated cases, $V_{oc} = 2.75$ peak	61
Table 7. Beam Parameters	83
Table 8. Component list used in the reed switch based SSH experiment	84
Table 9. Performance of proposed methods under varying operating circumstances	98
Table 10. Geometric parameters of the applied beams.	104
Table 11. Parameters of the beams applied in experiment and simulation.	105
Table 12. Parameters of Magnets used in the experiment and simulation.	105
Table 13. Beam Parameters for asymmetric 3-beam experiment	122

Chapter 1. Introduction

The energy crisis and the demand of smart objects have attracted the scholar's attention to energy harvesting. Among the methods, piezoelectric materials have a relatively high energy density, comparing to other forms of mechanical energy harvesting materials. However, there are some limitations to break still, which would be furthermore mentioned in the next sessions. In this chapter, motivation, bottleneck and the project aim would be pointed out, followed by the research method, the result contribution, and lastly the dissertation organization

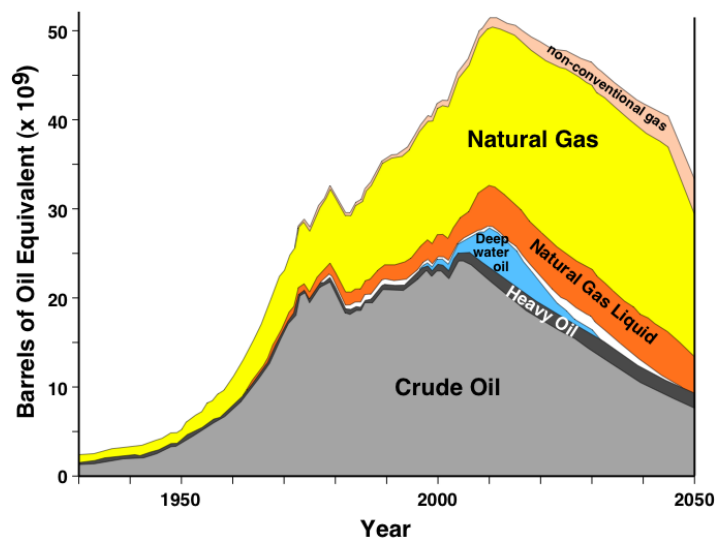


Figure 1-1 The world fossil fuel production curve forecast [1]

1.1 Motivation and Aims

Equation Chapter (Next) Section 1 Internet of Things (IoT), a future concept that is now approaching to reality. In the near future, most objects in daily life come to be “smart”- they are connected to the internet as their brains, with their own sensors to “feel” the world. Looking to the future, Cisco IBSG predicts there will be 25 billion devices connected to the internet on the upcoming 2020 [2] (Figure 1-2(c)). In the near future, infrastructures like bridges, roads can be self-monitoring. At home, not

only the electronics, anything you can name: garage, table, bed curtain... may bear wireless sensors, to make life easier (Figure 1-2). It would bring inconvenience, however, if each of the sensing nodes not connecting to electrical power requires battery replacement. On the other hand, to supply all the additional sensor, the electrical power is a certain requirement. However, the energy crisis is also a happening event. The major source of electrical power – crude oil has reached its peak of discovery and also other fossil fuels that come with it are facing the same crisis (Figure 1-1). Renewable and clean energy sources are developed, and energy harvesting is among which.

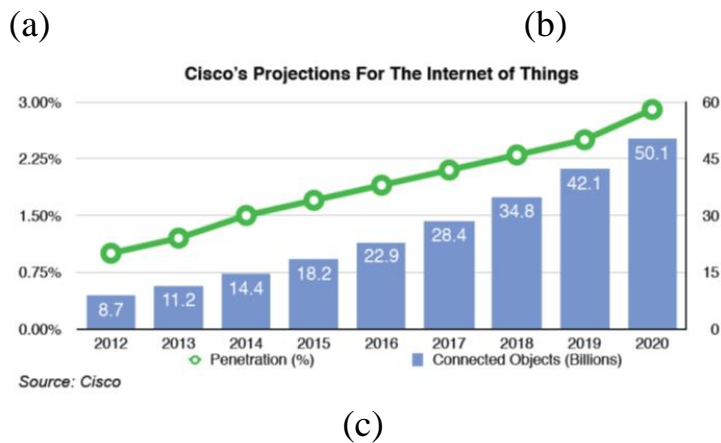
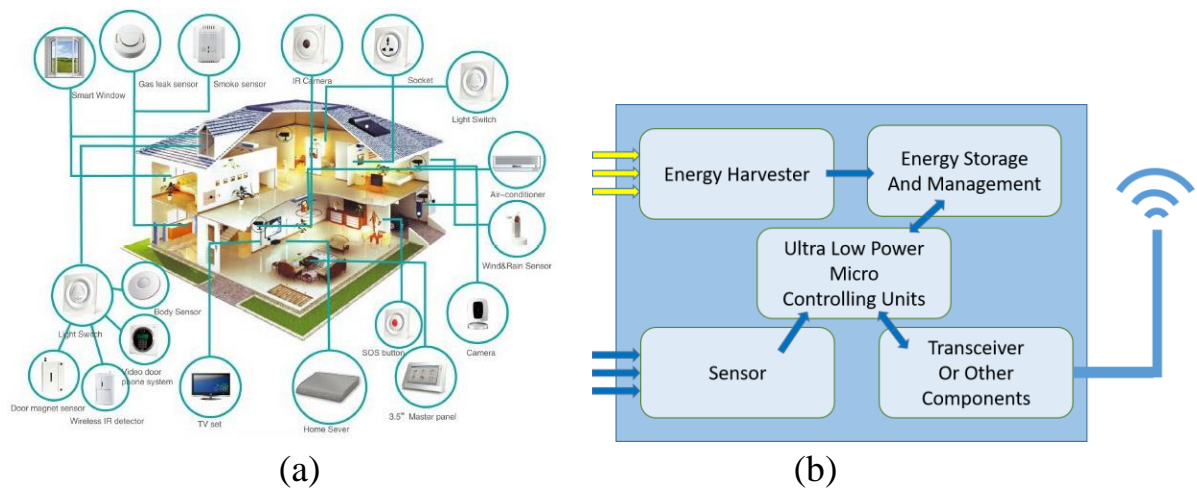


Figure 1-2 The IoT concepts

(a) Smart home concept [3] in IoT (b) Typical wireless sensing node system driven by an energy harvester (c) CISCO's projection to the number of devices connected to the IoT

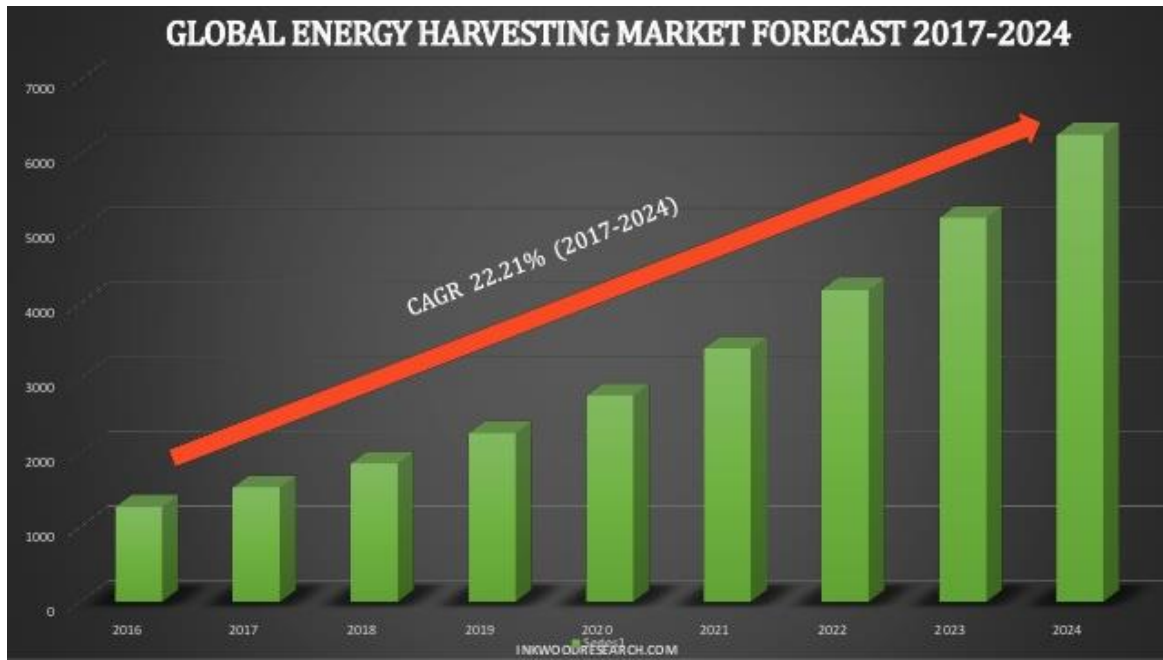


Figure 1-3 The energy harvesting market forecast

The value of 2016 was \$1276 million, and is forecasted to grow to \$6225 million by 2024. Provided by Inkwood Research. [4]

To supply the sensing nodes with clean and renewable energy, energy harvesting systems arose from the researches, and became a popular field of study. As the development of the ultra-low power electronic strives, the power requirement of the wireless sensing nodes has dropped to the scale of milli-watts and microwatts. The lowering of the power requirement creates the possibility to self-power by energy harvesting the ambient environment. The strong need of the market, is predicted to grow from the market value of \$1,276 million to \$6,225 by 2024, as forecasted by Inkwood Research during 2017. (Figure 1-3).

Energy harvesting, is to transform energy from another form to electricity, e.g. from solar power, heat gradient, or other mechanical forms. Mechanical forms such as vibration can be found everywhere in our daily life, any equipment with rotating motors may vibrate when the center is not placed ideally. Infrastructures such as bridges vibrate as vehicles passes by. Natural sources such as wind or human motion,

are also popular field for vibrational energy harvesting. Moreover, vibrational sources provide a feasible power density comparing to other commonly seen source Table 1.

Table 1 Recreated from [5, 6]

Energy Source	Power Density $\mu\text{W}/\text{cm}^2$	Draw Backs	Requires Rectifier?
Solar	15000 Outside	Input range is wide due to light source.	X
	100 Inside		
Vibrational	375	Limited operating frequencies, varying vibrational frequencies	O
Temperature	40	Gradients are usually not large enough	X
RF	Range too Wide	Coupling and Rectification	O

Table 2 Energy storage density comparison of kinetic energy harvesting [6]

Type	Practical Maximum (millijoules/cm ³)	Aggressive Maximum (millijoules/cm ³)
Piezoelectric	35.4	335
Electrostatic	4	44
Electromagnetic	24.8	400

As mentioned in Table 2, piezoelectric energy harvesting has a relatively high energy density compared to electrostatic and electromagnetic means. Thus, we have chosen the piezoelectric energy harvesting method, as it could harvest mechanical energy such as vibration or deformation of its hosting device.

Cantilever beam, as an old topic in vibrational energy harvesting, is easy to fabricate and analyze. It is frequently used as a mother structure of the vibrational energy harvesting device. For example, by attaching a piezoelectric patch on its root,

a simple vibration harvester is born. However, cantilever beams inherit an efficiency issue of operating frequency. As we know, mechanical structures have resonance frequencies, which would transform the input power to the greatest level of deformation. When the operating frequency is near the resonance, the device then works with its optimal efficiency. Therefore, expanding the working bandwidth has been long studied. Using multiple beams with close resonances is a commonly used technique. One of the target in this work, is to expand the working bandwidth using a new form of beam arrays mechanically coupled with repulsive magnetic forces.

To harvest the generated electrical power, an interfacing circuit for energy collection is required. Synchronized switch harvesting (SSH) is a popular solution to increase the harvested power. The main idea is to switch on and off the switches on certain time to alter the current flow, so that the electrical characteristic is changed to a better efficiency. Other than the circuit topology, the switch design is also essential. Electrical smart switches were designed to determine the switching instance, due to the passive component used, certain amount of energy loss is inevitable.

Despite the well-designed functions proposed by previous works for the SSH, the complexity of the circuit also brings new issues due to the vast components, threshold voltage, frequency selectivity and inherited filters which are undesired. These tradeoffs may pay-off when supplant power is generated, such as in bulk sized piezoelectric harvesters (PEH). But when the generated power is limited, to make the best use of the power is then important. In this work, we aim to design a circuit with simplicity, ultimately compatible with Micro-electro-mechanical system (MEMS) devices, which are limited in power generation.

In this research, we aimed on the two previously mentioned issues, by designing two new methods to improve them. A type of mechanical-electrical hybrid switch was designed based on reed switches, to reduce the energy loss of the circuitry. The

operating bandwidth was improved by magnetic connection, which gives the structure a MDOF like output, but with evenly spread stresses. Comparing to electrical connections, this method can achieve a broader bandwidth without considering the parallel or shunt connection effects. A suitable circuit was referenced, where the connection between the beams are separated by inductors, and the interference during connection is reduced.

1.2 The Energy Harvesters

To meet different applications and working conditions, energy harvesters come in different size (Figure 1-4), from macro to nano, there are also vast applications. Table 3 shows some practical applications that goes with different scales of energy harvesting devices (in size, assuming the power/size ratio is positive). The applications that suits within multiple are colored with the same hue. From above mentioned, one can understand that, all of the devices can be included in IoT.

The power-grid can be provided by macro scale harvesters such as wind turbines, solar panels, or piezoelectric alignments under the road. The harvested energy from macro sized devices can be used to provide street lights, and also monitor structural health of the infrastructures. For a scale lower, at the bulk size, wearable devices for consumer's industries or health monitoring like smart watches can be supplied. Then, to the micro scale, system on chips and some biomedical implants lies within the size. As for the nano-scale, some nano-sensors such as for military gas sensing can be applied.

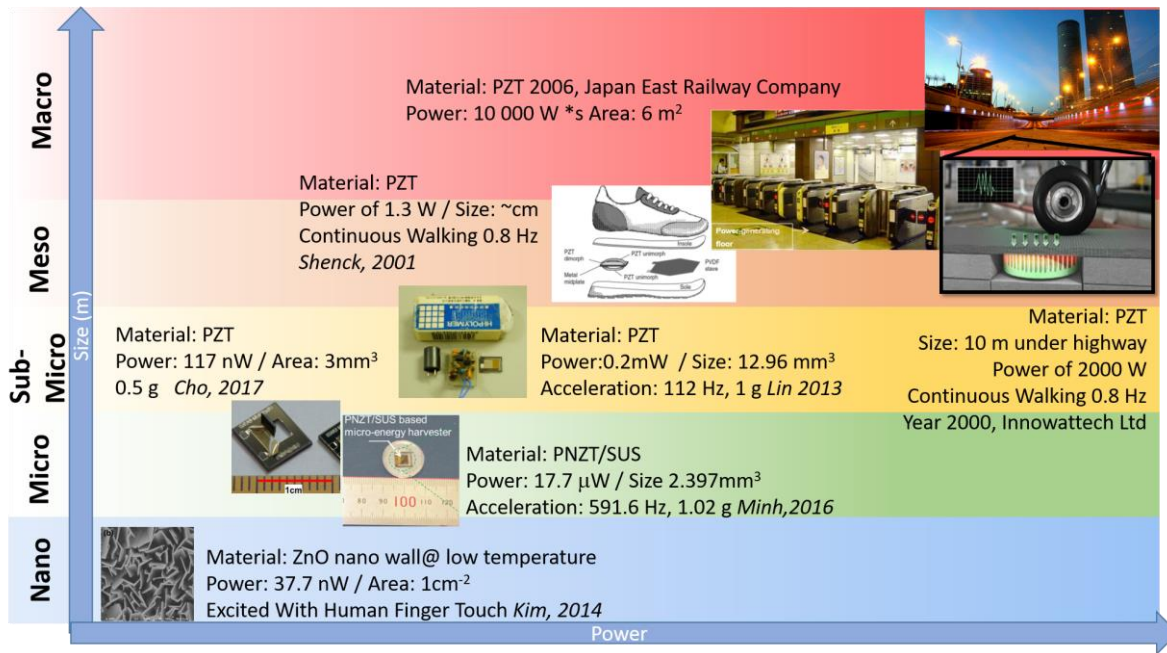


Figure 1-4 Energy harvesting devices in different scale in size corresponding to power output [7] [8] [9, 10]

Table 3. Approximate scale definition of the energy harvesting systems

Size (in meters)	Scale Names	Applications		
$10^0 \sim 10^3$	Macro/Meso	Power-grid	structure monitoring	IoT
$10^{-3} \sim 10^0$	Meso/Bulk	Wearable devices /		
$10^{-6} \sim 10^{-3}$	Micro	Health Monitoring	System on chips	
$\sim 10^{-9}$	Nano	Military: Dust Project	Biomed-Implants	

The methods listed in Table 1 can be further classified in to kinetic energy harvesting and radioactive energy harvesting. Solar, RF, and thermal forces are radioactive energy sources, while vibrational is kinetic. For kinetic forces such as vibrational or rotary, it can be further categorized by its harvesting method, such as electrostatic, electromagnetic, and piezoelectric (Table 2).

For ambient energy harvesting, as listed in Table 1, solar energy seems to be the most promising method. However, the application conditions restrict solar energy harvesting system from general use. That is, some areas on earth do have sunshine all

year long, but some don't. The climate is an unpredictable source. Therefore, other harvesting sources should be also considered. In the following of this section, some energy harvesting techniques from different sources will be introduced.

1.2.1 Radioactive Harvesters

Solar energy has been long studied and applied. It is already in use for large scale energy generation. It comes in a great variety of range: from the size of a wrist watch to grid-connected units (Figure 1-5). In different places, the maximum radiation of the sun varies, from Norway to Congo, from indoor to outdoors. The solar cells are usually made from semi-conductor materials, crystalline silicon (89%), amorphous silicon (10%), cadmium telluride (0.5%), copper indium, diselenide and gallium arsenide.

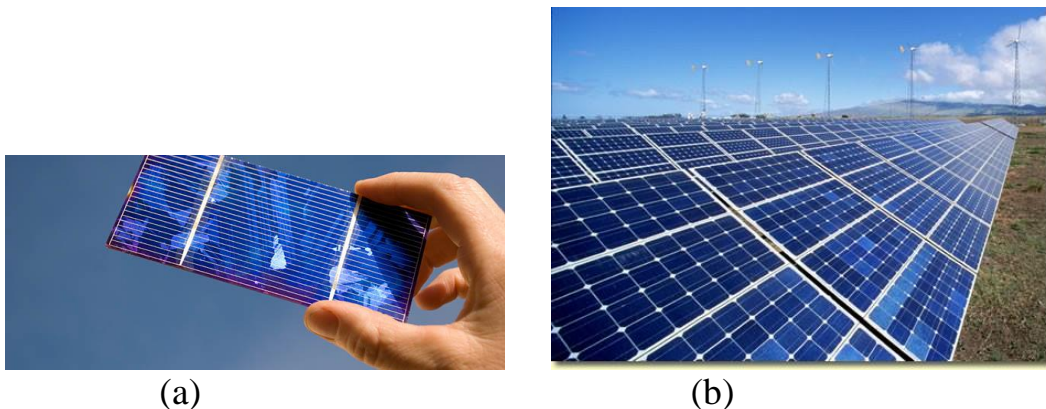


Figure 1-5 Solar harvesters in different scales

(a) A small scale solar harvester [11] (b) Large scale solar cell connected to the grid [12].

As shown in Figure 1-6, thermal energy harvesters utilize the thermoelectric (TE) conversion to convert thermal energy into electric. A harvesting cell basically consists of a thermocouple, semiconductor of a P-type of an N-type. The two semiconductors are connected electrically in series, and thermally in parallel. As there exists temperature gradient between the hot plate and the cold plate, free

carriers flow from the hot plate to the cold, causing a potential difference between the cold plates. The difference of the potential can then create electric energies to be harvested.

Places with constant thermal differences, such as machines that produces waste heat, human skin and the environment are sources for the devices. However, when human body sense the environment change, the skin will reduce the surface temperature to save the inner heat of the body. This lowers the efficiency of the device. Thus, as long as wearable devices are considered, one has to take account of human self-conditioning.

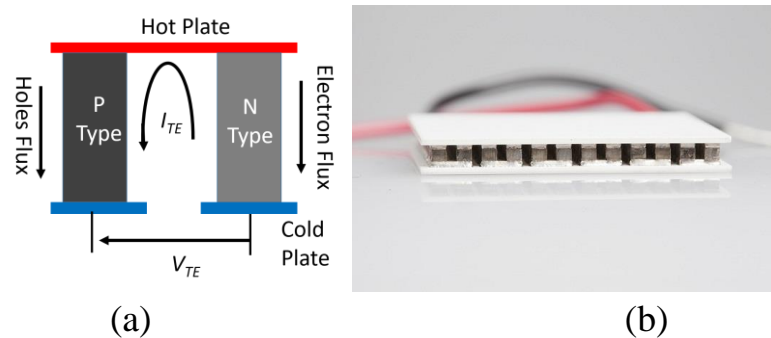
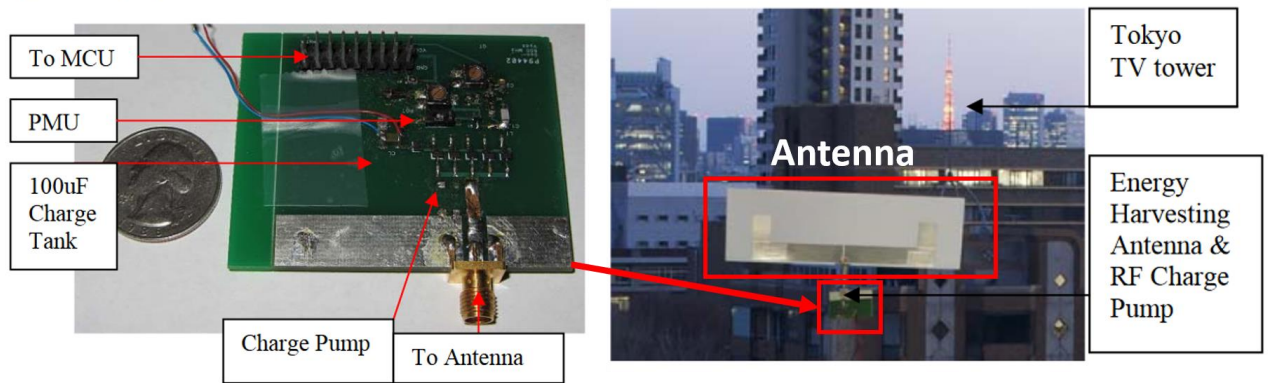


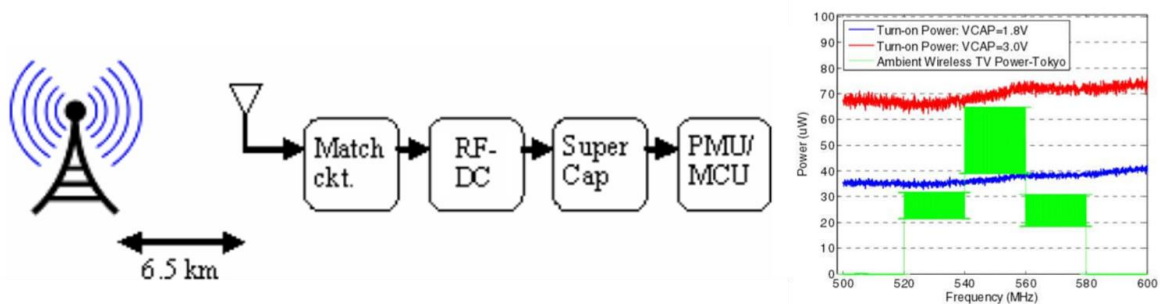
Figure 1-6 Thermal Energy Harvester

(a) Working mechanism of a single cell [13] (b) an actual thermal harvester device[14]

The theory is, as we live in a life full of radio frequencies, TV stations radiates enormous amount of them. TV, WIFI, radio, cell phones... if we could just setup a set of antenna for current induce, the power can be recycled. A well-known radio frequency energy harvesting technique is the wireless charging technique for mobile phones. However, for mobile phones, the radio frequencies are produced by the charger, not the natural ambient frequency. It was previously developed for bio-medical uses. For instance, when an implanted cardiac defibrillator is used, the battery gradually dies out. Another surgery to replace the battery is a waste of resources and also a torture to the patient.



(a)



(b)

Figure 1-7 A radio frequency energy harvester, acquiring energy 6.5 km from the TV tower
 (a) Experiment Setup (b) The schematic of work flow (left) and the experiment results (right) [15]

The examples to charge batteries above are both active, where a radio frequency producing device is used, instead of ambient environments. Figure 1-7 shows an academic experiment, where researchers set the harvester 6.5km away from the Tokyo TV tower [15]. The antenna, mounted on the device, is bulky so that the energy capture is enough. No obstacle is between the TV tower and the harvester, and the result, as shown in the right of Figure 1-7 (b). The blue and red curves indicate the power required to charge the super capacitor. The green, in micro-watts is the harvested power from the location.

From this result, we can conclude that the radio frequency energy harvesting is a “city” option for IoT. First of all, you have to live close to the TV tower, or anything that strongly emits radio frequency. Then, the antennas set on the device is bulky, at

least for now. The efficiency may be greatly reduced indoors. It is however useful, for infrastructure health monitoring in the city, for their antennas can be mounted on the construction itself.

1.2.2 Kinetic Energy Harvesters

Kinetic energy harvesters harvest energy from structural changes such as movements, displacements or deformations. Vibration and rotary energy harvesting are commonly seen examples. They can be easily found on human body and also in the environment. Bridges, buildings are examples that vibrate. It is the most intuitive- for instance, conventional power plants use steam from heat created from fuel to drive the rotors. Then, by Faraday laws, current is induced to be stored. Clean energy harvesting like wind and wave energy harvesting, takes the advantage of air/fluid flows to cause the deformation or rotation of harvesting devices. The two mentioned types can be also in grid-scale.

Other than the magneto-electrical method of Faraday laws, electrostatic and piezoelectric materials are also popular in smaller scale energy harvesting. Vibrational harvesters, as one of the most commonly used structures, usually consist of a host structure, such as a spring or a cantilever beam, that can also be modeled into a mass-spring-damper model (Figure 1-8). It is however restricted to its resonance frequency. There are several bottlenecks: First, on bulk devices, resonance frequencies can be a few tens to a few Hz. However, the miniaturizing of the device brings the resonance frequency to several hundred or kilo-hertz. The ambient frequencies of our natural world is below 120 Hz. That is, 120 Hz is one of the commonly seen target frequencies for energy harvesters, due to the 60 Hz city power doubled by the rectifier. Secondly, the resonance frequency of the structure, which provides the optimal efficiency, is also restricted. Thus, only a small band of specific

frequencies are feasible for optimal power output. To overcome the small operating bandwidth, broadband structures would be discussed later on.

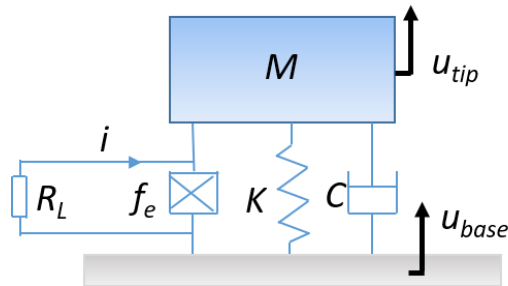


Figure 1-8 General spring mass damper model for transducers

Magneto-electrical method is based on Faraday's law, as mentioned. The concept is to use a moving magnet, where its flux is linked with a coil, or vice versa. During the movement, changing voltage potential is inducted by the varying magnetic flux Φ_m through the coil. Other than vibration, any motion that causes varying flux can induce energy output. It is therefore suitable for wearables since human motion are in low frequency and is not consistent nor periodic, for example the device shown in Figure 1-9(b). With low frequencies and non-consistent movements, the harvested power can be lower than consistent conditions. The proposed wrist band is able to charge a capacitor with 470 μF 25 V up to more than 0.81 V during at most 132 ms from any single excitations.

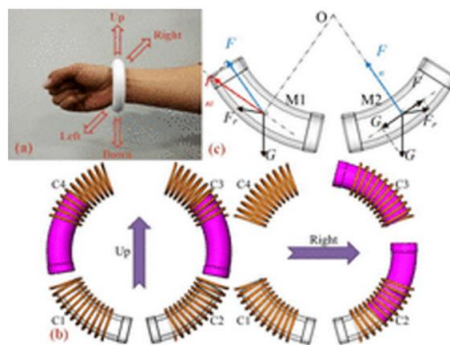


Figure 1-9 Magneto-electrical energy harvester

wearable device with random movements[16] (Non-spring mass system)

For the IoT wireless sensing nodes, the most appealing advantage of electrostatic energy harvesters is that its fabrication process is compatible to the MEMS process. It would indicate that it can be made in MEMS size, and also with batch process-ready for massive production. On vibration, the varying capacitance of moving capacitors changes the electric field. The electric potential change then induces charges, and thus the energy can be harvested. To create the variable capacitance, external voltage bias or pre-charged materials such as electrets are used. As the device vibrates, the relative distance between the two poles changes, inducing the current flow. The vibration can alter the capacitance value by three configurations (Figure 1-10): (a) by changing the gap between the electrodes (b) by changing the overlapping area (c) by changing the overlapping electric field. According to [17], the authors pointed out that, considering the MEMS process, configurations (a) and (b) requires wire leading or bonding on the moving parts, which would lead to the increase of the fragility and thus lowering the feasibility. Therefore, configuration (c), which had both polarities on the same side shows the most promising opportunity with MEMS energy generators. [18, 19]

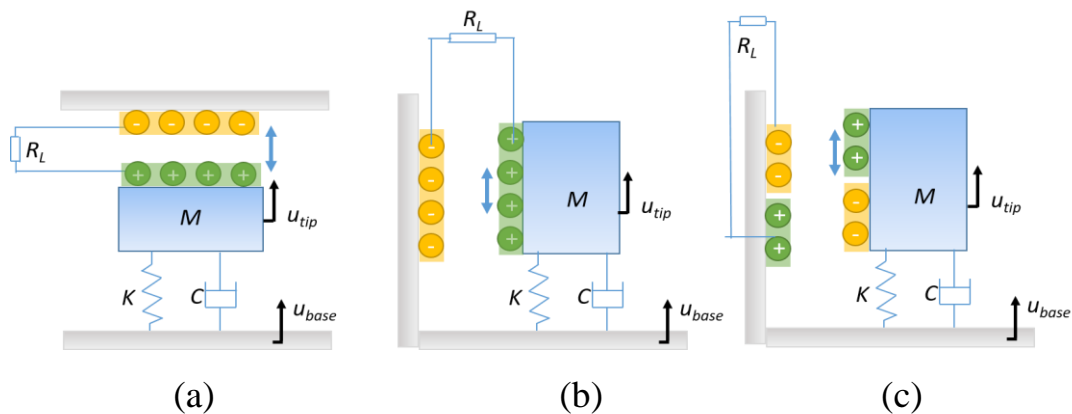


Figure 1-10 Three configurations of the electrostatic energy harvesting
(a) gap changing (b) overlapping area change (c) counter electrode change

The piezoelectric beam is a widely used conventional vibration energy harvester, as shown in Figure 1-11 (a). It consists of a cantilever beam, with a proof mass to adjust and lower the resonance frequency. A piezoelectric material patch is bonded to its root, as it is the location with most strain. Figure 1-11 (a) also shows that when the beam is bending upwards, the beam body has compressive force above its neutral axis. Below the neutral axis, the tensile force is present. Therefore, it is also the deformation direction of the piezoelectric patch. With the understanding of the deformation direction of the patch, the poling of electrodes may define the working mode of the piezoelectric patch, d_{31} , and d_{33} . The subscript 31 and 33 describes the two axis directions of stress and electrical field that occurs during the deformation, as shown in Figure 1-12(a) and (b). The devices in this work uses mode D_{31} , for its full utilization of the electric field, and also the fabrication simplicity.

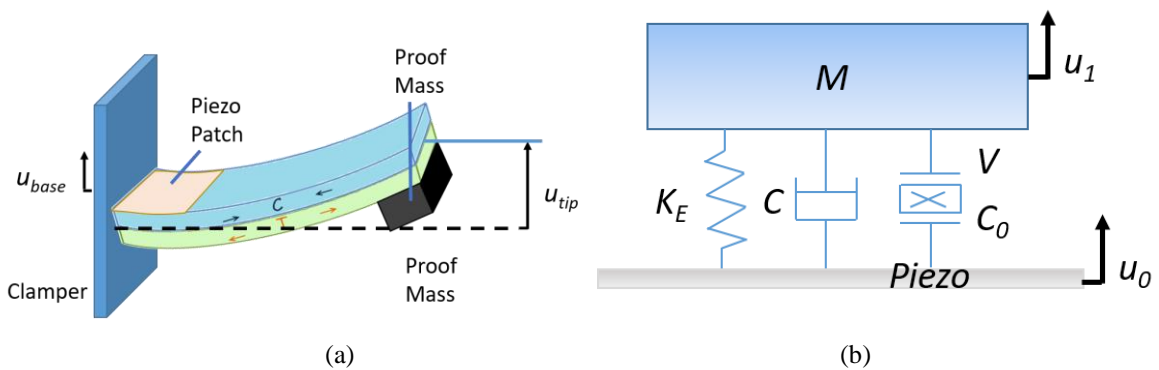


Figure 1-11 A piezoelectric cantilever based energy harvester

(a) Schematic (b) MCK model

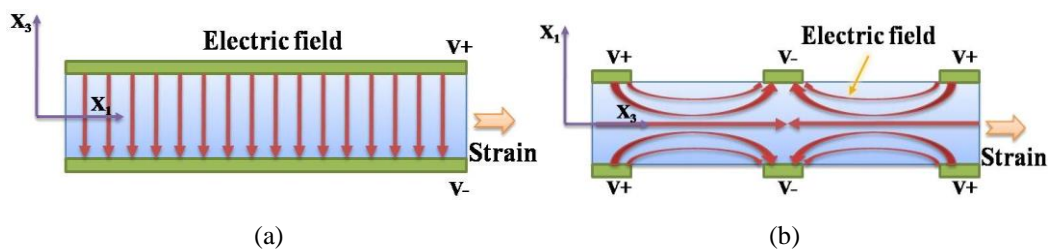


Figure 1-12 Working modes of the piezoelectric beam

- (a) The electric field perpendicular to the strain direction in mode d_{31} (b) The electric field parallel to the strain in mode d_{33} [20]

1.2.3 Modeling of Cantilever-Based Energy Harvester

As a vibrational energy harvesting device, the piezoelectric cantilever beam can be also model into a mass-spring-damper model (MCK) model as shown in Figure 1-11 (b). The model can be then described with eq. (1.2.1) and (1.2.2) [21]. In the equations, $u = u_1 - u_0$, representing the beam displacement, F represents the piezoelectric force due to the elasticity and converse piezoelectric action of the piezo patch, η for the equivalent damping factor, K_E the short circuited stiffness, and M is the equivalent mass. I stands for the output current, V the piezoelectric output voltage of the piezoelectric element, C_0 the clamped capacitance and α the force factor of the piezoelectric patch (electrical-mechanical turns ratio).

Eq. (1.2.3) depicts the energy distribution between different forms. It is an integrated form of (1.2.1) within the period of working frequency τ , from the starting time t_0 . The converted energy will be stored into the piezoelectric element in C_0 and also delivered to the circuit through the circuit, which is expressed as eq. (1.2.4). As for eq. (1.2.4), it describes the energy relation by multiplying the voltage to eq. (1.2.2).

$$M\ddot{u}(t) = F - \alpha V - K_E u - \eta \dot{u} \quad (1.2.1)$$

$$I = \alpha \dot{u} - C_0 \dot{V} \quad (1.2.2)$$

$$\frac{1}{2} M [(\dot{u})^2]_{t_0}^{t_0+\tau} + C \int_{t_0}^{t_0+\tau} (\dot{u})^2 dt + K_E [u^2]_{t_0}^{t_0+\tau} = \int_{t_0}^{t_0+\tau} F \dot{u} dt - \alpha \int_{t_0}^{t_0+\tau} V \dot{u} dt \quad (1.2.3)$$

$$\alpha \int_{t_0}^{t_0+\tau} V \dot{u} dt = \int_{t_0}^{t_0+\tau} V I dt + \frac{1}{2} C_0 [V^2]_{t_0}^{t_0+\tau} \quad (1.2.4)$$

The MCK model can be also expressed as equivalent circuits so that one can apply interface circuitry simulations considering the mechanical characteristics [22]. An equivalent model of a MDOF degree energy harvesting system can be found in Figure 1-21(d). According to [23] and [22], the corresponding parameters between the mechanical and electrical domains is found in Table 4 :

Table 4 Corresponding parameters between the mechanical and electrical modeling for MCK based PEHs

Mechanical Parameters (u_0 = system displacement)	Equivalent Electrical Parameters
Relative displacement $y_n = u_n - u_{n-1}$ y_1, y_2, \dots, y_n	Charge q_1, q_2, \dots, q_n
Relative velocity $\dot{y}_1, \dot{y}_2, \dots, \dot{y}_n$	Current i_1, i_2, \dots, i_n
Mass m_1, m_2, \dots, m_n	Inductors L_1, L_2, \dots, L_n
Damper $C_n, n \geq 1$ C_1, C_2, \dots, C_n	Resistor R_1, R_2, \dots, R_n
Spring Stiffness (Reciprocal) $\frac{1}{K_{E1}}, \frac{1}{K_{E2}}, \dots, \frac{1}{K_{En}}$	Capacitor C_1, C_2, \dots, C_n
Inertia force on mass $m_1 \ddot{u}_0, m_2 \ddot{u}_0, \dots, m_n \ddot{u}_0$	Ideal Voltage Source v_1, v_2, \dots, v_n
Electromechanical turns ratio α	Turns ratio of ideal transformer N

Therefore, a single beam with its first resonance frequency considered can be modeled as a simple MCK circuit as shown in Figure 1-13.

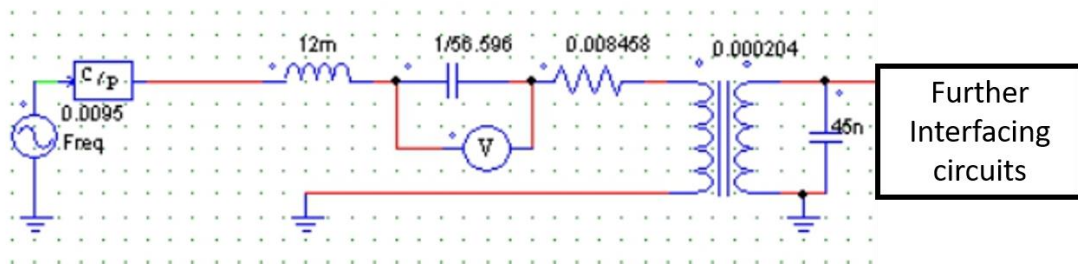


Figure 1-13 Equivalent circuit model of a single beam considering only the first resonance

1.3 Harvesting with a Broader Bandwidth

As mentioned afore, the cantilever structure is hindered by its small working bandwidth near its resonance frequency. Figure 1-14 shows the bandwidth of a piezoelectric cantilever beam output respond to frequency. Q_m , or the quality factor, is a reference to define the bandwidth. The higher the quality factor, the higher power output is presented in the resonance, and so is the curve sharper. It would also refer to a small working bandwidth. Meaning that half a hertz away would bring the output back to a very low level. As a tradeoff, increasing the bandwidth, would also lower the peak energy output of the beam.

To apply in different circumstances and to a wider range of operating frequency, it has been long that researchers strived to broaden the operating bandwidth for PEH devices. Stoppers, beam arrays, up conversion, bi-stable structures, and MDOF structures are some of the popular methods. However, one should be reminded that the decrease of the quality factor also lowers the output voltage, to keep the total amount of energy equal. Thus, a target of the broadband design is to increase, or at least not decrease the overall power output.

Optimal Frequency Scan

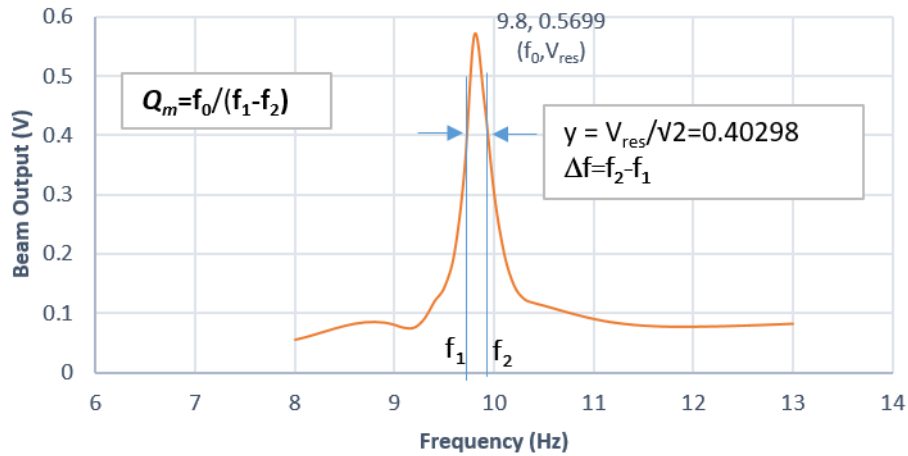
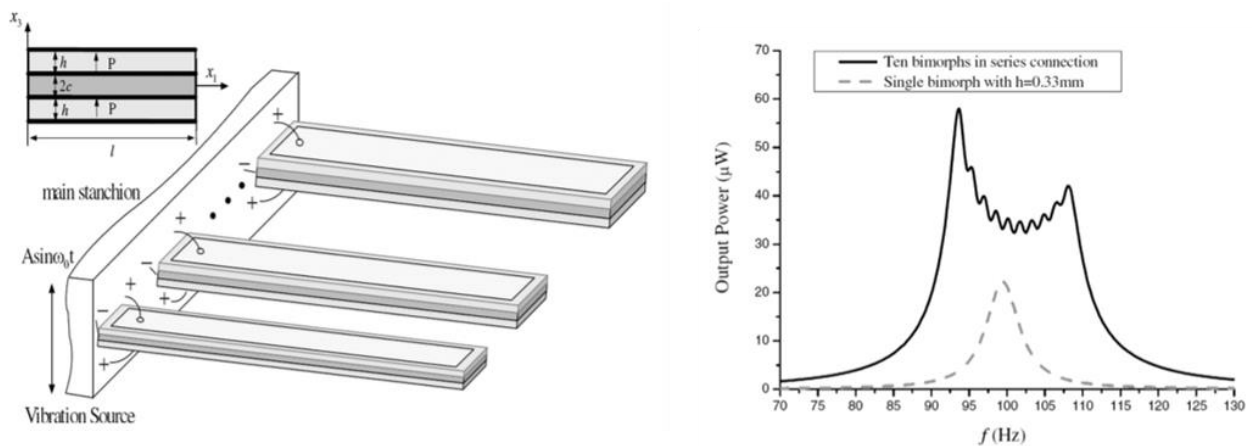


Figure 1-14 A typical voltage output respond to chirping frequency.

Nonlinear mechanical behaviors are studied to improve the working bandwidth of the oscillating harvesters. Tunable, MDOF, stoppers and bistable techniques are the few popular methods due to the ease of implementation and good performances.

1.3.1 Beam arrays

An intuitive method to create broader bandwidth is to combine multiple beams, each having a different resonant frequency. [24, 25] It is however an issue designing the circuit to handle the energy harvested provided by various beams.



(a) (b)

Figure 1-15 Cantilever array to create broad band [25]

(a) schematic diagram (b) numerical results showing ten beams in series connection

1.3.2 Stoppers

Stoppers also enhance bandwidths [26] in forms of rigid or beams. For instance the mechanical switch which also acted as stoppers in [41] was not rigid, and [27] has a rigid case. In [41], two beams with higher frequencies are used, which can be modeled by the MCK model as shown in Figure 1-16. On the point of contact, the two MCK systems merge, and the k and c values sum up as if it is a step increase.

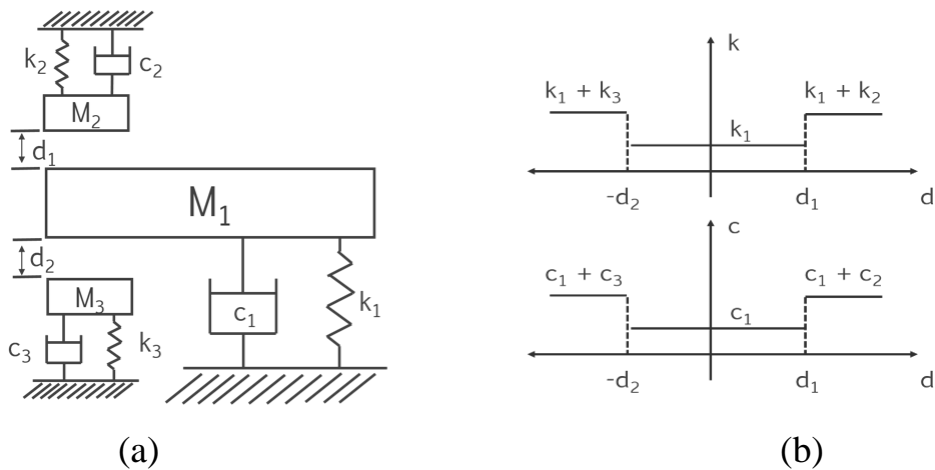


Figure 1-16 Model for stopper in forms of cantilever adopted from [28]

(Redrawn) (a) MCK model (b) the stiffness k and damping c responding to the distance between the masses d_n

The research done in [28, 29] showed a promising results using stoppers with cantilever beams. With a stopper on one or both sides, as shown in Figure 1-17 (a), the tip displacement of the beam is limited to the distance of the stoppers. Figure 1-17 (b) shows the result when stopper is applied to cantilever beam when the frequency is scanned upwards. As it is mention in the work, additional stiffness

occurs to the system when the beam is exerted to the stoppers. [30] uses a cantilever beam with higher resonance frequency as the top stopper, and rigid case as the lower stopper. The beam with higher resonance frequency is also equipped with piezoelectric elements, so that the up converted energy can also be harvested. By the term up conversion, means that the structure uses a low or non-resonant device to strike a structure with high resonance frequency, and therefore creates energy output with higher frequency with low frequency driven systems, as shown in Figure 1-17 (c).

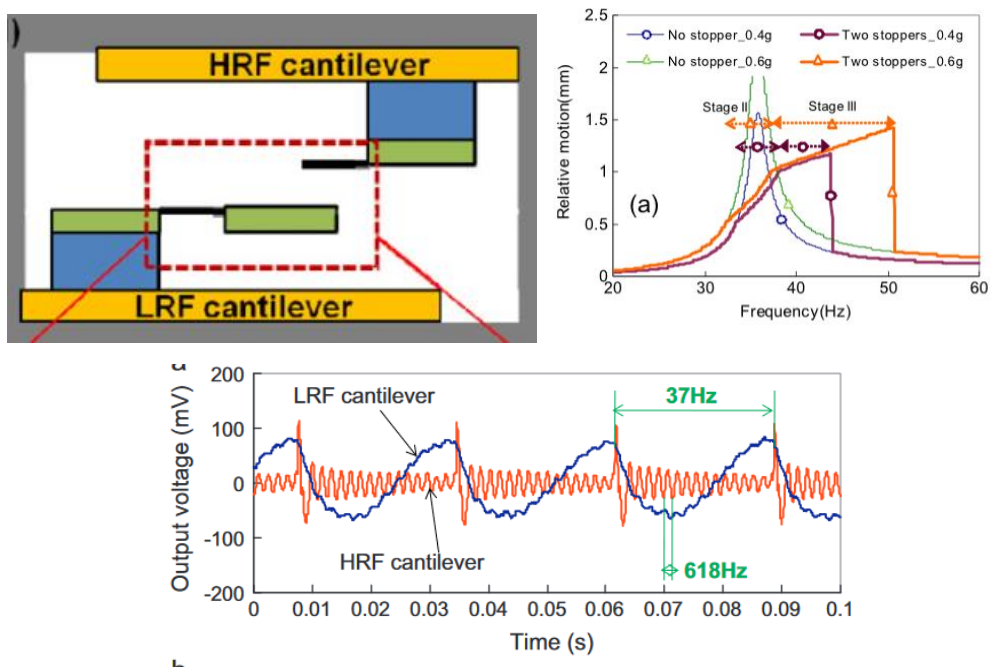


Figure 1-17 Results comparisons of different stopper distances on both sides

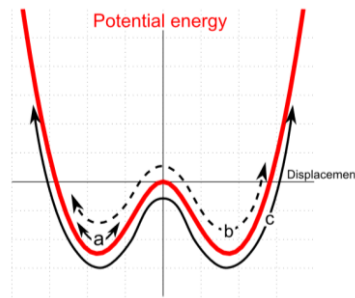
(a) stopper on both side structure, with one side rigid and the other as an up conversion beam [30]

(b) [28] (c) up converted result of [30]

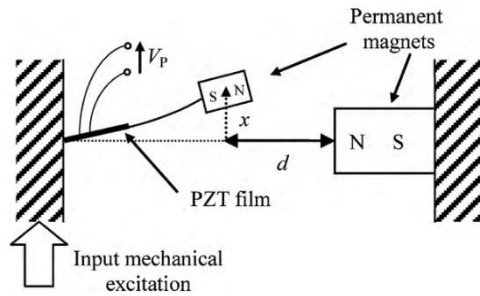
1.3.3 Bistable Structures

Bistable can be implemented by tip magnets [31] [32], bucked structures [33, 34], and other magnetically designed structures[35]. It provides two energy wells, where

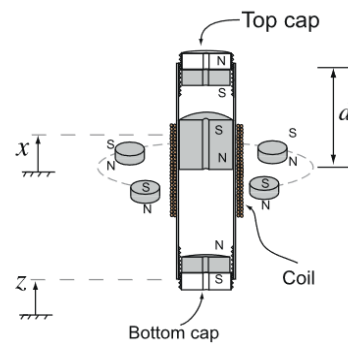
the beams are stable and is linear like within the trap of the well. According to [36], it provides three different working states depending on the input amplitude. In the first state, where the amplitude input is low, the beam would oscillate within one of the energy well. As the amplitude of the oscillation is increased, the second state is reached. The beam oscillates in a chaotic track, between the two energy wells. When the amplitude is increased, overcoming the wells, a periodic characteristic occurs again. Figure 1-18 shows some schematics of the magnetic driven bi-stable setups.



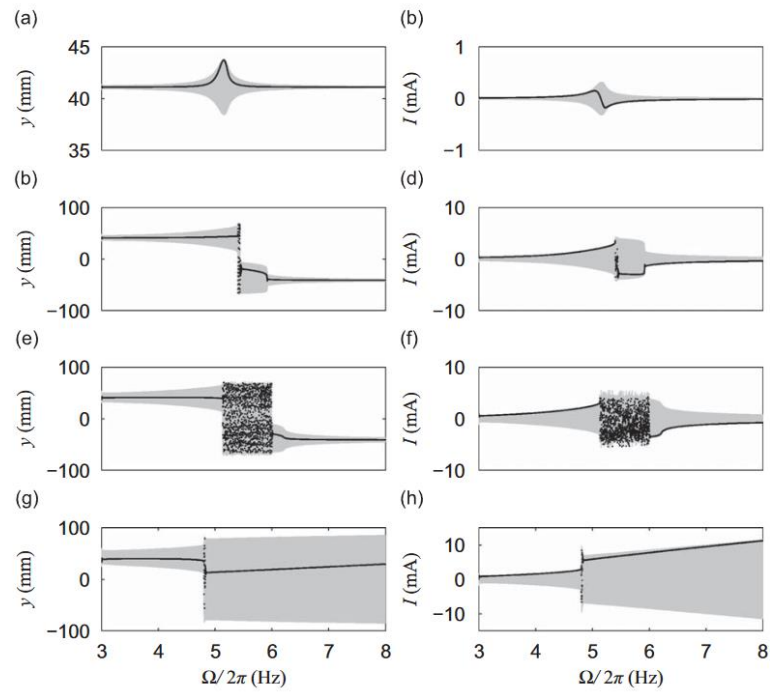
(a)



(b)



(c)



(d)

Figure 1-18 Bistable energy harvesting concepts

(a) Energy well [36] (b) Tip magnet [31] configuration (c) Other magnetic setup [35] (d) Results of under increasing accelerations from 0.1 m/s^2 to 10 m/s^2 , a-h [35]

As another form of realizing bi-stable structure, Figure 1-34 (a) and [34] are non-linear device called Buckled-Spring-Mass system, adopted with stoppers, targeting at the combination of both advantages from the two nonlinear characteristics. The resulting outputs are shown in the following Figure 1-19:

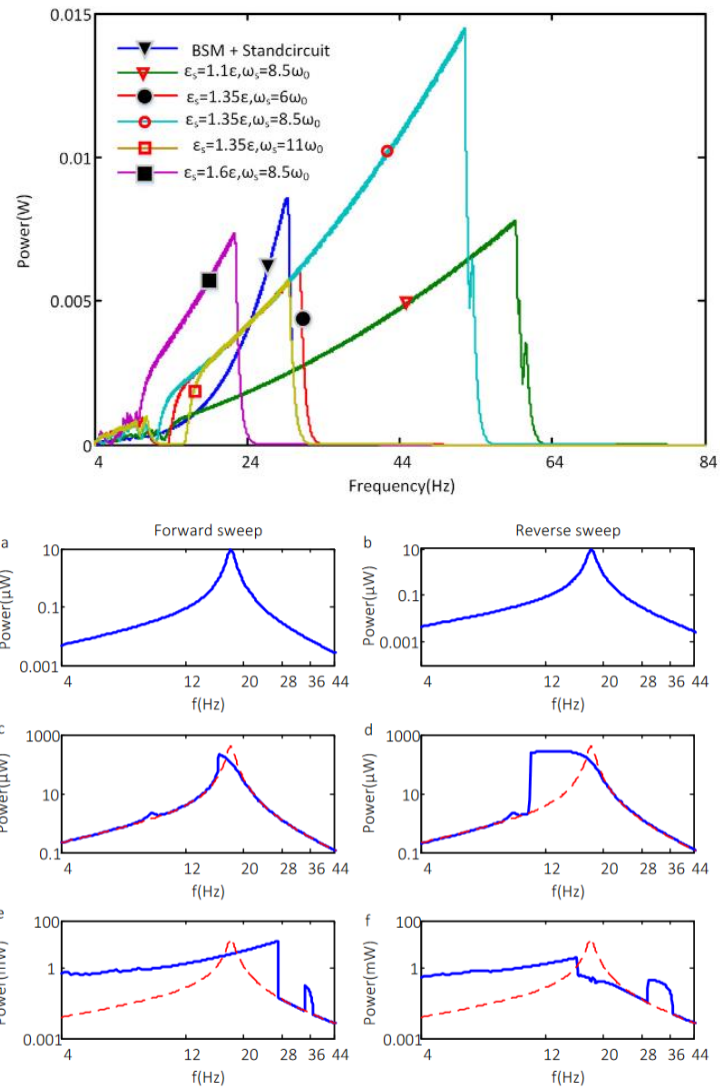


Figure 1-19 Output result of buckled-spring-mass systems

(a) with a stopper [33] (b) With out stoppers. Theoretical voltage output corresponding chirping frequencies under different acceleration levels with forward and backward sweep: a. b. 0.075m/s^2 ; c. d. 0.5m/s^2 ; e. f. 3m/s^2 [34]

1.3.4. MDOF structures

Multi-degree of freedom is another method to improve bandwidth[37, 38]. [23], in 2012 proposed a model with a mother structure for the first degree of freedom, with the 2nd and 3rd degree of freedom installed on the mother structure shown in

Figure 1-21. In 2015, [39] proposed an analytical proof from 1DOF to 5DOF, with the stacking structure where n^{th} structure mounted on the $n-1^{\text{th}}$ body structure (2^{nd} on the 1^{st} , 3^{rd} on the second), shown in Figure 1-20 . In this work, a 2 DOF experiment is performed to prove the theoretical assumptions. Analytical results showed that the increase of the degree of freedom will also increase the power density of the device. [40-43] showed 2DOF structures and results.

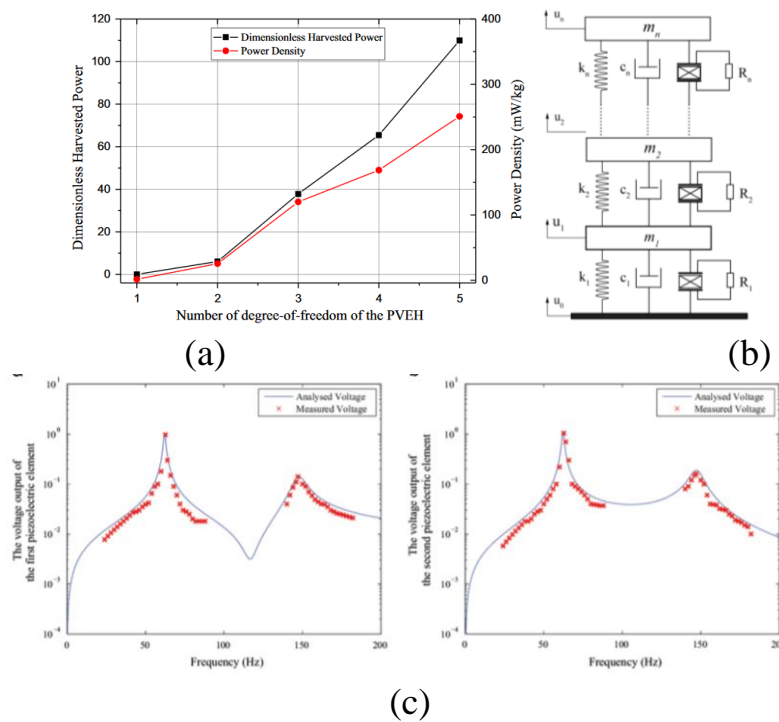
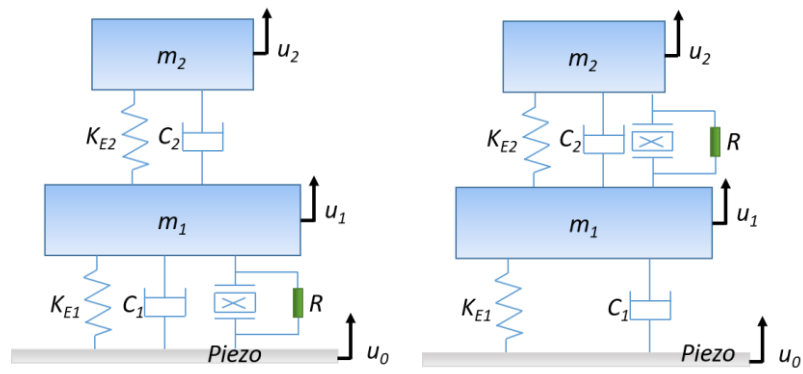
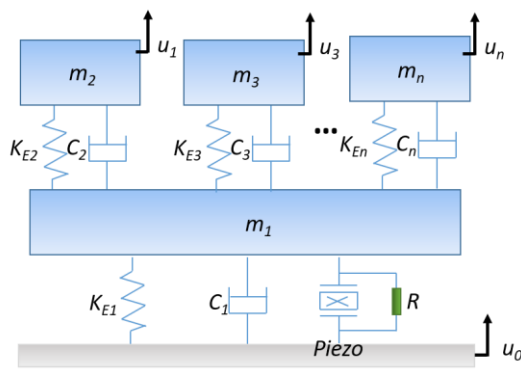


Figure 1-20 Stacked MDOF Modeling

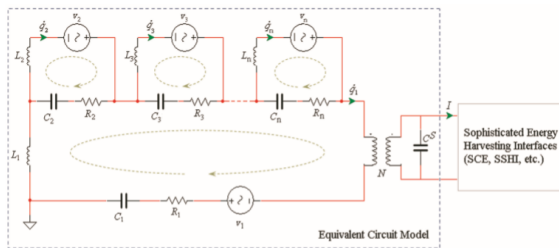
(a) The dimensionless harvested power and the harvested power density versus the number of DOF of the PVEH (b) General MDOF model used in the work (c) Analytical results comparing to experimental results for 2DOF structures, the left shows the output power for the first beam, and the right shows the output for the second [39]



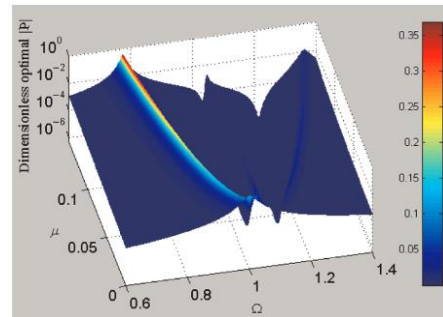
(a) (b)



(c)



(d)



(e)

Figure 1-21. Mother-Sibling Model of MDOF PEH redrawn from [23]

(a) 2DOF degree model, piezoelectric harvester on the 1st structure (b) 2DOF degree model, piezoelectric harvester on the 2nd structure (c) Generalized MDOF for PEH, with piezoelectric element bonded on host structure (d) Equivalent Circuit model of the MDOF degree energy harvesting system (e) Dimensionless optimal power output of 3DOF model from [23]

For 2DOF modeling using the structure [23] has proposed. Eq. (1.3.1)

represents the major beam, or beam 1. Coefficients with subscript numbers identify the beam number. Unidentified coefficients y is the displacement difference of the two masses, $y = u_2 - u_1$. C_n , where the integral $n > 0$, is the damping coefficient of the beam. The MDOF equation and be further expanded, and simulated by circuitry representations as shown in Figure 1-21(d) .

$$\begin{cases} m_2 \ddot{y} + C_2 \dot{y} + K_{E2} y = -m_2 \ddot{x} - m_2 \ddot{u}_0 \\ (m_1 + m_2) \ddot{u} + C_1 \dot{u} + K_{E1} u + \alpha V + m_2 \ddot{y} + (m_1 + m_2) \ddot{u}_0 = 0 \\ -\alpha \dot{u} + C_0 \dot{V} + \frac{V}{R} = 0 \end{cases} \quad (1.3.1)$$

$$\begin{cases} m_2 \ddot{y} + C_2 \dot{y} + K_{E2} y + \alpha V = -m_2 \ddot{x} - m_2 \ddot{u}_0 \\ (m_1 + m_2) \ddot{u} + C_1 \dot{u} + K_{E1} u + m_2 \ddot{y} + (m_1 + m_2) \ddot{u}_0 = 0 \\ -\alpha \dot{u} + C_0 \dot{V} + \frac{V}{R_L} = 0 \end{cases} \quad (1.3.2)$$

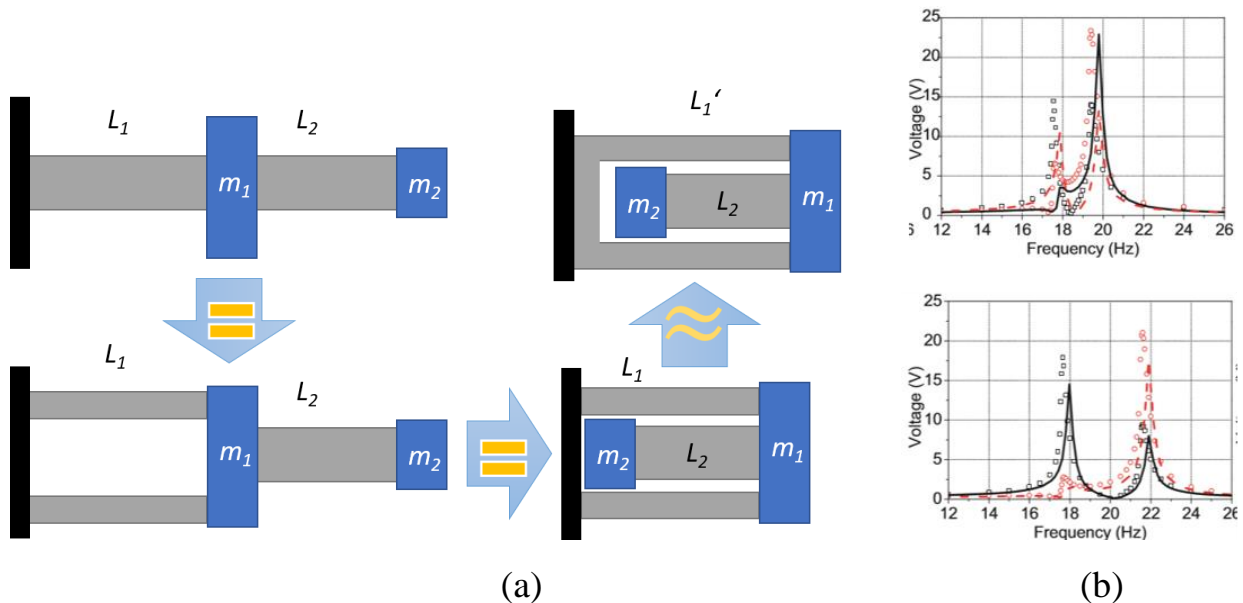


Figure 1-22 2DOF Structure design and results [44]

(a) redrawing of the proposed 2DOF structure, (b) two different experimental results with different proof mass ratios.

2DOF devices are most easily fabricated. One of the realized 2DOF structure was proposed by [43, 44]. As shown in Figure 1-22, a cut-off structure was designed to reduce the overall length of the device. The 2DOF structure is originally as the upper right. It can be transformed to the lower right structure. Then beam of m_2 is folded in, which is still identical to that of the first. It is then designed with a similar aspect ratio, but with a full width for the root.

An stainless steel based MEMS 2DOF design referencing [44] was fabricated [45]. Simulation was also conducted to understand the stress distributed on the resonance. It was worth noticing that the stress is severe on the edges of the root. This shortens the device lifespan, due to the fatigue fracture which would cause on the most stressed locations.

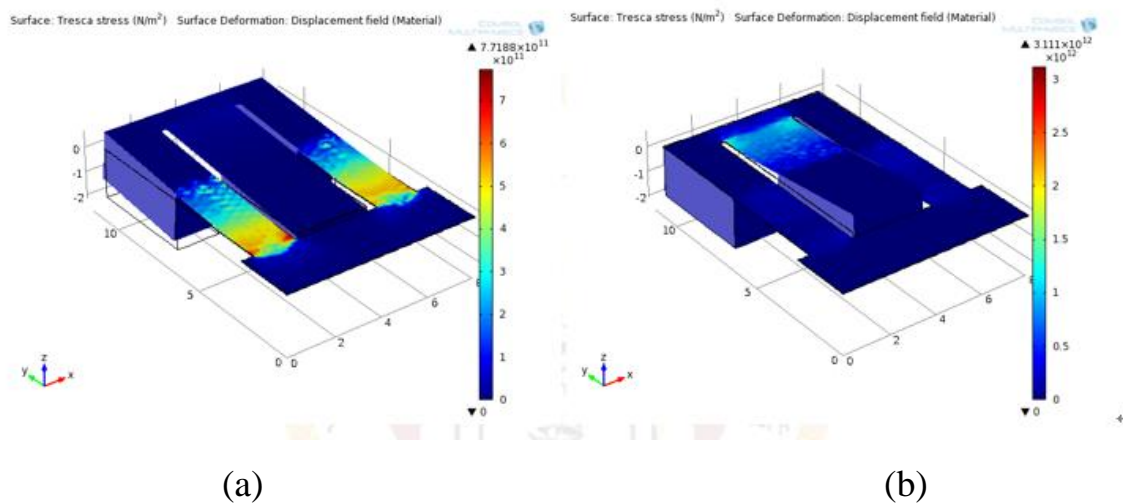


Figure 1-23 Stress simulation of a 2DOF beam [45]
 (a) on first resonance (b) on second resonance

Another structure of 2DOF is fabricated in MEMS, the structure was designed using spiral springs and two masses [46], shown in Figure 1-24. In the results, we can see that the two resonances are far apart, and the working bandwidth was divided into

two bands.

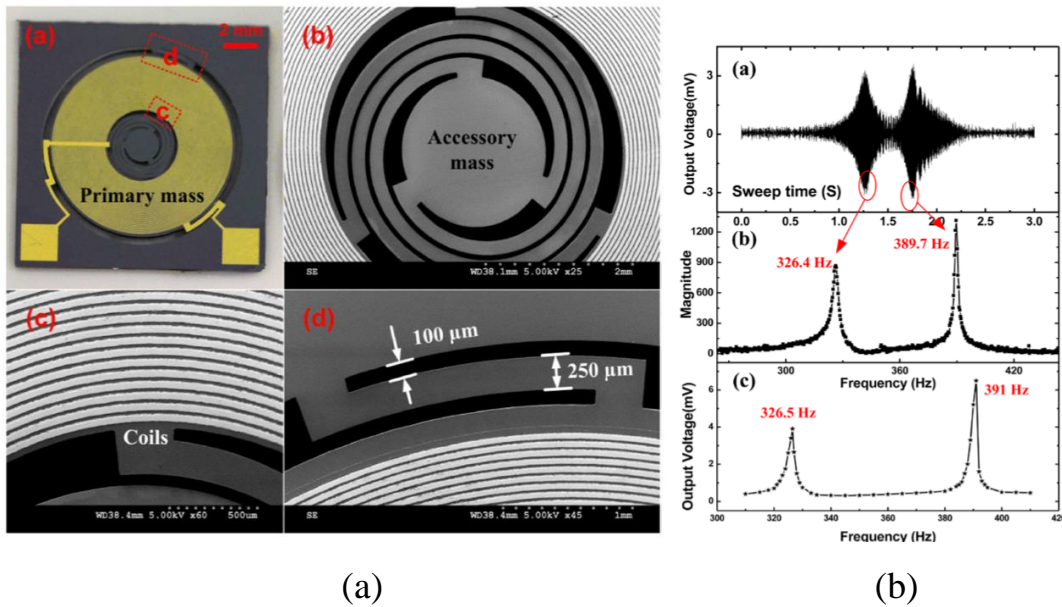


Figure 1-24 Spiral MEMS 2DOF device [46].
 (a) Fabricated device (b) Experimental results

From the researches, one should notice that most 2DOF devices have a host structure, which is used to mount the sub structures. As shown in Figure 1-23, the root of the hosting beam structure endures a high level of stress. From practical consideration, the device should be fragile at the location.

1.3.5 Up Conversion

As the size of the device gets smaller to suit in the small sensors, the operating frequency also gets higher. However, natural vibrating frequencies fall below 120 Hz. To resolve, up conversion was designed to lower the operating frequency. Figure 1-25 (a) shows an typical up-converting design using electromagnetic energy harvesting [47]. In electromagnetic energy harvesting, the magnetic mass induces the current flow. Figure 1-25 (b) shows that the system is driven in the lower frequency

(like the environment), and the mass would trigger a higher output frequency, which is the device resonance.

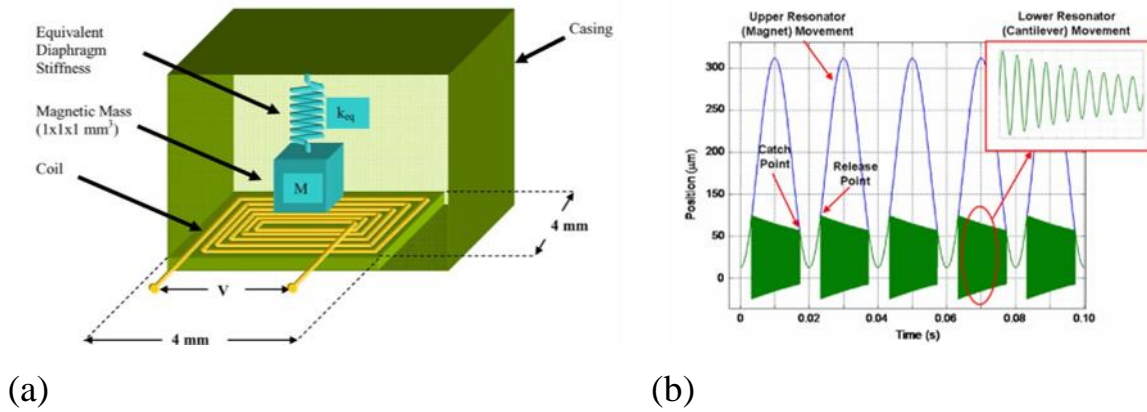


Figure 1-25 Up conversion design using electromagnetic energy harvesting [31]
 (a) Structure design (b) Trigger signal and up-converted signal

[48] shows a piezoelectric up converter by placing ridges on the lower resonant. When the lower resonant moves, the ridges were then brushed over by the probe attached to the higher resonant. Magnetic methods are also applied [49]. The magnets aligned in front of the beam tip create additional tip displacements over the base displacement.

1.3.6 Active Resonance tuning

By using additional piezoelectric actuators, [50, 51] one is able to alter the moment of inertia or the structural stiffness to reach the goal of tuning. Moving the location [52] or changing the mass of the proof mass can also tune the resonance frequency. However, the methods neither requires additional power sources, or human tuning.

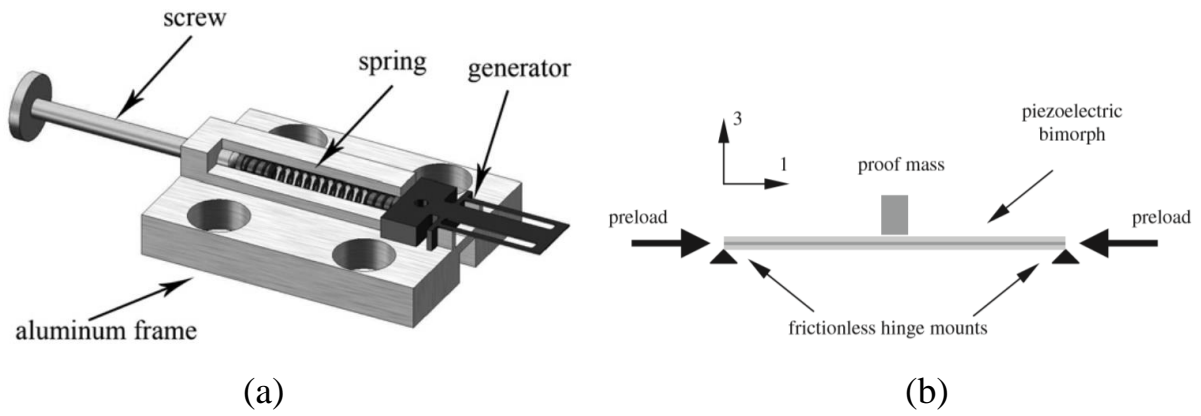
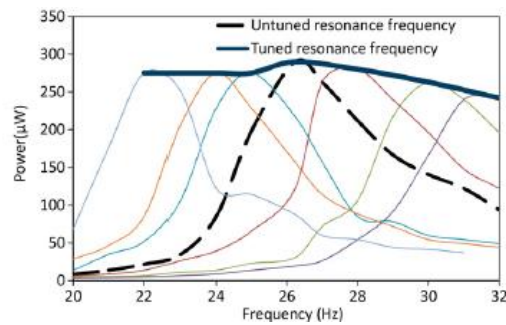
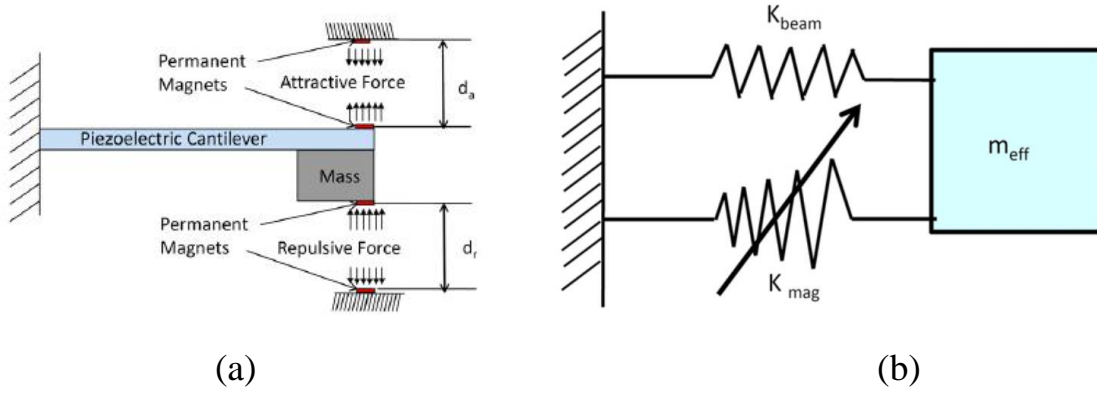


Figure 1-26 Tuning by preloading on axial direction

(a) cantilever [53] (b) fixed beam [54]



(c)

Figure 1-27. Magnetic resonance tuner

(a) Experiment setup (b) Lump Model of the device (c) Experiment Results. [55]

Tuning the stiffness K_E of the structure can also save spaces, it also keeps the

calculation and structure simpler. Giving the structure an axial preload can reach this goal [53, 54, 56, 57]. [56, 57] uses magnets to provide axial forces, while the other two use clamping techniques. An alternative stiffness tuning was realized by using magnetic forces to tune the simple cantilever beam [55] [58] from the vertical direction. To tune the stiffness, or the spring coefficient in the lump model, one or two magnets can be placed below and/or above the beam, with also a magnet on the tip of the beam. The distance of the magnets was tuned, resulting in the change of the repulsive or attractive force applied to the tip of the beam.

The force $F_{mag}(d)$ between cylindrical magnets can be represented as the equation below:

$$F_{mag}(d) = \left[\frac{B_r^2 A_m^2 (l+r)^2}{\pi \mu_0 l^2} \right] \left[\frac{1}{d^2} + \frac{1}{(d+2l)^2} - \frac{2}{(d+l)^2} \right] \quad (1.3.3)$$

To obtain the spring coefficient k_{mag} in Figure 1-27 (b), Hooke's Law is used with eq. (1.3.3). By differentiating the force equation on the magnet distance d , eq. (1.3.4) can be derived.

$$K_{mag}(d) = \left[\frac{B_r^2 A_m^2 (l+r)^2}{\pi \mu_0 l^2} \right] \left[-\frac{2}{d^3} - \frac{2}{(d+2l)^3} + \frac{4}{(d+l)^3} \right] \quad (1.3.4)$$

And therefore, the new system damping coefficient of a single beam K'_E would become:

$$K'_E = K_{mag} + K_E \quad (1.3.5)$$

1.4 The Interfacing Circuits

To obtain the energy transduced, an interfacing circuit is required. The design of the interfacing circuit determines the performance of the energy harvesting system. Most energy generated in mechanical energy harvesting such as vibration comes in alternative current (AC). To retain the energy in storage devices such as batteries or

capacitances, rectification to direct current (DC) is required. The basic method is to use a diode based full bridge rectifier, and a capacitance in parallel to the load. It is named as standard energy harvesting (SEH) in this dissertation.

However, adding an electrical load would increase the damping of the piezoelectric element. Lesieutre et al, [59] had discussed the damp increase in the system due to the electrical load. Moreover, due to the large intrinsic capacitance of the piezoelectric element, the impedance matching circuit is important to reach the optimal generated power. Therefore, different types of circuits were designed to balance the drawbacks. [60, 61] showed that with adaptive control and a circuit consisting of an AC-DC rectifier and a DC-DC step down converter, the increased harvested power percentage is around 325%. However, it is not yet feasible for micro-scale self-powered harvesting system – the power consumption of the controllers to drive and calculate the duty cycle may cost more than what's harvested.

One of the most promising method is the synchronized switch harvesting (SSH). As mentioned previously, energy harvesting was counter usage of damping control. Originated from synchronized switch damping (SSD) [62], a vibration control method, the switching techniques are originally categorized into two types according to the circuit topology. The first type has their switches placed before the rectifier: The synchronized switch harvesting on inductance (SSHI) [63] is introduced in 2005. Considering the relative placement of piezoelectric material, two different types of SSHI by the arrangement of the switch-inductor set are defined: When the inductor-switch set is placed in parallel to the piezoelectric element, it is defined as the parallel SSHI, (P-SSHI). Similarly, in series arrangement, the circuit is named as series SSHI (S-SSHI) [64]. Another configuration to improve is the hybrid SSHI, proposed in 2011 [65]. Active energy harvesting and improved SSHI [66] (2012) aimed to improve efficiency by integrating the switches into the rectifier. The

second group has the switches positioned after the bridge rectifier, such as SECE (Synchronous Electric Charge Extraction, proposed in 2005 [67]) and SSDCI (Synchronized Switching and Discharging to a storage Capacitor through an Inductor)[68](2009).

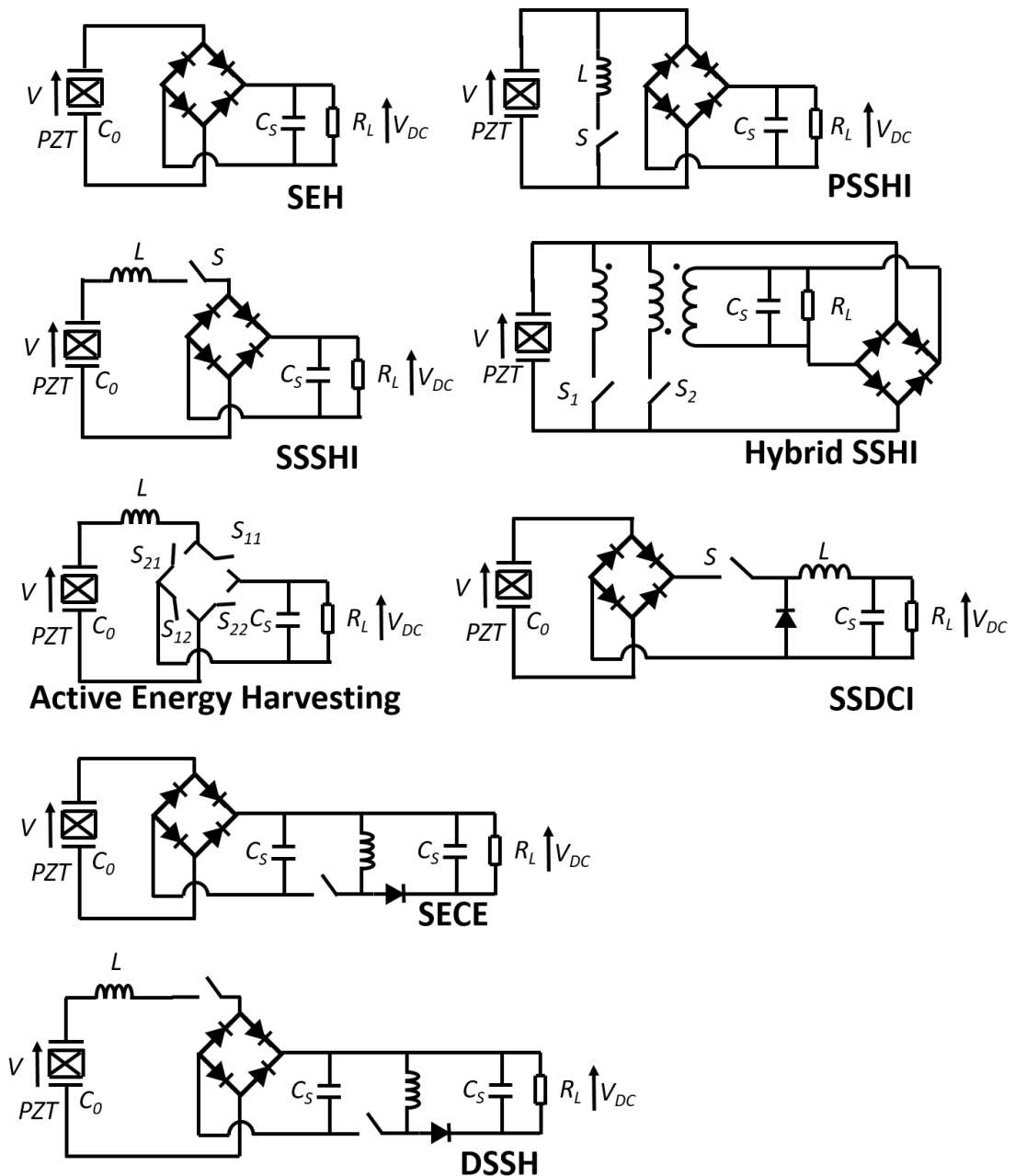


Figure 1-28 Different SSH circuits, adopted from [21]

According to [21], SSHI, SSDCI and active energy harvesting provides direct energy transfer to the load. Which would hinder the energy harvesting due to the back coupling. That indicates, with direct energy transfer, one has to consider the impedance matching for optimal load.

To decouple the impedance, SECE and DSSH (Double Synchronized Switch Harvesting) can be used. DSSH places the switches on both sides of the rectifier [69], while decoupling is realized by using the inductor as a de-coupler. When the decoupling occurs, the optimal power is ideally irrelevant to the loading impedance.

The above mentioned circuit topologies are shown in Figure 1-28. Later, An advanced version of DSSH, ESSH (Enhanced Synchronized Switch Harvesting) was then proposed during 2010 [70]. The normalized harvested power for comparison is shown in Figure 1-29, where we can visualize the load decoupling.

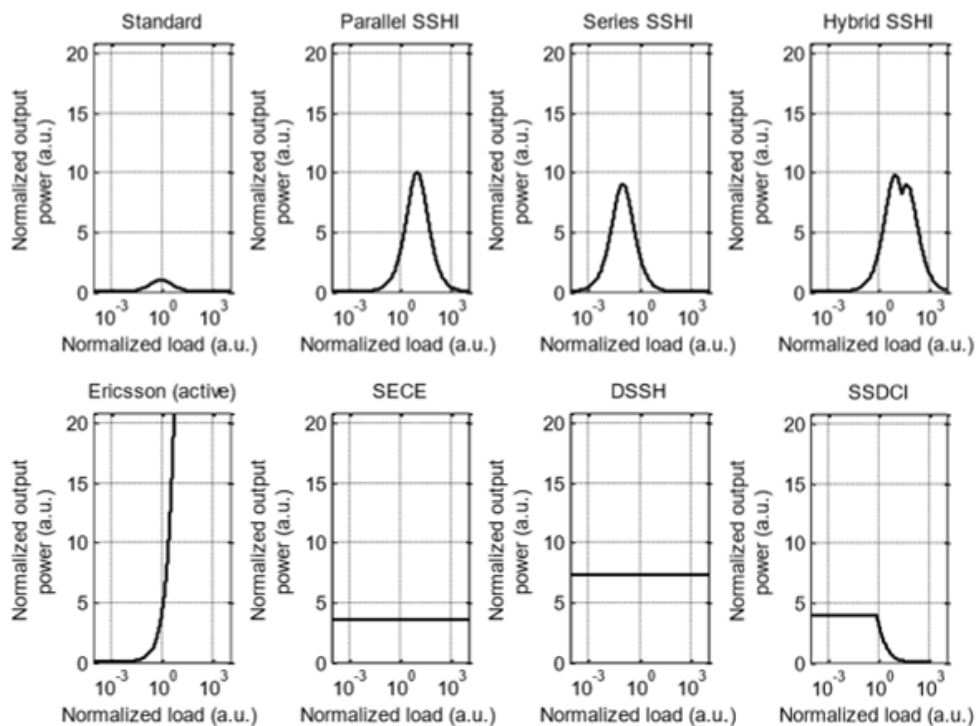


Figure 1-29 Normalized harvested powers under constant vibration magnitude. [21]

Regarding the decoupling effect, SECE and DSSH have successfully decoupled the load with constant power output. SSDCI has good decoupling characteristics with low impedances. Series SSHI has a relatively low optimal load comparing to the other SSHIs. In Figure 1-29, the SSH circuits have their non-ideal circumstances excluded. Therefore, taking account of the switch loss and the damping loss, the actual gain compared to the SEH should be considered lower.

1.4.1 Theoretical Modeling of the Interfacing Circuits

1.4.1.1 Standard Rectifier

As the most basic topology, SEH subjects to energy feed backs. Therefore, SEH is not able to provide the maximum power. Figure 1-30 (a) shows the typical AC waveforms of SEH. One can observe that there is a phase difference between the rectifier loaded output piezoelectric voltage V , and the piezo current I Figure 1-30 (b)). Consequently, the product of V and I , or the output power is feedback to the piezoelectric element due to the negative power harvested (colored zone).

The maximal power output of SEH during constant force can be expressed with the equation as follows [71]:

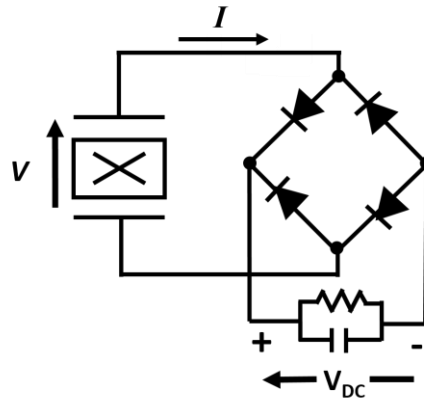
$$P_{F,standard} = \frac{R_L \alpha^2}{(R_L C_0 \omega + \pi / 2)^2} \times \frac{F^2}{C + \frac{2\alpha^2}{(R_L C_0 \omega + \pi / 2)^2}} \quad (1.2.1)$$

$$P_{u,std} = \frac{R_L \alpha^2}{(R_L C_0 \omega + \pi / 2)^2} \times \omega_2 u_M^2 \quad (1.2.2)$$

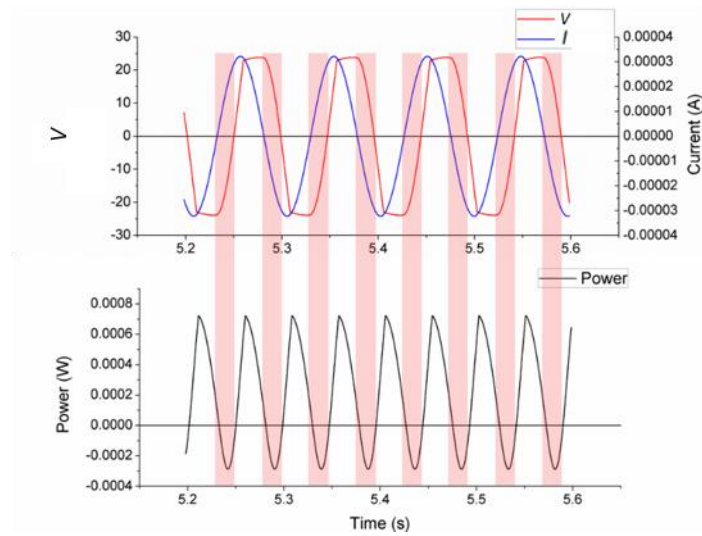
where R_L is the optimal load of SEH.

$$R_L = \frac{\pi}{2\omega C_0} \quad (1.2.3)$$

Equation (6) can be used to express the relationship with respect to the displacement.



(a)



(b)

Figure 1-30 SEH circuit and the power feedback

(a) Standard Energy Harvesting Circuit (SEH), (b) Energy feedback due to the current-voltage phase difference (below). It is the product of the voltage and current. The piezoelectric voltage (V) is represented by the red curve. The blue curve indicates the piezoelectric current (I).

1.4.1.2 Synchronized Switching Methods

To reduce the energy feedback, SSHI launches an LC resonance which utilizes an additional inductor to resonate with the clamped capacitor of the piezoelectric

element. The half-cycled LC resonance launched on the extremes of the tip displacement causes a quick inversion of the voltage. On the maximum voltage of inversion, which is also the current zero point, the switch is turned off so that the voltage would not fall back. Through this method, the voltage and the current are forced to be in-phase to avoid the unwanted power feedback, and the voltage output was leveraged to a higher level.

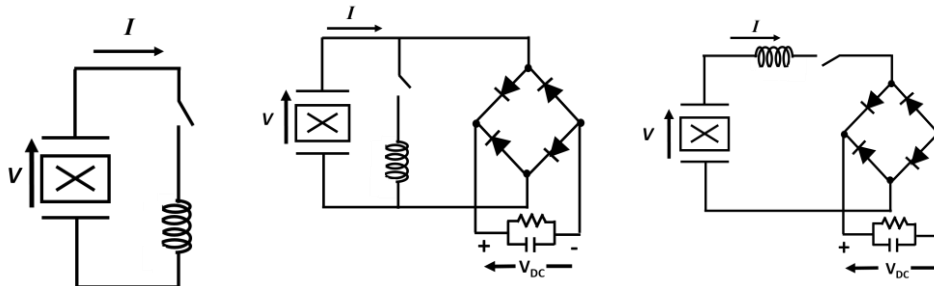


Figure 1-31 SSHI topologies with tagged voltage and current flow

(a) Load Free Parallel SSHI (LF-P-SSHI), (b) Parallel SSHI (P-SSHI), (c) Series SSHI (S-SSHI)

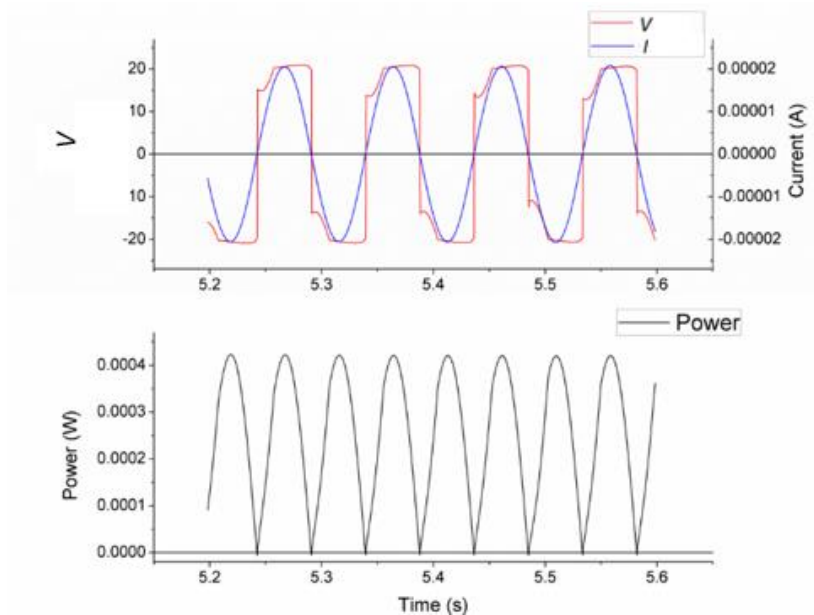


Figure 1-32. Reduced power feed-back using SSH techniques (P-SSHI).

The red curve V denotes the piezoelectric voltage, and the blue curve I denote the current flowing out of the piezoelectric element, the current and voltage to be in-phase.

Figure 1-31 shows the fundamental implements of the SSH techniques with voltage and current labels. This method is used to observe the waveform change without any load or rectifier, which also has the least power loss in consequence of the simple circuit. The current of which can be best observed since it is lightly loaded in impedance. In this work, it is defined as the load free parallel SSHI (LF-P-SSHI), which can be found in Figure 1-31 (a). It is named because of its similarity to parallel SSHI (P-SSHI), shown in Figure 1-31 (b), which is named by the location of the inductance-switch set.

On launching the switch of P-SSHI, the switching instance continues for half of the LC resonance period t_s , which is designed to be much smaller than the source frequency (eq. (1.2.4)). Nevertheless, one has to take account of the inner resistances of the components which lead to the non-perfect inversion. The loss ratio is usually denoted as γ . By this ratio, the inversed voltage can be obtained by the product of voltage before inversion and the coefficient. The ratio is determined with equation (1.2.5), where Q_i is the quality factor of the resonance.

$$t_s = \pi\sqrt{LC_0} \quad (1.2.4)$$

$$\gamma = e^{-\frac{\pi}{2Q_i}} \quad (1.2.5)$$

As for P-SSHI, the switch conducts and the current flow through the inductor to the regulator. The experimental value of γ is obtained with V_{DC} for S-SSHI. V_{DC} denotes the rectified voltage across the load and capacitor of the rectifier.

The optimal power output of P-SSHI, eq. (1.2.6), and S-SSHI, eq. (1.2.7), during constant force can be also found in [71]:

$$P_{F,P-SSHI} = \frac{4R_L\alpha^2}{(R_L C_0(1-\gamma)\omega + \pi)^2} \times \frac{F^2}{C + \frac{4\alpha^2}{(R_L C_0(1-\gamma)\omega + \pi)^2} \frac{RC_0(1-\gamma^2)\omega + 2\pi}{\pi}} \quad (1.2.6)$$

$$P_{F,S-SSH} = \frac{4R_L\alpha^2(1+\gamma)^2}{(2R_L C_0(1+\gamma)\omega + \pi(1-\gamma))^2} \times \frac{F^2}{C + \frac{4\alpha^2(1+\gamma)}{C_0\omega(2R_L C_0(1+\gamma)\omega + \pi(1-\gamma))^2}} \quad (1.2.7)$$

As mentioned in the introduction, we wish to design a structure with simplicity so that the complexity of the circuit can be avoided for limited amount of energy input. Thus, the P-SSH and S-SSH are used in this work.

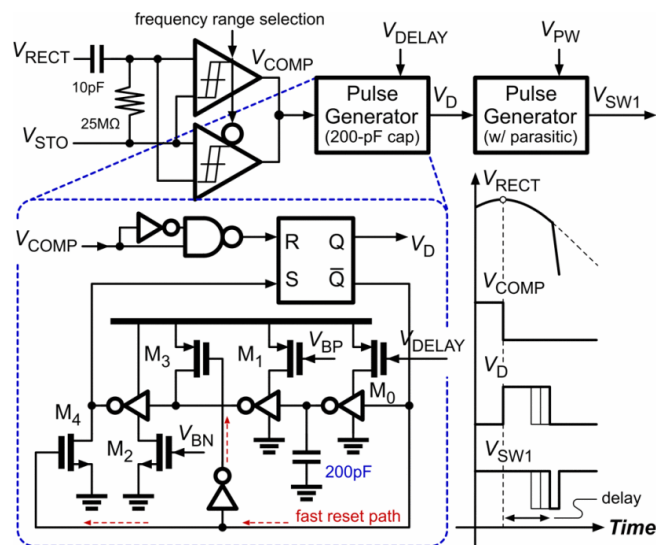
1.4.2 Autonomous Switches for Self-Powered Systems

1.4.2.1 Electrical Switches

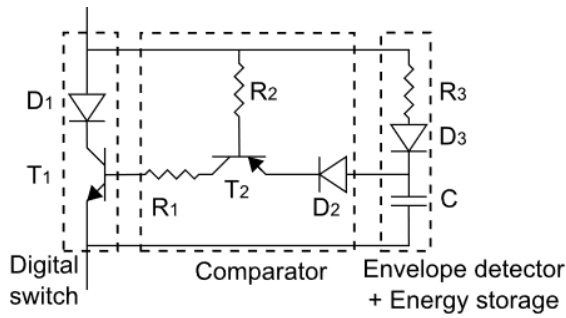
To achieve self-powering systems using synchronized switches, the switches should not be powered by external power. By electrical and mechanical methods, the self-powered autonomous SSH was carried out. With the name self-powered, it means that the energy required to monitor and control the switching instance is supplied by the energy harvester itself. The first electronic smart switch was proposed during 2007 [72]. The smart switch is able to adapt to broader physical excitations [72-74]. In some cases, the switches are also frequency dependent, depending on how the smart switch circuit is designed. Some advanced methods are also proposed to improve, either efficiencies or bandwidths, by precision controls using integrated circuit chip designs[75] (Figure 1-33 (a)) or micro controllers such as peripheral interface controllers [76]. As a precisely designed IC, the control power of the controlling chip in [75] was merely 12 μ W, lowering the optimal conversion efficiency. That also leads to another problem, the switches are power driven, requiring some energy consumptions which may even lower the harvested power when the supplied energy is not enough.

Several self-powered configurations for low power applications were proposed,

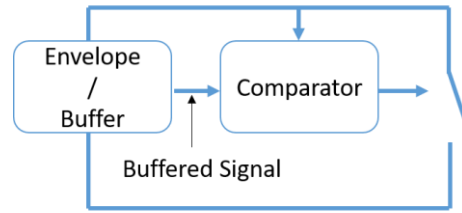
so that the device can be used in wireless applications [72-74]. As shown in Figure 1-33 (b) The proposed setup consists of a signal buffer, composed of a pair of resistance and capacitance. The buffer is used to create a short delay of the signal. Using a transistor, the comparison of the buffered signal and the original signal can be performed. In this way, the approximation of the voltage peak is found with a short delay due to the PN junctions of the transistor. It can be simply modeled into Figure 1-33 (c). To lower the consumption, another design was proposed with reduced components [77]. The methods mentioned above were able to adapt to the single piezoelectric patched cantilever beams. Later, to achieve a precise switching instance, another approach (Figure 1-33 (d)) was proposed [78] by dividing the single patch in to three. Simplified model can be found in Figure 1-33 (e) The divided patches, provided an accurate signal and energy for the current sensor, the operational comparator and the harvesting comparator. However, dividing the patches into three also means that the energy from the other two patches cannot be harvested. It is feasible in bulk sized systems, where there are plenty of space for piezoelectric elements. Nonetheless, in miniaturized systems, that is not practical.



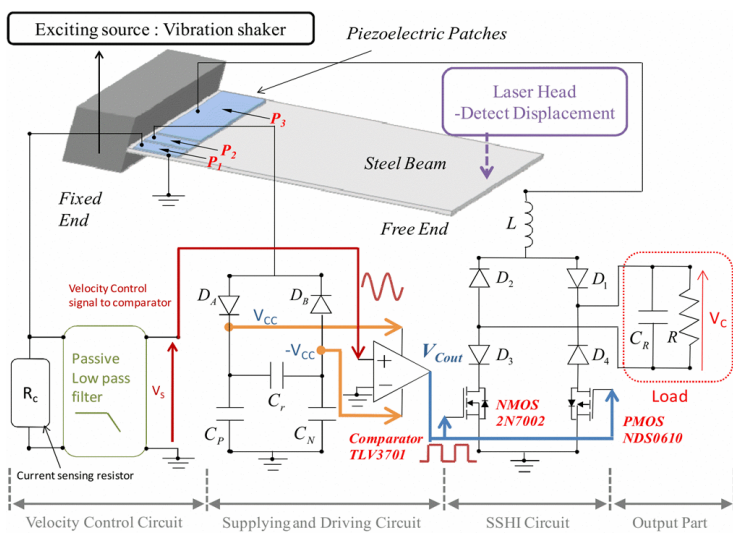
(a)



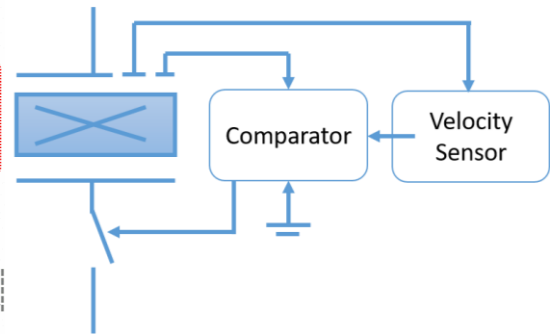
(b)



(c)



(d)



(e)

Figure 1-33 Electrical autonomous switches

(a) Implementation of autonomous switch, increasing the bandwidth of energy harvesting by designed IC [75] (b) the original self-powered smart switch [73] (c) simplified model of the smart switch (d) velocity controlled method to detect switching time [78]) (e) simplified block diagram for velocity sensing switch [78]

Regarding the smart switch, using the semiconductor components as the electrical switches, it was not “off” for real. The off state of the smart switch can be seen as a high impedance load, which in result, caused high losses in S-SSHIs when low power is supplied. The energy loss of the smart switch will be further discussed in Chapter 2

1.4.2.2 Mechanical Switches

As mentioned, the electrical methods consume some power to drive the switches. On micro or MEMS devices, the output power may not be abundant or even too little to drive the smart switches, not to mention dividing the piezoelectric patch. As a resolving method, mechanical switches proposed in [27, 33, 79] do not require energy to trigger, but hinders from physical situations. In other words, mechanical switches consist of electric contact pads that requires to be physically triggered-when the beam reaches certain level of deflection, the switch component on the stopper is impacted and switched on. That would indicate the problem: if the base driving displacement is too small, the switching location is not reached, thus cannot be switched on. Moreover, the physical impacts on the cantilever beam itself also shortens the lifespan of the device, causing a faster fatigue and may also create large noises. Examples of mechanical switching methods are shown in Figure 1-34, showing impacting switches in Figure 1-34 (b-c) and sliding electrodes as switches are shown in Figure 1-34 (a). On one hand, stoppers create the broadband effect, which would be mentioned in the following section 2.3, on the other hand, the rectifying can be performed by the contact.

Another method was proposed by H. Liu [80] with a parasitic oscillating structure on the tip of the beam to side step the mechanical impact. In this method, the main structure would not be damaged during the conducting instances. As far as the main structure is concerned, if the switching element fails, the harvesting can still be working, thence stability can be maintained.

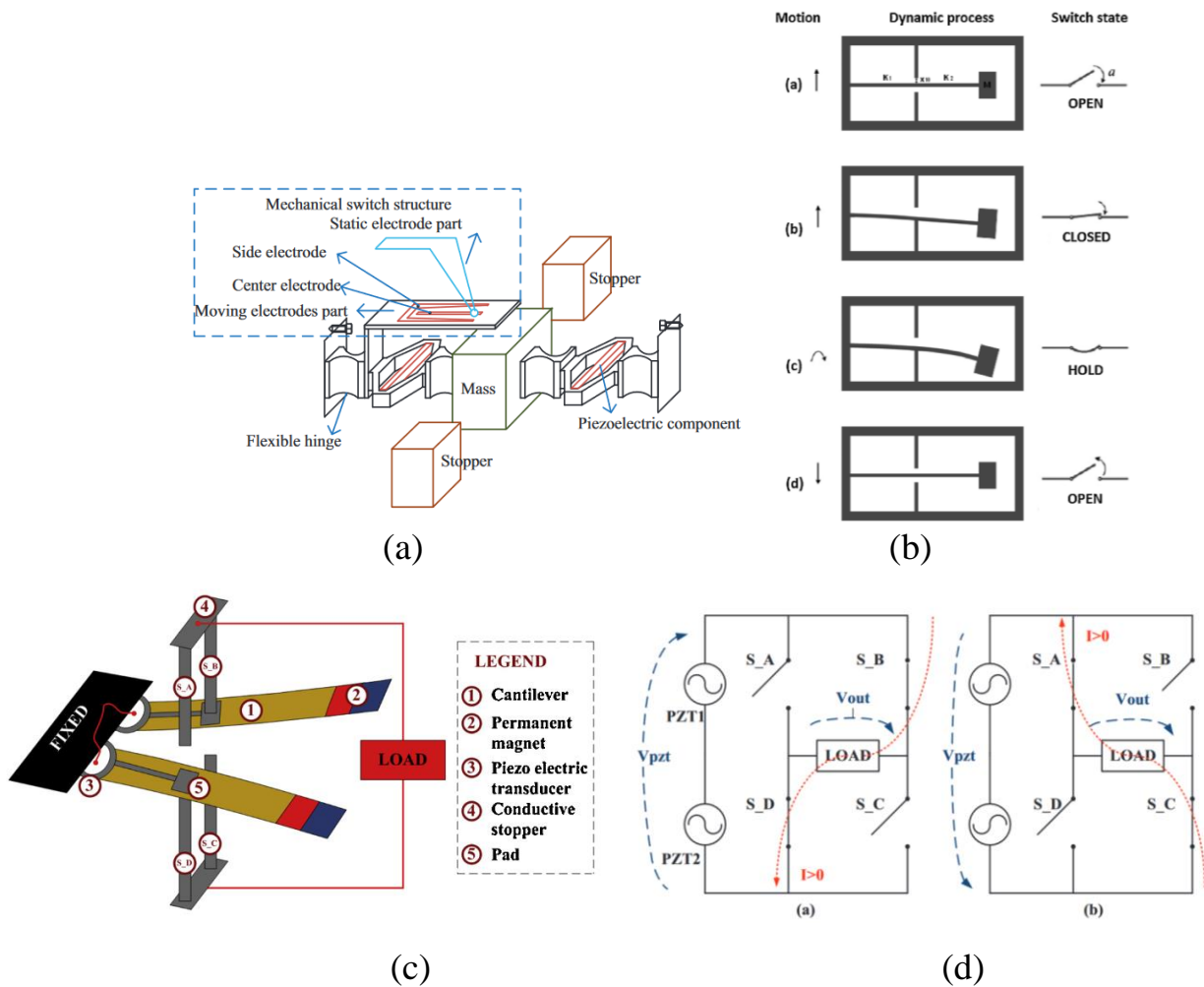


Figure 1-34 Mechanical switch designs

(a) with sliding electrode [41][33] (b) integrated stopper with switch [27] (c) a stopper-switch based threshold free rectifier [81] (d) the switch control flow of [81] to realize the rectification

1.4.3 Multiple Beam Circuitry

To connect multiple beams for best output, [82, 83] investigates about the circuitry connection and models of the beam arrays using SSH techniques. Conclusions show that the P-SSHI connection has a moderate power output but the widest bandwidth, whilst the S-SSHI holds the highest output at the cost of the bandwidth. SEH has the performance in between.

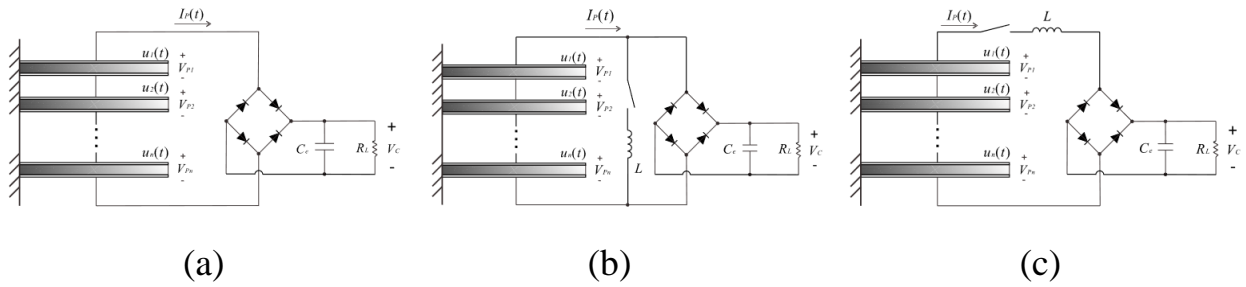


Figure 1-35 Circuit connection for cantilever arrays [83]

(a) beam connected in series, SEH (b) beam connected in series, P-SSHI (c) beam connected in series, S-SSHI

Another circuit proposed later in 2015 showed a promising connection circuit by using Optimized synchronous electric charge extraction (OSECE) to connect two beams[84]. The two OSECEs then charge the shared capacitance. Experimental results showed that the summation of the two beam outputs is almost linear and almost lossless.

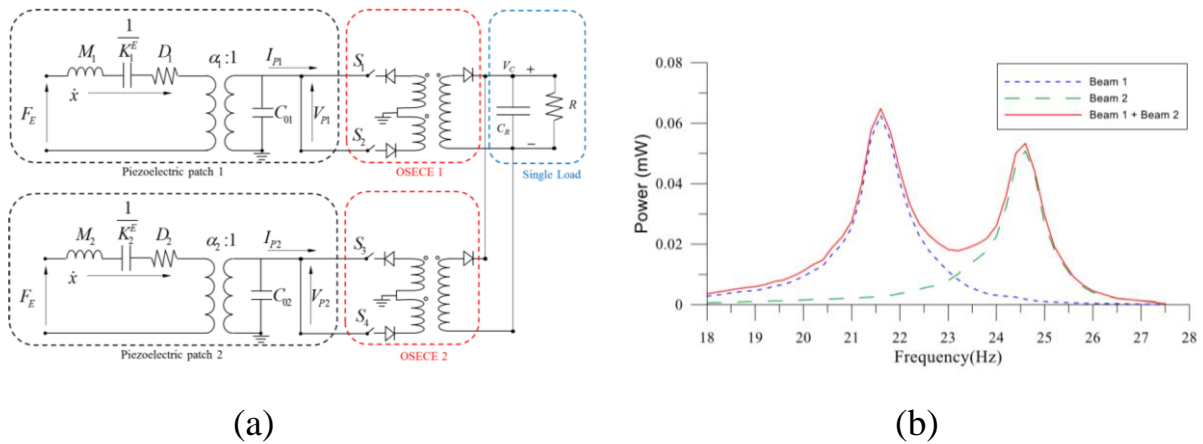


Figure 1-36 Connecting two beams using OSECE [84]

(a) circuitry arrangement (b) experimental results

1.5 Dissertation Organization

In this work, the following chapters are organized as follows:

Chapter 1 introduces the motivation and aim of this dissertation. A general

introduction of all the techniques and backgrounds are presented. The models and techniques from the literature reviews which would be used in this work are also introduced in this chapter. The equivalent mechanical model and circuitry models of a piezoelectric cantilever beam are introduced. The SEH, P-SSHI, and S-SSHI are further discussed. Switching techniques for peak detection is also introduced. The mechanical means of bandwidth expansion models are also reviewed

Chapter 2 presents a simple model which is able to represent and calculate the power loss of the original smart switch for SSHI when it is driven in non-ideal power. A micro-PEH was used in this chapter as an ultra-low power source to drive the smart switch in both P-SSHI and S-SSHI.

Chapter 3 introduces the new hybrid electro-mechanical switching structure that has only the threshold voltage of a single diode. The switch structure consists of a pair of reed switch and its debouncing circuit. Different debouncing circuit were proposed and compared.

Chapter 4. uncovers a new bandwidth extension technique by connecting the beams within a beam array using magnetic force. By proper tuning, the usable bandwidths of the beams were extended, and the output power was also improved.

Chapter 5 Concludes the work, with summary of this work and the major impacts of this dissertation. Some basic concepts for future work are proposed for further improvement.

Chapter 2. Electric Circuit Losses: Modeling of a Smart

Switch Driven in Low Voltage

Attributing to the circuit topology and the inherited threshold, the smart switch for self-powered harvesting requires certain amount of energy to trigger. As the MEMS systems provide limited power source, the smart switch does not work ideally. In this chapter, the causes which lead to the losses are investigated and discussed. For instance, when the voltage is not enough, the diode does not work in the optimal resistance, and the impedance is greatly increased. Looking on the other side, the voltage required to drive the SSH, for example, S-SSHI is greatly increased by the voltage division due to the impedance of the load and that of the smart switch. Thus, a simple model for the smart switch under limited power supplying is proposed. Experiments are conducted to prove the model, pointing out the existing problem in the commonly used switching method.

2.1 Power Provided with Micro PEH Device

The micro PEH power supplying device used in this section is fabricated with the process proposed in [10]. The structure of the generator and the fabricated beams can be found in Figure 2-1 (a, b).

To investigate with different power supplying situations, two different types of Micro PEHs are used: 1. A typical uni-morph d_{31} device, which consists of a substrate (stainless-steel), with a PZT layer (1st PZT layer), and an electrode (top electrode). 2. A bimorph configuration beam consisting of two PZT layers sandwiching the stainless steel substrate, with the coverage of the top and bottom electrodes. Among the two, bimorph devices have the advantage of the variability of

power sourcing, shunt, or series connections can be poled depending on the demand of higher current or higher voltage source.

As far as the bimorph structure is considered, the top and bottom electrode consists of titanium (20 nm) and platinum (200 nm); the thickness of the stainless steel is 50 μm ; and each of the single PZT layer is 10 μm thick. For the uni-morph device, the substrate used was a 30 μm stainless steel, and the PZT layer was 15 μm thick. The length and width of the beam is 8000 μm and 6000 μm , respectively, for both of the bimorph and uni-morph devices. A tungsten proof mass was attached to the end of the beam to lower the resonant frequency of the bimorph structure, which is targeted around 120 Hz. The size of the tungsten proof mass is 4000 μm \times 6000 μm \times 1000 μm for the bimorph device, and 400 μm \times 6000 μm \times 450 μm for the uni-morph.

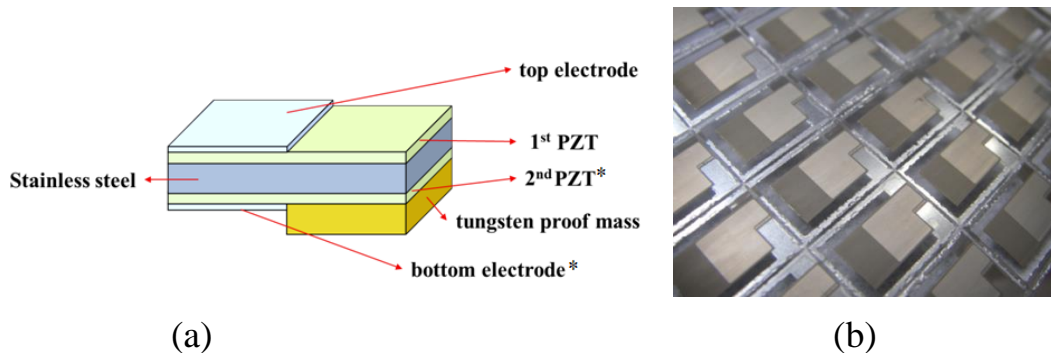


Figure 2-1 Schematic diagrams of the piezoelectric MEMS generator. [10]

The starred content exists in the bimorph structure only (a) beam structure (b) fabricated beam.

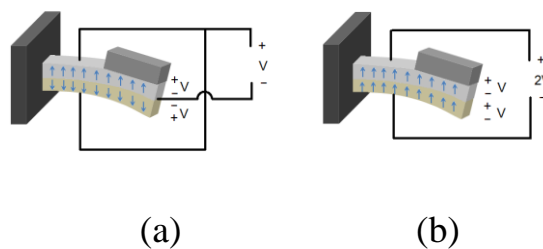


Figure 2-2 Schematic diagram of bimorph poling and connection

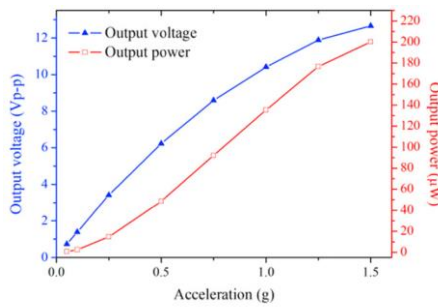
(a) parallel connection (b) series connection

Using the lump parameters, we can model the performance of the devices. The lump parameters listed in Table 5 were obtained using an impedance analyzer. The C_0 and k^2Q_M varies in the two d_{31} devices due to the fabrication discrepancies. These parameters will be utilized in the following sections.

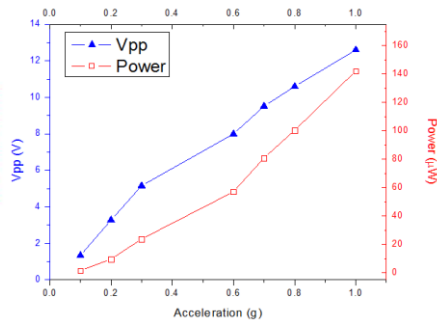
Table 5. Lump parameters derived through a network analyzer for the d_{31} and bimorph devices used in this section

Beam	Bimorph Parallel	Bimorph Series	d_{31} #1	d_{31} #2
C_0 (nF)	13.9	3.4	4.78	4.5
f_0 (Hz)	88.97	95.02	124.3	125.7
f_1 (Hz)	88.06	96.10	125	128.8
k^2 (%)	2.02	2.2	1.1	0.418
Q_M	35.62	35.19	7.92	41
k^2Q_M	0.72	0.68	0.87	0.172

The standard AC mode is used as a standard to compare the power enhancement ability of the SSHI technique, and the power losses of the rectifying circuits. In the following Figure 2-3 (a,b), the power outputs of the two types of micro PEH are shown. Under a 1 g excitation level, the uni-morph device was able to supply $134 \mu\text{W}$ with a voltage output of $10 V_{pp}$, whereas the bimorph device gave $143 \mu\text{W}$, with $12.8 V_{pp}$.



(a)



(b)

Figure 2-3 Power and voltage outputs of Micro PEH excited with varying acceleration levels
(a) a typical uni-morph device (b) a typical bimorph device (in parallel),

2.2 The Circuit Loss

2.2.1 The Rectifying Loss

Diodes are essential components for rectifying the piezoelectric voltage to DC output in order to store the harvested energy and to supply electronic devices. A typical diode component 1N4148 is used in this work to observe its power response, with a fixed given voltage of 21 V. The inverse current loss, which is merely a few nano-amperes, will be ignored in this work. From the experiment, we have noticed that, even with enough voltage, the current that is limited will determine the threshold voltage of the diode. Experimental results showed that, while the threshold point of the diode is not reached, the power that is consumed increases in a more quadratic trend. Subsequently, when the threshold point is passed, the curve becomes more linear due to the resistance that is greatly reduced over threshold. It is also known that the current output of the device is quadratic relative to the acceleration of the device, that is, exceeding certain acceleration will smooth the power loss ratio. In another term, it would mean that the power loss due to the diode loss is critical when the current input is limited by the size and the external acceleration driving the PEH.

A full bridge IC DB105 was used to evaluate the power loss of the standard harvesting circuit, where the maximum voltage drop is around 1.1 V according to the manufacturer's datasheet. Experimental results show that, under low voltage inputs, most of the energy is consumed by the diodes, yielding an almost null harvested power. As we elevate the acceleration to 0.5 g, where the power input comes to 60 μW , the voltage input comes to 3 Volts RMS to the optimal load of 150k Ω .

Meanwhile, the overall power output is around 30 μW , with the voltage input equal to 2.12 V_{RMS} . It could be estimated that the voltage drop is around 0.88 Volts, with the loss of around 50%. As the power input comes to 100 μW , the input voltage reaches 3.87 Volts, whereas the harvested power is 52 μW , with 2.79 Volts. From a voltage difference of 1.07 Volts, the real R_{on} of the diode stands (or in other words the threshold is reached). From this point, we can observe the loss power ratio begins to slow its slope as the threshold is reached. Thereby, if the current can be raised in certain way, the inherited characteristic of the PEH will provide enough voltage to drive the rectifying bridge in a less power consuming way.

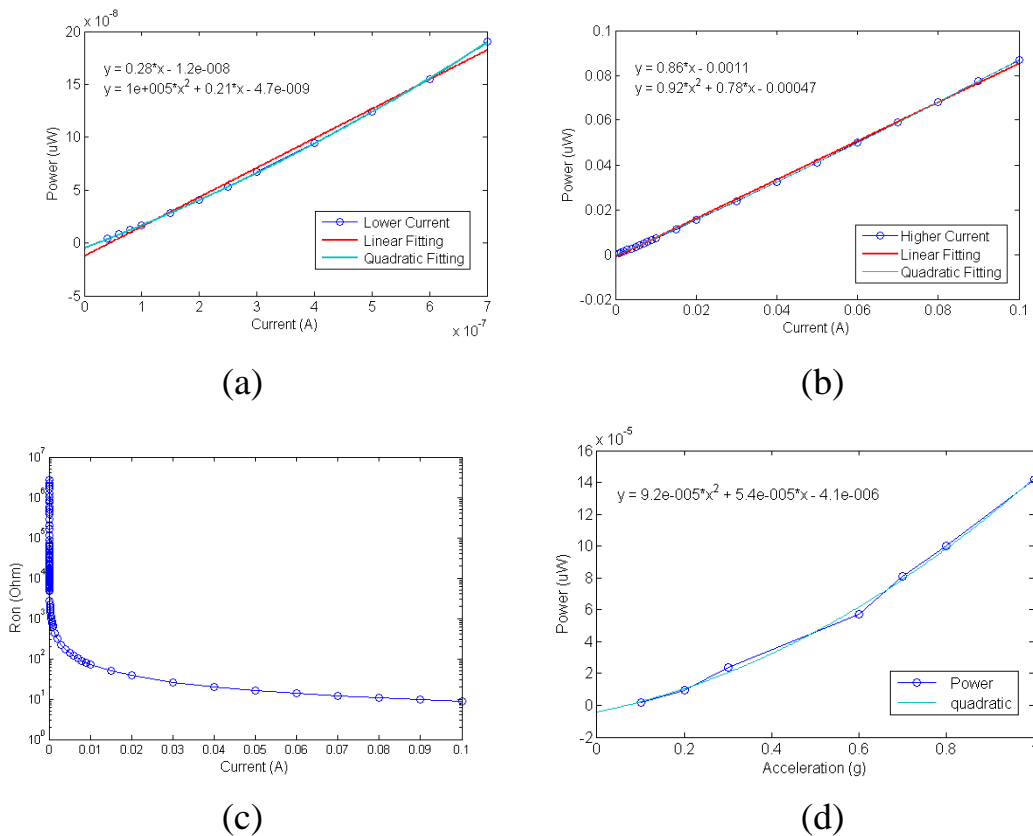


Figure 2-4 Diode Analysis using Keithley 2420 source meter

(a) diode loss with scales of micro-amps, (b) diode loss with scales of milli-amps (c) R_{on} of a diode in respond to current (notice R_{on} in log scale) (d) power output curve fitting of one MPEH.

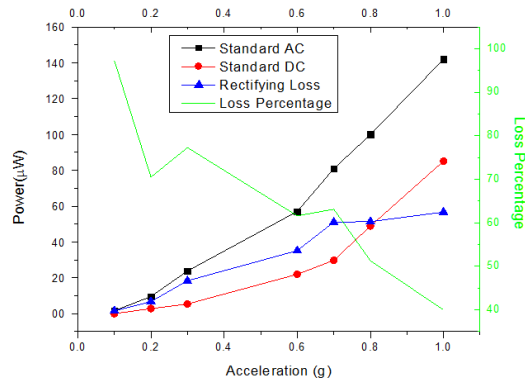


Figure 2-5 Rectify loss experiment of IC DB155

2.2.2 The Smart Switch Loss

The concept of the self-powered switching technique is shown in Figure 1-33 (b). The exact circuit can be found in Figure 2-8 (a). The switch is composed of two parts, the peak detector and the switching component. The peak detector consists of a comparator, which is used to compare the output voltage of the energy harvester with its envelope. From Figure 2-8 (b), one can read that, as the signal falls to a level lower than the envelope, the comparator gains the information and sends a signal to the switching component to turn on the single-direction switch. [85, 86] had proposed solutions to execute this concept. Several researches had also showed their effort on optimizing this circuit [87]. Both of the proposed solutions utilize transistors as the comparator, which in consequence, rose up the voltage requirement of the self-powered switch. In this work, we have used the solution of self-powered SSHI (SP-SSHI) proposed in [72] to analyze the energy flow.

According to the literature, a single switching process can be divided into 4 phases: the charging, the transition state of inversion, the inversion, and the rebounding of oscillation, as depicted in the following Figure 2-6 (b-e). Figure 2-6 (a) gives an overall view of the switching waveform.

In the first charging stage, the two capacitances of both directions are charged,

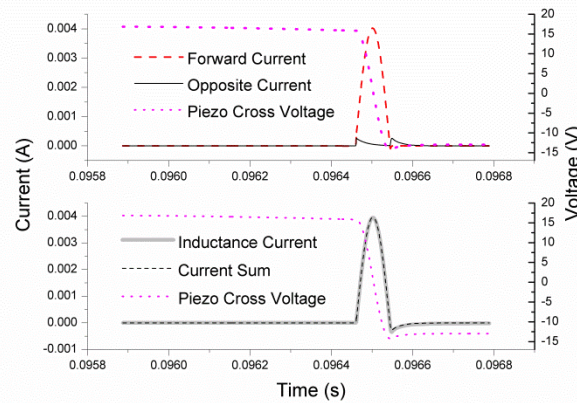
one through the diode, another on the opposite switch, by the PN junction of the transistor. Using a transistor enables the capacitor on the opposite switch to follow the input voltage, but is also one of the passageways of the switch loss. Afterwards, as the voltage of the forward capacitance is charged to the level of the input voltage, the input voltage starts to drop.

On the transition state of inversion, the transistor will be switched on when the V_{BE} overcomes its threshold which enables the discharging of the capacitor to charge the FET effective capacitance. This turns on the switch, which triggers the LC resonance of the inductance and the C_0 of the PEH. In consequence, the voltage starts inverting as the massive current passes through the inductance via the FET switch. On this instance, the massive current flow will pull the current of the opposite switch to its diode-restricted direction. As a result, the capacitor starts its first own voltage inversion. The charging of the opposite capacitor will cause a small leakage through the FET switch for a short instance until the voltage reversion, which may cause another minor passageway to the power loss. It is small enough to be ignored for now.

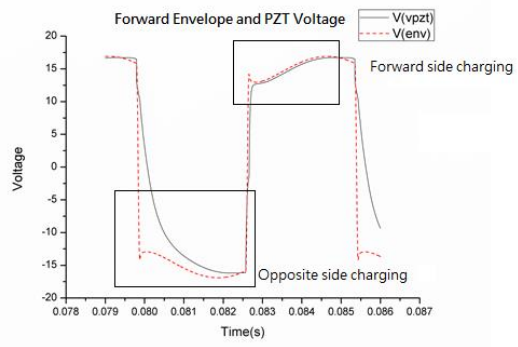
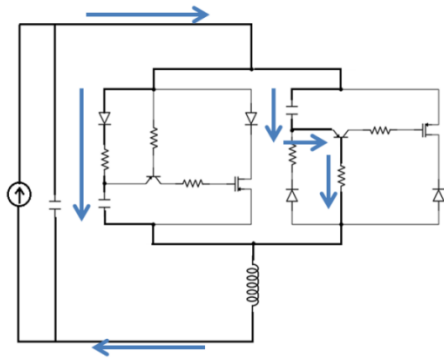
When the switch is totally on, or when the real inversion starts, the FET of the opposite is totally off due to the reversion of the voltage. Then as the LC oscillation comes to the negative current, it does not stop abruptly.

A rebounding occurs in consequence. In this time, it also gives an overshoot peaking to the waveform, which also makes the inversion non-ideal, as shown in Figure 2-7 (b, c). During this stage most of the negative current is blocked by the forwarding diode, the remaining energy damped by the circuit through three routes: 1. Charging of the opposite capacitance 2. Discharging of the forward capacitance by the leakage through the PN junction of the forward switch 3. A minor leakage of the FET switches due to the instant rise of the capacitance and current.

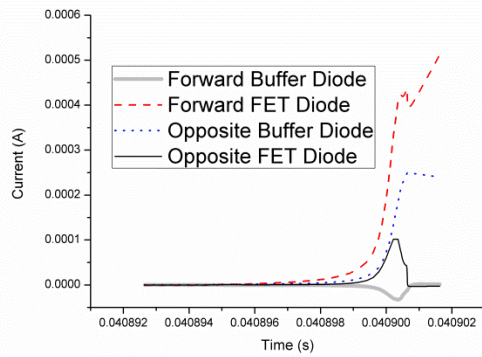
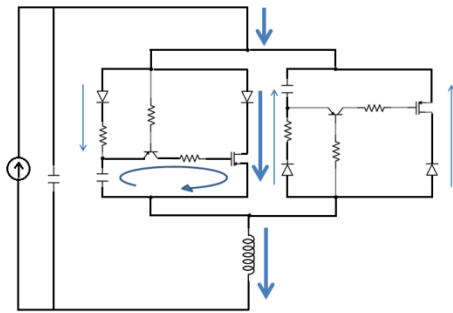
The charging of the opposite capacitance during this stage elevates its inverted voltage to match the envelope of the new inverted waveform, giving the initial voltage for the next opposite process where both capacitances are charged. On the other hand, as the discharging is complete, the current continues so as to start charging the capacitance to the other direction, which will be a first step in the opposite process. The value of the base resistors should be carefully chosen, or else the LC resonance will continue until it is totally damped. This phenomenon is caused by two reasons: 1. a mismatching of the damping resistance pair, causing the resonance continuation 2. an inappropriate selection of the resistance connecting to the base, causing the quantity of leakage current via the stopping switch. When the time constant of the pair is mismatching, worse cases of the oscillation can occur, bringing up more losses. The resonance current will be charged back into the capacitance of the piezoelectric device, as mentioned in [87].



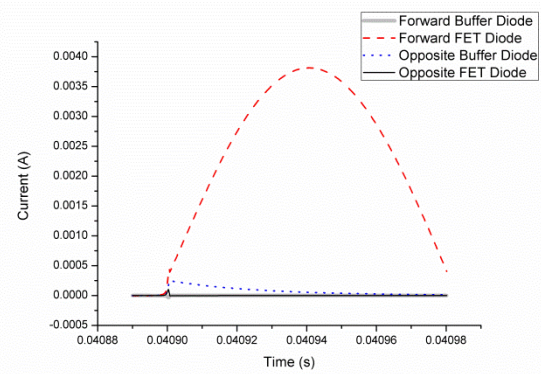
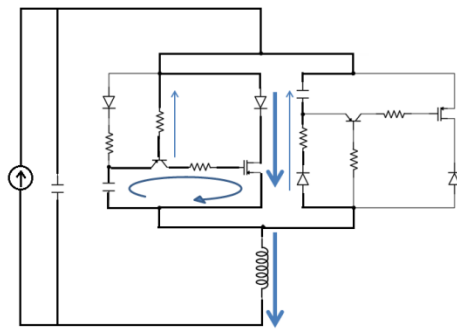
(a)



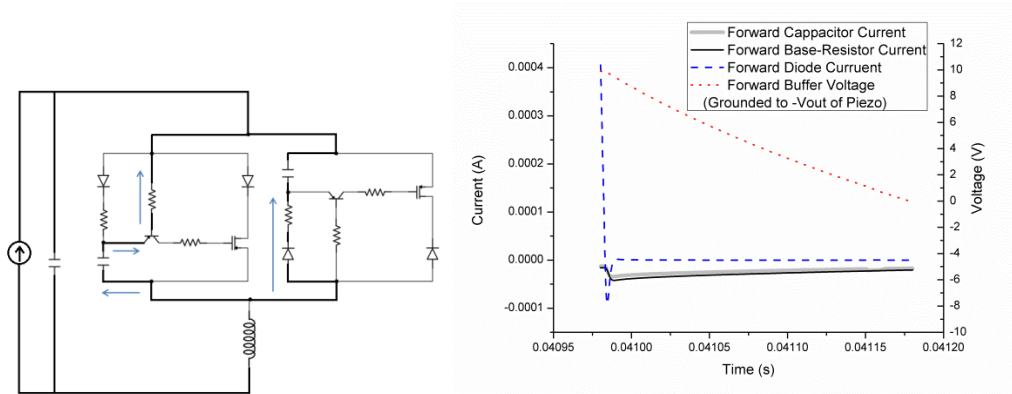
(b)



(c)



(d)

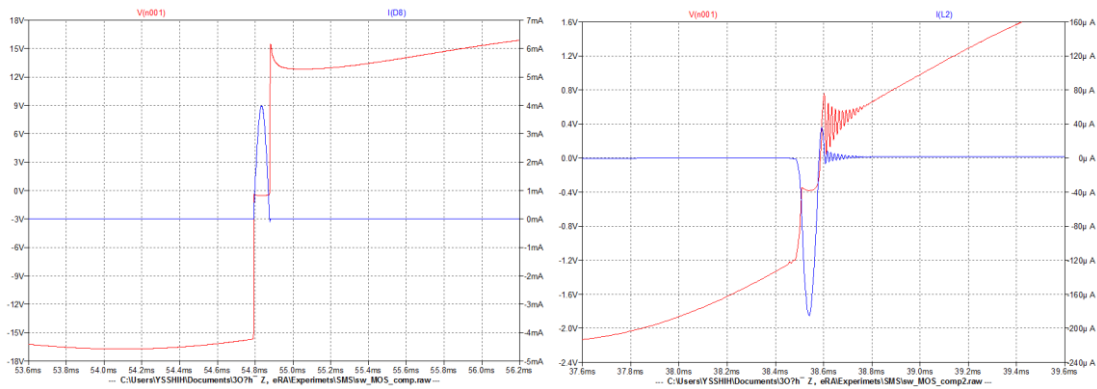


(e)

Figure 2-6 Diagrams showing different states of a SSH switching

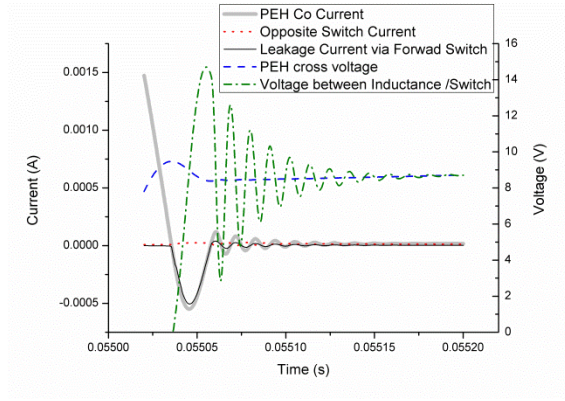
The circuit current flow on right, and waveform response on left

- (a) Overall look of the current and voltage response during an inversion
- (b) Capacitance charging state
- (c) FET capacitance charging state
- (d) Inversion state
- (e) Rebounding state, where the discharging of the left switch's capacitor, and the charging of the right switch's capacitor happens



(a)

(b)



(c)

Figure 2-7 Inversion investigations

- (a) proper switch voltage/current output (b) Current passing through the leaking / damping passage ways (c) The underdamping charging C_0 of the PMEH

3.2.2.1 Voltage requirement analysis of a conventional self-powered switch

With the knowledge of its working mechanism, one can then proceed to the modeling of the self-powered switch. To drive the abovementioned switch, certain level of voltage is required. But in micro-power harvesting, the voltage amplitude is usually limited by the size of the device and the applied acceleration, hence in this section we investigate the voltage requirement of the switch through a single direction switch (Figure 2-8(a)) which in pairs, composes the bi-directional switch. Figure 2-8(b) shows an simulated result zoomed in to the on-switching instance. Assuming the switch operating on the P-SSHI, we eliminate the cross voltage across the inductance, analyzing through the following steps. To turn on the switch, the voltage across the capacitance of the buffer should satisfy:

$$V_{Buf} \geq V_{EC} + V_{GS} \quad (2.2.1)$$

On the other hand, the voltage across the capacitance should also satisfy:

and series SSHIs. When the voltage does not exceed the required level, it is only restricted in working on the first stage. Hence the equivalent circuit for a half-cycle can be simplified with the following figure. The diodes are omitted for simplification. The cross voltage of the switch can be calculated, omitting the loading effect for now:

$$\begin{cases} V_{P-Switch} \approx V \\ V_{S-Switch} \approx V \frac{Z_{switch}}{Z_{switch} + R_{S-Load}} \end{cases} \quad (2.2.7)$$

Where it can be obtained that, assuming the RC pairs are identical,

$$Z_{switch} = Ls + \frac{1 + sRC}{2sC} \quad (2.2.8)$$

3.2.2.2 Loss analysis on charging-state

From afore mentioned analysis, two states are found to dominate the losses, that is, the charging state, and the rebounding state where the switch components are charged. A simple way to analyze the loss is to calculate the harvested voltage over the load in series SSH. We can then use the eq (2.2.9) derived from the simple model shown in Figure 2-9 (a, b):

$$V_{S-Load} = V \frac{R_{S-Load}}{Z_{switch} + R_{S-Load}} \quad (2.2.9)$$

Plotting the equation in to a bode plot(Figure 2-10(a, b)), we can find that it is a band pass equation, with a high passing frequency band. Therefore, it can be assumed that most of the energy is blocked by the switch in series under our operating frequency of 120 Hz. The following plot Figure 2-10 (a) shows that on 120 Hz ($\omega=754$ rad/s), the gain magnitude is around -15 dB, when the voltage is not enough to turn on. So we can also estimate that the voltage to turn on the series SSHI

is:

$$V_{s-PZT, \max} \geq (V_{EC} + V_{GS} + V_D) \div 0.822 \quad (2.2.10)$$

With all the current going through the same passage way, the consumption of voltage also indicates that the power consumption ratio of the switch is dominant under low voltage operation in the working range of 120 Hz. Only 17.8% of the energy can be harvested on the load.

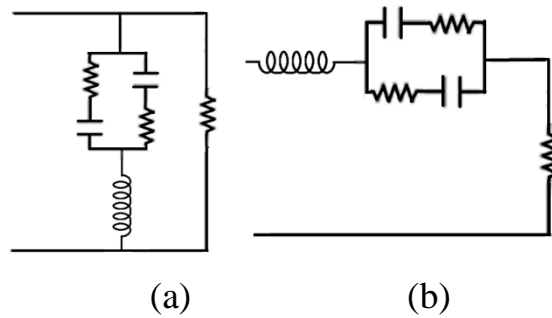
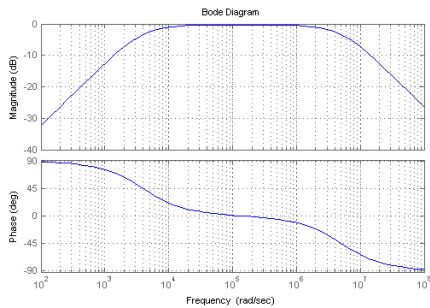
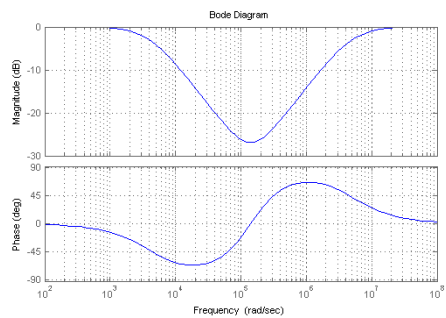
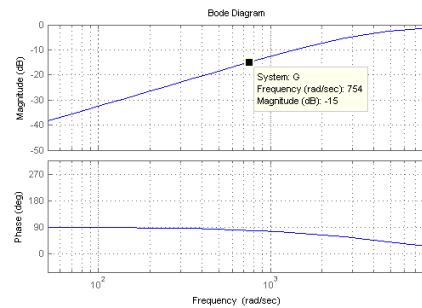


Figure 2-9 Circuit modeling of charging state during SSHI switch
(a) in parallel (b) in series



(a)



(b)

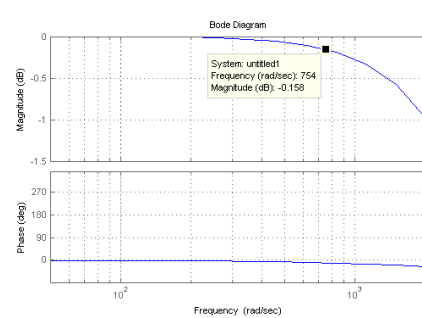


Figure 2-10 Bode plot simulation of the model on Matlab

using $R=56\text{ k}\Omega$, $L=125\text{ mH}$, $C=220\text{ pF}$, $R_{\text{load}}=600\text{ k}\Omega$. (a) left: transfer function over R_{Load} ; right: close look over R_{Load} (b) left: transfer function over Switch; right: close look over Switch

It is then possible to calculate the power loss of the parallel SSHI with the same fashion. With the same voltage input, the current is inversely proportional to the impedance of the components. Using the information already calculated above, we can assume that 82.2% of the current passes through the R_{load} , and the loss is around 17.8% using the circuit when the switch is not turned on.

2.3 The Loss Experiment

In this section, the smart switch was used in P-SSHI and S-SSHI under different power supplying conditions: voltage lower than threshold, voltage in between fully driven and the base threshold, and voltage more than enough.

2.3.1 Driven with voltage too low

Several self-powered switch loss experiments were conducted under different circumstances: provided limited power and enough power. Both experiments were conducted by different designs of the PMEHS mentioned above. Firstly, the experiment with non-ideal power input was performed using $d_{31}\#2$ showed in Table 5. The amplitude of the input voltage was 2.75 V peak. In this circumstance, where the sum of $V_{EC} + V_{GS} + V_D$ is considered to be around $0.5+1.9+0.6=3\text{ V}$, the switch is driven mostly in the first state. Experimental result (Figure 2-11) shows that, since the threshold of the FET shifts due to the current source, there is a slight lump on the parallel SSHI curve, on the location of which the optimal load exists. As for the series SSHI, most of the power is lost until the optimal load of the standard circuit is

reached. Calculating the percentage of the efficiency, it is quite close to the range of our estimation. Comparison of which can be found in Table 6

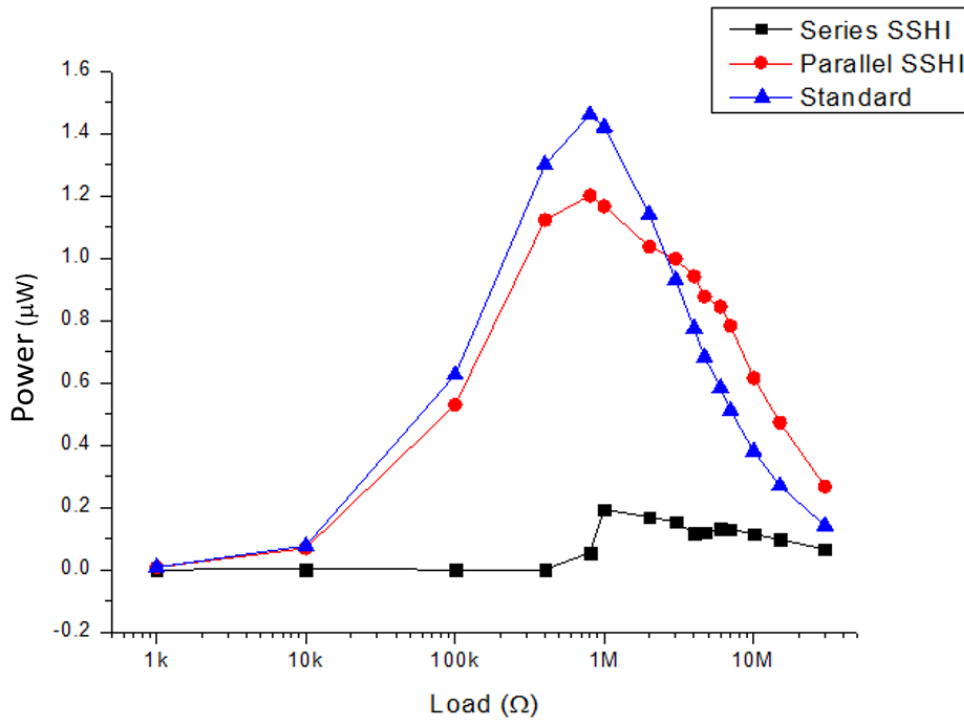


Figure 2-11 Experimental results of power outputs with voltage inputs less than requirements (2.75 V peak), d₃₁#2, parameters showed in Table 5

Table 6. Experimental results with voltage inputs less than requirements in comparison to estimated cases, $V_{oc} = 2.75$ peak

Circuit	Power Output (µW)	Efficiency (%)	Estimated (%)
Standard	1.46	100%	100%
Parallel	1.20	82%	82.2%
Series	0.20	13.7%	17.8%

2.3.2 Driven with voltage in between

To understand the transient response of the voltage for both SSHIs, the device was then accelerated to the output of 4.5 V peak Figure 2-12(a). Observing the optimal load can give us a glimpse that both the series and parallel SSHI are working,

but it is also obvious that the S-SSHI was performing undesirably with low efficiency. On the other hand, although the P-SSHI was still not working as ideal as it could be, it started its enhancing effect. It could be attributed to the inherited band-passing effect of the switch, which was connected series, having the current flowing through all the time to charge the easy to loss capacitance.

For further investigations, the voltage was gradually driven higher for the parallel SSHI, to observe the transient response of the rising voltage input. Results can be found in Figure 2-12(b). The MPEH was driven from 2.75 V peak to 4 V peak, which is 1 volt higher than the required voltage of 3 V. From the trend we can see the lump on the optimal resistance of the parallel SSHI starts to emerge, and is consequently dominant. It is noticeable that, parallel SSHI, which consumes less energy, has its enhancing effect starting on 3.65 V peak despite that on 3.5V, where the SSHI dominates the curve. The result can be owed to the power loss of the switch.

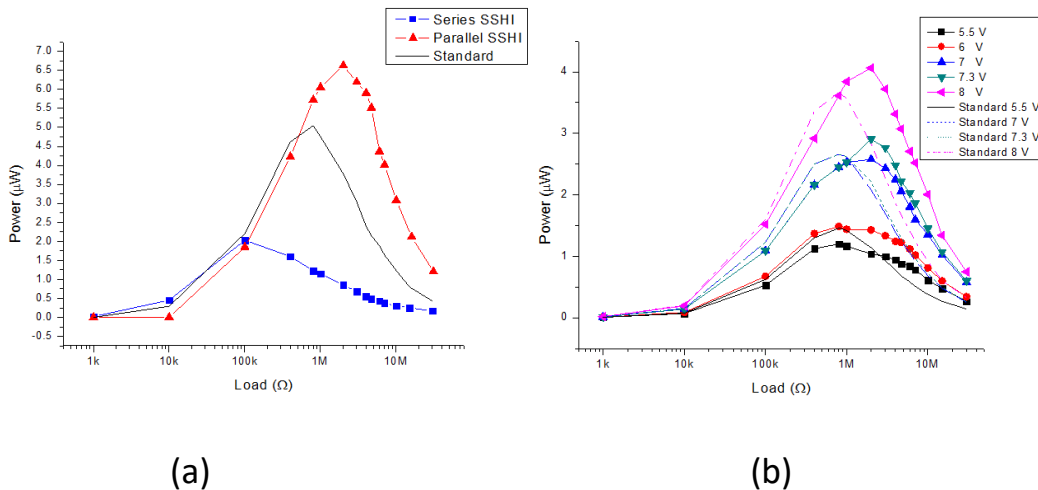


Figure 2-12 Power output results of transient voltage driven cases using $d_{31}\#2$, from Table 5

- (a) Series and parallel SSHI in comparison with standard circuit with 4.5 V peak input
- (b) Activation voltage test for parallel SSHI, where the piezo is connected in series (Input voltages in legend are volts peak to peak).

2.3.3 Driven with enough voltage

With input voltages high enough, e.g. voltage inputs greater than 6 Volts peak in our case, the SSHI could work more theoretically. It is also noticed that the optimal load is higher than the theoretical results. This phenomenon can also be attributed to the equivalent impedance of the switch on the off-state, which takes place most of the time. For instance, calculating the equivalent impedance using the parameters above used for Matlab simulation, we have $Z_{switch} // R_{load} = 586k\Omega$, with $R_{load} = 600k\Omega$. To increase the equivalent load to $R_{load} = 600k\Omega$, R_{load} has to be increased to $620k\Omega$, so that the matching impedance may take place again. Experiment results of the following experiment is shown in Figure 2-13(a-e).

Bimorph Connections in SSHI and Standard Cases

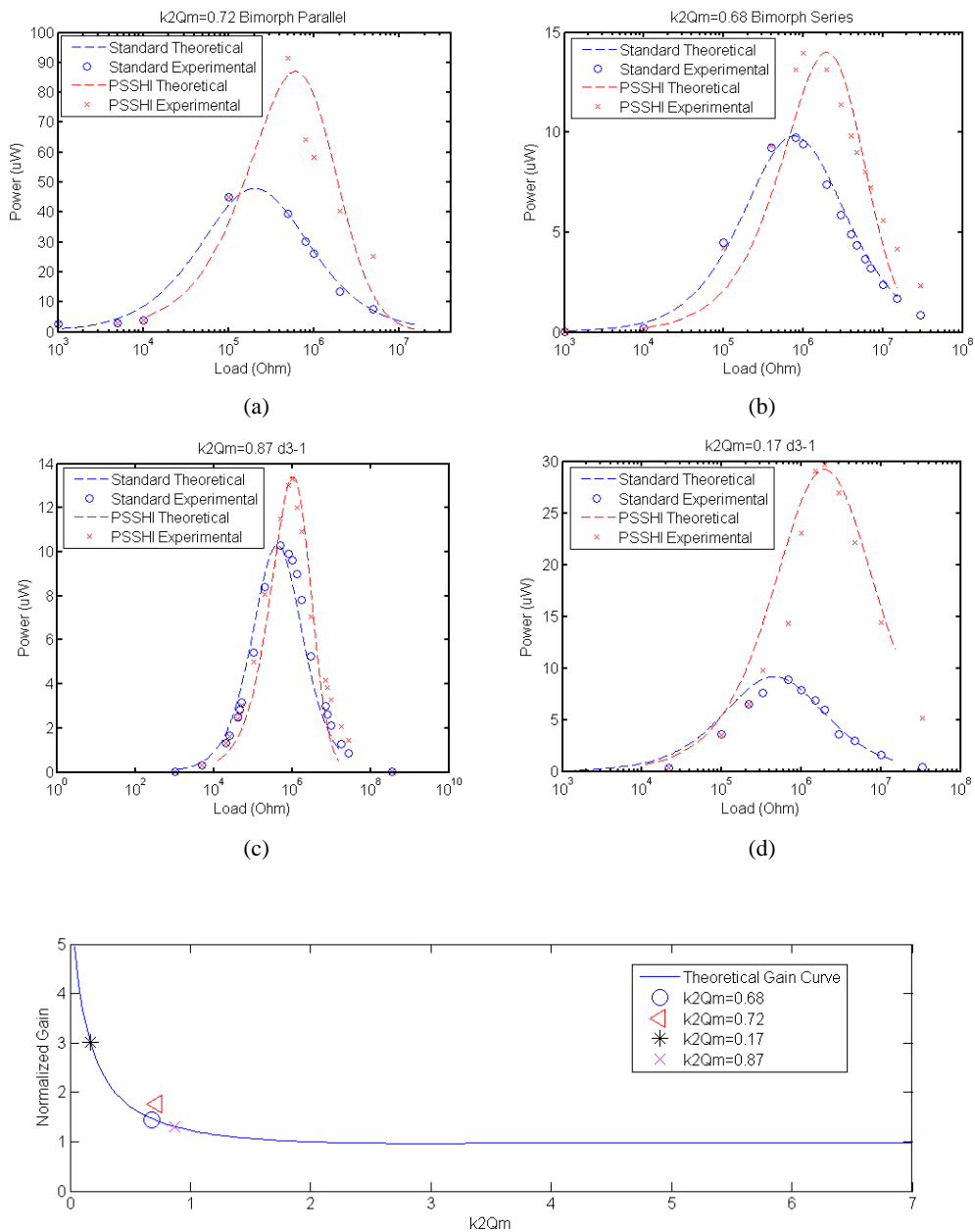
Shown in Figure 2-13(a), the parallel poled and connected device had a k^2Q_M of 0.72. With availability to give more than $90 \mu W$ under $0.75 g$, the harvested power with standard DC was approximately $44.9 \mu W$ due to the rectifying loss. Using the parallel SSHI DC with enough driving energy, the output came to $91.4 \mu W$, which was 2.03 fold in comparison to the standard technique. The experimental result can be found in Figure 2-13 (a). The power output was a little higher than the expected theoretical power gain. A series poled device shown in Figure 2-13 (b) with k^2Q_M of 0.68 had a gain of 1.44. The standard output was $9.72 \mu W$, and the SSHI output of $13.98 \mu W$. Results shown in Figure 2-13(b).

Connections with d_{31} in SSHI and Standard cases

The experiment was also conducted with two d_{31} devices with similar fabrication processes. The devices showed different k^2Q_M values and power outputs due to the fabrication process and the device characteristic design. Figure 2-13 (c) and (d) shows the experimental and theoretical comparisons of the two d_{31} devices. In

standard cases, both experiments met the theoretical optimal output of 10.3 and 8.89 μW , with the input voltage of $12V_{pp}$ $8.9V_{pp}$. When it comes to the P-SSHI, the overall optimal load shifted upwards for around $500k\Omega$. And the power was enhanced by 1.29 times and 3.33 times each.

To observe the efficiency, the output results are compared to theoretical curves with respond to the k^2Q_M in Figure 2-13(e). Theoretical curves are developed from the equations of [73].



(e)

Figure 2-13 Experimental results of parallel SSHI with power sources enough to drive SSHI.

(a) Bimorph in Parallel (b) Bimorph in Series (c) $d_{31}\#1$ (d) $d_{31}\#2$ (e) theoretical gain value

Beam parameters can be found in Table 5.

2.4 Discussion

Considering the basic component loss, the rectifying loss is restricted to its threshold voltage. We have used a bulk IC DB155 to have a greater scale of energy loss understanding. For other silicon controlled devices, such as transistors, when the PN junction is not fully conducting, similar responses cause a higher level of impedance.

The derivation with diode loss for SEH and SSHI are proposed in [73]. However, the authors considered the voltage output higher than the threshold voltage of the diodes. The proposed equations for SSHI considers only considers the circumstance of triggered switches, where the cross voltage over the diode is had met the stable value of the threshold voltage.

The smart switch design used in this work had a 3 V threshold in P-SSHI. Below which, the SSH techniques cannot be fully conducting and thus the harvested power is even lower than that of the SEH. In the case of S-SSHI, the threshold voltage was $3/0.822$ times higher due to the impedance voltage divide, approximately 3.63 V. However, when driven in 4.5 V, the power harvested from the S-SSHI was still limited. That is, the transient state of the S-SSHI, where the time delay should be taken in to account.

In the transient state, where the threshold is met, the efficiency grows with the input voltage, even if the provided voltage is greater than that of the threshold. It can be attributed to the switch delay loss, due to the voltage difference required to trigger the transistor (Figure 2-8 (b)). For the switching time delay loss, it will be

profoundly introduced in the next section. From Figure 3-20, we notice that the phase difference of 0.6 Rad will reduce the gain to 0.7 times. Referring to [88], a more precise calculation can be done for both SSH techniques within the transient zone considering the switching time delay.

Taking the overall response into account, from low power to abundant, we can refer to the modified switch analysis in [66], considering the topology, has the voltage detecting threshold similar to that of the P-SSHI due to the detecting envelope design located parallel to the EH. Nevertheless, the switch itself is located in series to the harvesting capacitance, and therefore would have the response similar to that of the S-SSHI. The harvested power of the SEH the modified SSHI comes to crossing point on 5.84 V for open circuit piezoelectric voltage. With V_{OC} below the threshold voltage was also not considered. Figure 2-14 shows the how the theoretical harvested power of SEH and P-SSHI changes in [66] and the experimental results in this work. The theoretical harvested power on the crossing point was 23.75 μW , with theoretical switch response omitted below the driving voltage. Nevertheless, comparing the experimental results in this work to the theoretical result of [90], the trend of the curves for the harvested power are similar. With components and transduced power different, the voltage on the crossing point in this experiment was around 3.5 V, and the corresponding harvested power of 2.5 μW .

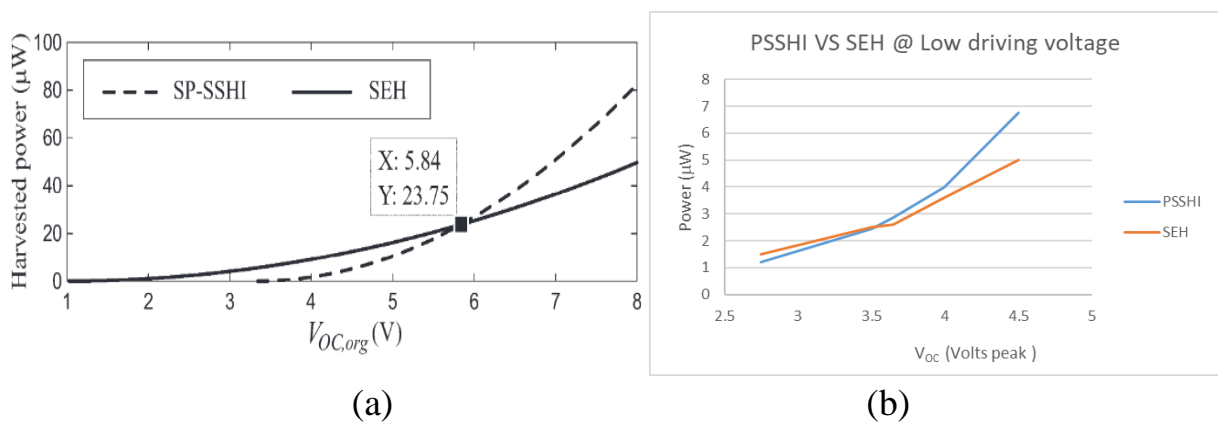


Figure 2-14 Comparison between the harvested power of self-powered SSHI and SHE

(a) Theoretical results from [66] (b) Experimental result in this work

Chapter 3. Hybrid Switch on SSH Methods

Regarding the circuit loss discussed previously, mechanical switches are used to avoid the excessive loss. To increase the stability and robustness, we choose to sidestep the physical impact of the main structure. In this chapter, reed switches are introduced to serve as the mechanical displacement detector and switch itself. Reed switches are easy to purchase and install. It is a mature device, where all sizes are available - from the size of bulk to MEMS (micro electronic engineering system). Reed switches are controlled by a magnetic field. Using this characteristic, it is used for non-contact displacement detection in this work. One should however note that, all mechanical switches suffer from the inherit problem of chattering. The chattering is caused from the bouncing of the mechanical switch blades, which does not settle until several micro seconds depending on the switch dimension.

In this chapter, the design concept of applying reed switches on SSH will be firstly introduced, along with the mechanical chattering problem and its resolving de-bounce method. Then the switching delay and the theoretical energy loss will be reviewed and discussed. Experiments are then conducted to inspect the loss due to the chattering, and the efficiency improvement of the resolving method. The switch delay loss experiment is also performed. Finally, the discussion inspects how different de-bouncing methods can be applied.

3.1 Design Concepts

3.1.1 Reed switch introduction

The point of using reed switch is to reduce main structure impacts with simple

adoption. The reed switches applied in this work can be easily purchased. Among the various types, the reed switch we use is a commonly seen glass sealed capsule. It is composed of two ferromagnetic blades, sealed within a vacuumed/inert gas-filled capsule, as shown in Figure 3-1 (a). When magnetic field approaches the pull-in (PI) zone, the blades attract each other and touch until the field leaves the drop-out (DO) zone.

Using a permanent magnet, PI is usually measured in distance, millimeters or inch. It could be also measured in field strength milli-Tesla or Gauss. When using coils, PIs are measured by, currents through the coil, volts across the coil, or ampere turns (AT). The drop-out could be measured in similar means as the PI measurement. The DO zone is a bit larger than the PI zone in attribute to the magnetic hysteresis. The hysteresis is usually expressed by DO/PI in percentage. Due to the difference of the reed switch design and fabrication, the hysteresis varies. The three parameters are to be used to decide the distance between the wavering tip and the reed switch itself.

Figure 3-1 (b) is a schematic diagram showing how the magnet interacts with the switch: As the single pole magnetic field enters the PI zone, the two conducting blades, differentiated in to two different leads, are induced with different poles, which would draw them together. The magnet then leaves the DO zone, to release the contacting blades. On typical usages, the main lobe which is in the middle is used for the switch control. There are also side lobes, smaller than the main lobe which are side effects created by the extension of the leads. On the brink of these side lobes beside the main lobe, as shown on the left of Figure 3-1 (b), it is overlapped considering the movement of the tip magnet. The bulky magnet would create a chaotic switching response if the magnet enters both PI zones, and the response is unpredictable. To avoid multiple triggering, the side lobe is used to operate the

switch.

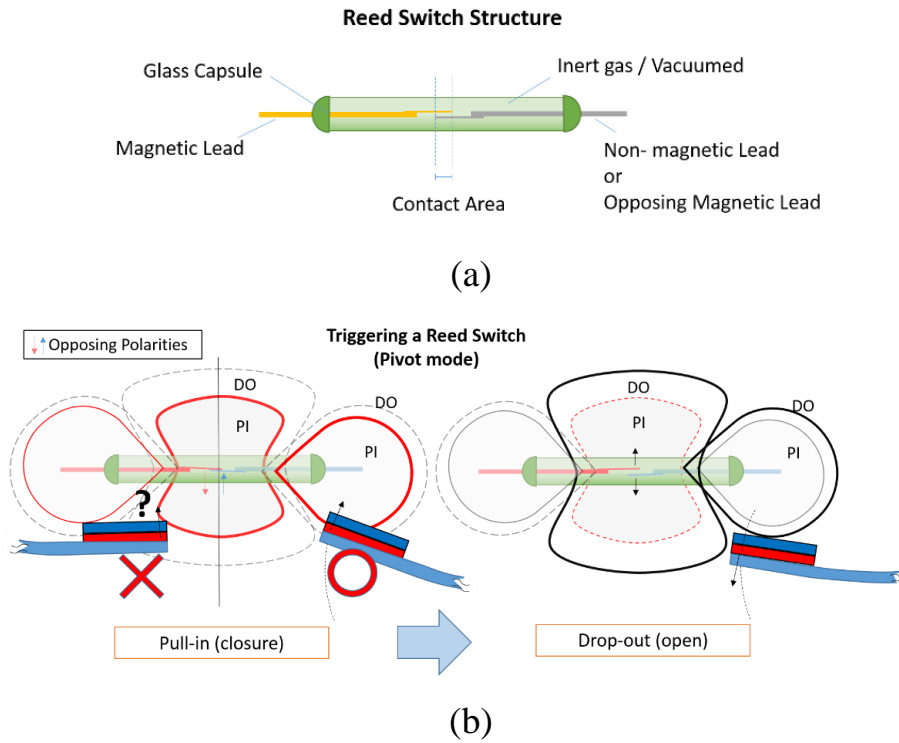


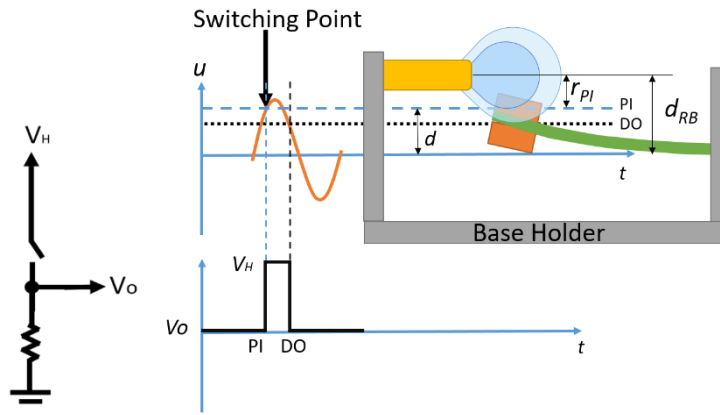
Figure 3-1 The glass sealed reed switch
 (a) Structure (b) operating a with magnet.

3.1.2 Reed switch replacement on SSH techniques

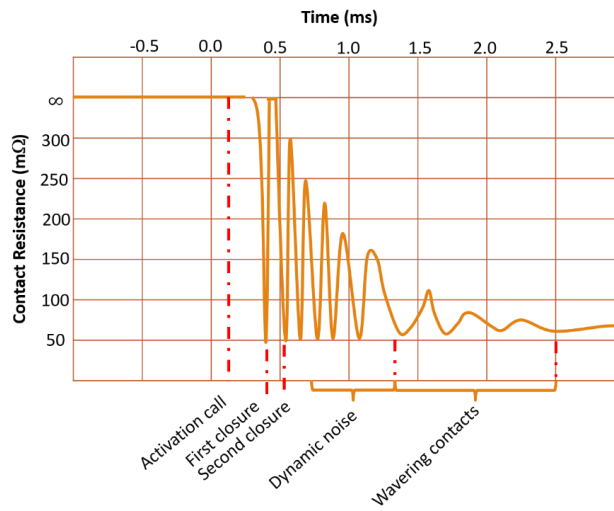
With the knowledge of how to operate the switch, we are able to utilize the reed switch on SSH techniques taking advantage of the characteristics mentioned above. The concept is as simple as such: Magnets are placed on the tip of the beams to serve as the proof mass and also the switch control. When the beam wavers to its extreme on vibration, the magnet enters the PI zone, pulling the blades together. Off as it leaves, the switch is then opened when the tip leaves.

A DC response experiment was used to test the chattering response and also the feasibility of the displacement trigger. A reed switch was placed above the cantilever beam, with a magnet at its tip. Figure 3-2 (a), indicates that, when the magnetic field enters the PI zone, the switch turns on, causing $V_O = V_H$. As the magnet leaves the

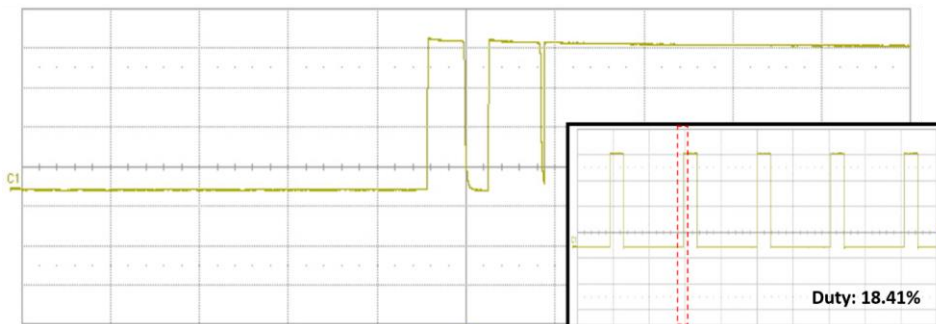
DO zone, the output is grounded to zero. By adjusting the distance d between the reed switch and the tip, the on switching duty can be tuned.



(a)



(b)



(c)

Figure 3-2 Reed chattering experiment

(a) experiment setup (b) DCR response, redrawn from Electronics [89] (c) The screenshot of the oscilloscope waveform for the chattering. The vertical axis is in 1V/div and the time scale is 50 μ s/div.

To investigate the chattering, it can be represented with the dynamic contact resistance (DCR). The DCR response during a call-close period can be represented as shown in Figure 3-2 (b). The plot shows that, after the activation call, the blades closes for the first time, with a bounce back reopening, then closes for the second, bounces open again, and the dynamic resistance oscillates until steady settle. This bouncing back is caused by physical contact blade bounce, which typically persists around 100 μ s, and 500 μ s for steady settle down. Zooming into the on-switching edge (Figure 3-2 (c)), one can observe that the chatter causes two reopening signals.

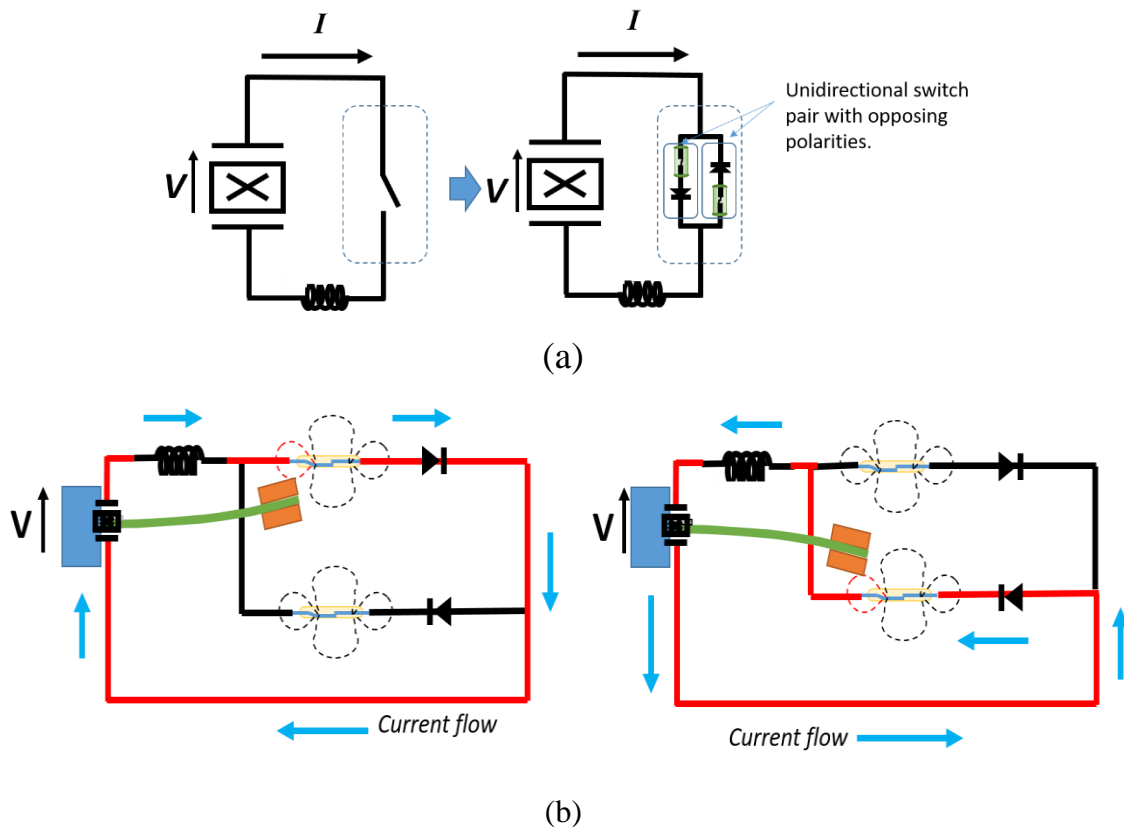


Figure 3-3 Applying reed switch on LF-P-SSHI

(a) switch replacement (b) working concept

To drive the SSHI, the switching should happen on both extremes. Therefore, two reed switches were placed, one up and the other below the tip of the cantilever beam. From the DC experiment, we noticed that the hysteresis delay prolongs the on-switching duty, lasting for multiple LC resonating periods. However, in SSH techniques, the inversion is caused by a single direction pulsed current, or in other words half the LC resonance. Thus, a diode was required to prevent the current back flow, one for each flow direction. Figure 3-3 shows how reed switch is applied in LF-P-SSHI. Each diode-switch pair is a unidirectional switch, and by placing two pairs with opposing polarities, a bidirectional switch is formed as shown in Figure 3-3 (a). Figure 3-3 (b) shows how the tip triggers the reed switch, with the conducting current flow of different directions on the opposite sides.

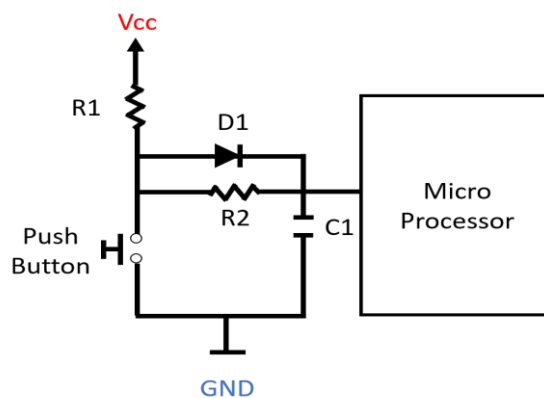


Figure 3-4 Conventional snubbers used in microprocessor controls

3.1.3 Resolving the chatter: snubbers (de-bouncers)

As mentioned, almost all mechanical switches subject from chattering. To control micro possessing units, push buttons are often used. It is a widely-known method to limit the chatter (de-bounce / snub) by adding a RC buffer, so that the voltage can be held with little ripple, as shown in Figure 3-4. That, gives the first

version of the reed de-bouncer: the resistor-capacitance snubber (RC snubber). However, in microprocessor applications, the energy supply is usually well enough and is needless to consider. Hence, resistors are used, regardless of its power consumption. Theoretically, an ideal inductor does not cause energy losses. Thus, to reduce the energy loss, the inductor was introduced to replace the resistor to become the LC snubber. Then, a third design was revealed, the silicon controlled rectifier (SCR) de-bouncer. In this section, the three types of snubbers are introduced.

3.1.3.1 Reed de-bounced on Resistor (RDR)

Using resistor-capacitance to de-bounce, or snub, Figure 3-5 shows the first adopted de-bouncing technique similar to that of Figure 3-4. Figure 3-5 shows a unidirectional switch, as mentioned in the last section. The snubbing method would be denoted as RDR (reed de-bounced on resistor) in the rest of the text. The snubbing mechanism is identical to that of the conventional snubber. The RC circuit forms a low-pass filter which would prevent high frequency signals from passing, for instance, the chattering. When the switch is on, the capacitor of the RC is charged, and would hold the voltage with a small ripple even if the switch bounces on and off for several times. Hereby, we can say the signal is snubbed (or filtered). This capacitance would keep the MOSFET on, until the capacitance is discharged or the diodes stop the current flowing from the other direction.

The RC circuit forms a first order filter, with its cut-off frequency obtained by the equation $f = 1/2\pi RC$. For our application, the RC filter is designed to filter away the chattering frequency, and its cut-off frequency should be higher than the resonance of the SSH LC resonance, which is $f = 1/\sqrt{2\pi LC_0}$. The chattering frequency can be observed with experiments. Usually, the chattering frequency is two or more orders higher than the targeting LC resonance. One should note that the

capacitance should be small enough to filter the chatter frequency, but also high enough to store energy for driving the MOSFET. A semi-empirical method to estimate the on-power of the MOSFET can be used by referencing the component datasheet. The leakage current for the MOSFET in the operating voltage can be obtained from the datasheet and the appropriate range of the capacitance value can be derived accordingly. For a reference, in our experiment, the capacitance is in the range of 0.68~68 nF.

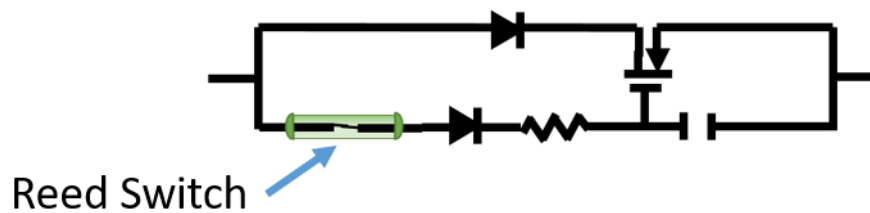


Figure 3-5 Unidirectional reed switch de-bounced on resistor (RDR)

3.1.3.2 Reed de-bounced on Resistor (RDI)

To have a sharper filter, and also less energy consumption, the LC snubber was used. The LC snubber would be denoted as RDI (Figure 3-6), for the following of the text. Ideally, the inductors are non-power consuming. Thus, by choosing appropriate inductors, the power consumption should be less, providing a sharp filter of second order.

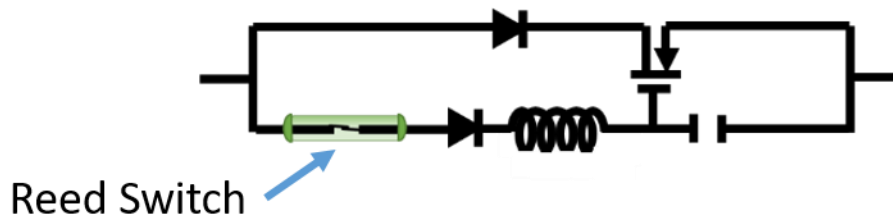


Figure 3-6 Unidirectional reed de-bounced on inductor (RDI)

3.1.3.3 SCR de-bouncer

For further improvement, the SCR configuration was proposed (Figure 3-8). SCRs are semi-conductor devices formed of a stack of four-layered-PN junctions, usually use to handle massive energy. The SCR composing structure is shown in Figure 3-7.

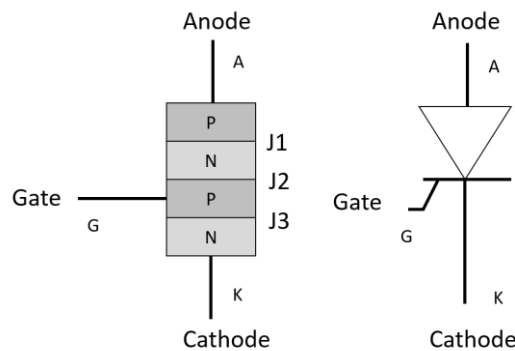


Figure 3-7 Schematic diagram of SCR

To on-trigger the SCR, the gate current I_{GT} is used. However, the gate current can only launch the conduction. The off-switching of the device is determined by some other instances:

- (1) Reverse the voltage over the anode and cathode V_{AK} ,
- (2) Lower, cut off, or reverse the passing current I_{AK} .
- (3) Provide a large amount of reversing gate current I_{GT} (Gate turn off). This is usually not considered due to the great amount of current.

This characteristic is appealing, for it meets just what SSH techniques require: to stop the switch on current reverse. That would mean, the diode can be omitted in the electrical switch since the SCR is a diode itself. However, most SCRs are used in power electronics, which also hints that it may not be suitable for low power

applications. Most SCRs have high leakage currents, which may even be at the scale of the max current of piezoelectric energy harvesting. Thence, the SCR applied should be chosen with care. High sensitivity and low power dissipation is required. In this work, P130AA of STMicroelectronics is used for its low I_{GT} , which is merely $0.1 \mu\text{A}$. With such low trigger level, the component is suitable for piezoelectric outputs, which has high voltage output but limited current.

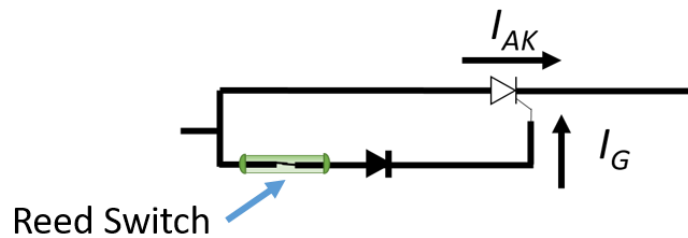


Figure 3-8 Unidirectional SCR de-bouncer

It is also noteworthy that, for SCRs so sensitive as P0130AA, the reverse gate voltage V_{RG} is also quite low (8 volts). The PN junction may break down if the gate-cathode voltage exceeds this value, resulting in false conduction. Therefore, the operating voltage should be considered, or a protecting component should be applied to avoid this incident.

3.2 Energy Loss Due to Switching Phase Difference

In this section, the energy loss due to the switching delay is investigated. It was already discussed in [88] that, the switching instance is usually non-ideal in practical applications. We will take the originally proposed smart switch from [73] as the first example. Figure 3-9 (a) shows how the phase difference occurs with smart switches.

As mentioned, the buffer voltage (V_{buf}) created by the resistor and capacitor was used for detecting the peak. Creating a second signal, V_{buf} , has a short time lag after the piezoelectric voltage V . Right after the extreme, the fall of V crosses with the rising V_{buf} . Ideally, this is the switching point, which has only a short phase lag. Yet, to compare the two signals, a transistor was used. Attributing to the PN junction characteristics, the threshold voltage has to be overcome to switch the transistor. The voltage threshold causes another time delay after the crossing point. In all, time τ was delayed, and the phase lag occurs.

For reed switch applications, the ideal switching position should be on the extremes of the displacement, otherwise phase differences or no switching would occur. Nevertheless, it is impossible to ensure that all displacements are perfectly switching on the extremes during actual usages. Thereby, a margin zone of the relationship between the tip and the switch location may be defined for better tracking. Figure 3-9 (b) shows how the difference is caused. The dotted line indicates the brink of the PI zone: below this line, no switch is triggered. The distance between the tip at settle and the PI zone is defined as d . To ensure that the magnet enters the PI zone, the maxima tip displacement u can be drawn closer to the reed switch so that $u > d$. In consequence, the switching time would be earlier than the tip extreme, and a phase lead was caused.

Severe phase leads and lags cause the deduction of energy harvested. An adequate zone can be designed to control the energy loss, and the good zone can be defined. When the tip overshoots the good zone, it would be considered as an inadequate drive due to the undesired energy loss.

For the reed switch application, the relationship between the leading phase and the tip displacement can be represented as below:

$$d = u_M \cos \theta \quad (3.2.1)$$

Referencing [88], we are able to derive the power harvested from the P-SSHI and S-SSHI considering the phase lead and lags with equations (3.2.2)-(3.2.6). The time difference τ is expressed in radial domain θ . In the following equations, ω_R stands for the resonance frequency of the beam. And u_M is the maxima deflection amplitude of the beam.

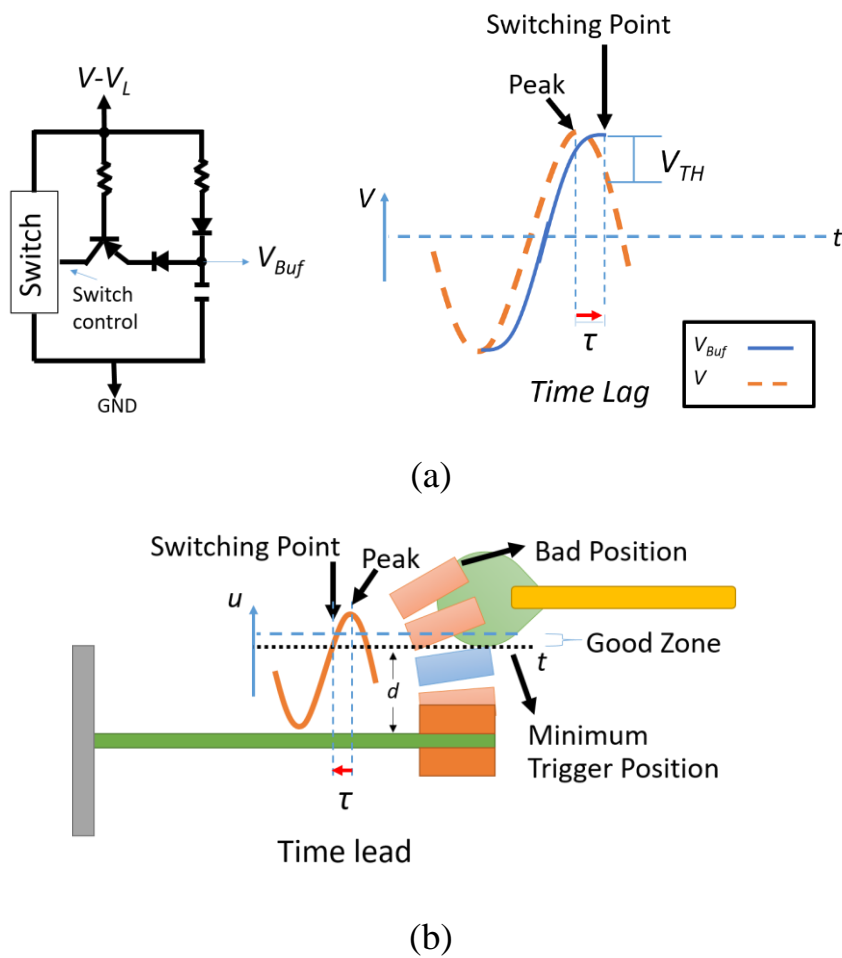


Figure 3-9 The cause of switching time difference
For (a) smart switch (b) reed switch

$$P_{para,opt} = \frac{4R_L\omega_r^2\alpha^2}{[\pi + R_L\omega_R C_0(1-\gamma)]^2} u_M^2 \quad (3.2.2)$$

$$P_{para,lag} = \frac{R_L \omega_r^2 \alpha^2 [1 + \cos \theta - \gamma(1 - \cos \theta)]^2}{[\pi + R_L \omega_R C_0 (1 - \gamma)]^2} u_M^2 \quad (3.2.3)$$

$$P_{para,lead} = \frac{4R_L \omega_r^2 \alpha^2}{[\pi + R_L \omega_R C_0 (1 - \gamma)]^2} (u_M \cos \theta)^2 \quad (3.2.4)$$

$$P_{series,opt} = \frac{4R_L \omega_r^2 \alpha^2 (1 + \gamma)^2}{[\pi(1 - \gamma) + 2R_L \omega_R C_0 (1 + \gamma)]^2} u_M^2 \quad (3.2.5)$$

$$P_{series,diff} = \frac{4R_L \omega_r^2 \alpha^2 (1 + \gamma)^2}{[\pi(1 - \gamma) + 2R_L \omega_R C_0 (1 + \gamma)]^2} (u_M \cos \theta)^2 \quad (3.2.6)$$

From the above equations, one can observe that for P-SSHI, the phase leading and lag power output can be expressed with (3.2.3) and (3.2.4). On the other hand, S-SSHI, as shown in equation (3.2.6), the phase difference, lead or lag, share the same equation. That is to say, the time difference is symmetric in S-SSHI.

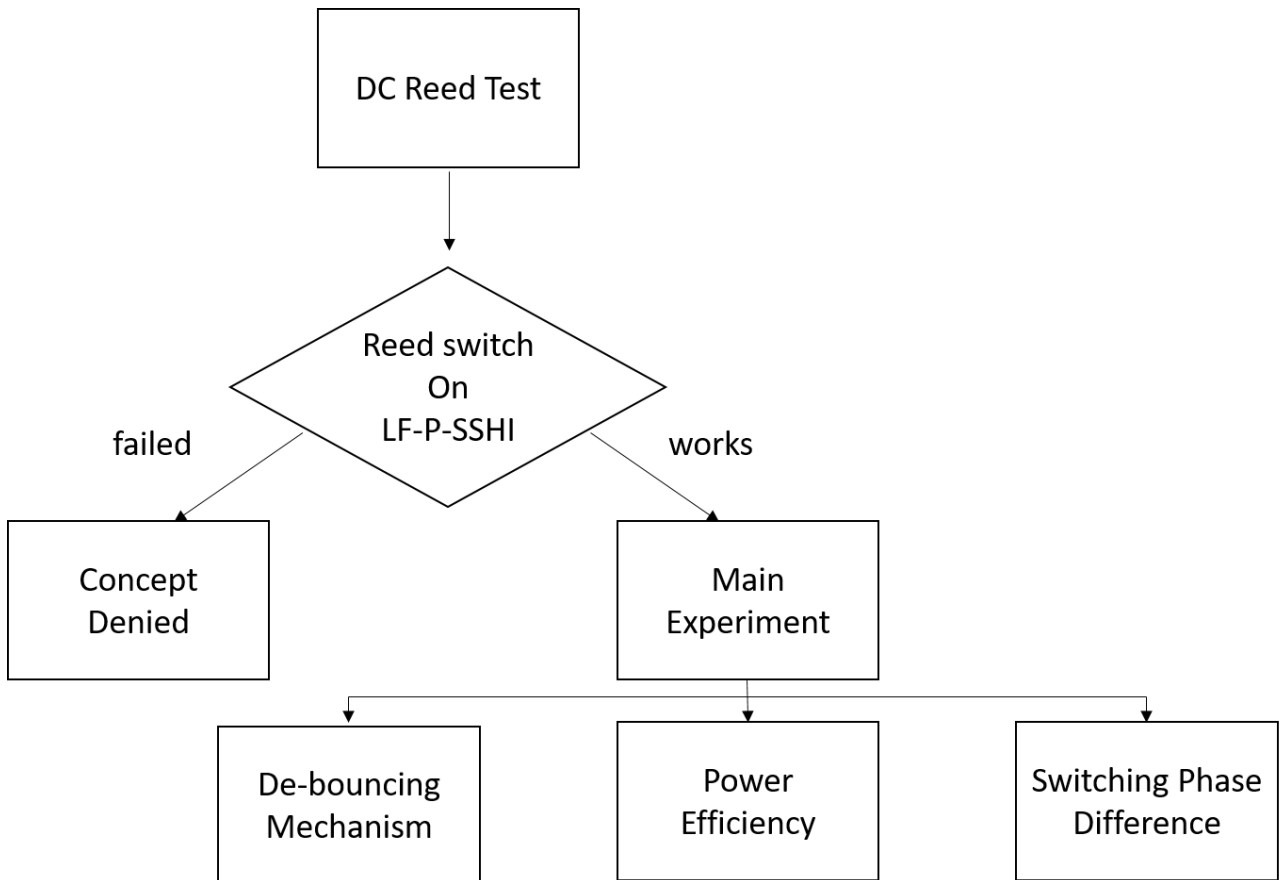


Figure 3-10 Flow chart of experiment concept

3.3 Experiment and Results

To realize the concept, the experiment was designed as shown in Figure 3-10. After the setup of the clamping device and the equipment, the DC reed test was done to assure the reed switch. It is also used to define the size of the PI zone. Then, the LF-P-SSHI circuit was conducted to assure that the reed switch is feasible for SSHIs. As it is a successful method, the de-bouncing mechanism is designed, followed by the power efficiency experiment. Lastly, the phase difference experiment was conducted.

CT-2 probes have limited sensitivity of 1 mV/mA. As mentioned, LF-P-SSHI has a higher level of current flow because it does not have any current restricting loads. Thus, it is used for observation, so that the current is high enough.

3.3.1 Experiment Setup

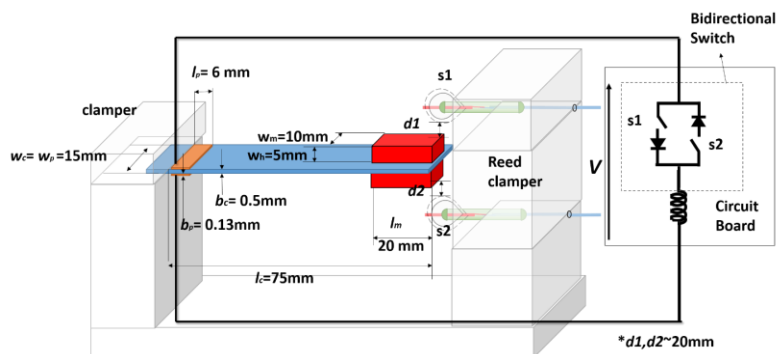
Figure 3-11 (a) shows the clamping device that holds the beam and the reed switch. The clamping system is designed with tunable x-y rails, two clamping bases on one side and one clamper on the other. On one side the cantilever beam is clamped, and the other side is for the reed switches.

The cantilever beam was composed of two piezoelectric patches bonded on both sides of the spring steel substrate. The PZT-KA2 piezoelectric patches were manufactured by Eleceram Technology Co., Ltd. The dimensions and lump parameters are listed in Table 7. Two beams were used in this experiment, beam 1 and beam 2. The beams share the same dimension, with different batch of KA-2 patches. To provide a higher voltage, the patches were connected in series. The patches are then connected to the circuit board with different circuits. The reed switches are clamped on the other side of the beam, below and above, driven by the

magnetic proof masses attached on the tip of the beam. d_1 and d_2 are the distances of maximum beam deflection to the brink of reed PI zone, which is around 20 mm (lateral distance also determined by the PI size).

The overall experiment system is shown in Figure 3-11 (b). Firstly, the output signals of the circuit are connected to the oscillator to observe the outcomes and the harvested power. The displacements were measured by two laser displacement meters. One tracked the base and the other the tip. The tip displacement can be then obtained by the difference of the tip and base displacement. To monitor the current flow and the chattering interference, Tektronix CT-2 probes were used.

The LF-P-SSHI was firstly tested for one can better observe the de-chattering characteristics from its full current flow. Then, the energy harvested from rectified SSHIs were compared. To set a reference, the externally powered SSHI was used and assumed as zero-loss. The externally powered SSHI has its driving signal provided by the second output port of the function generator, which also drives the shaker to provide the mechanical input of the energy harvester. The designed bidirectional switches were then compared: LF-P-SSHI was used to observe the current flow; P-SSHI and S-SSHI are used to investigate the efficiencies. Components used in the experiments are listed in Table 8.



(a)

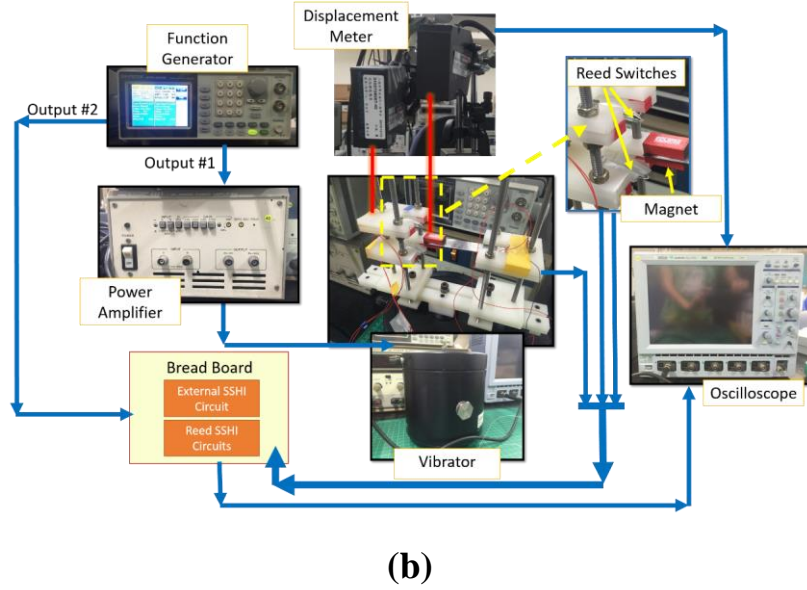


Figure 3-11 Experimental setup

(a) Schematic of the device clampers with the circuit (b) The equipment setup

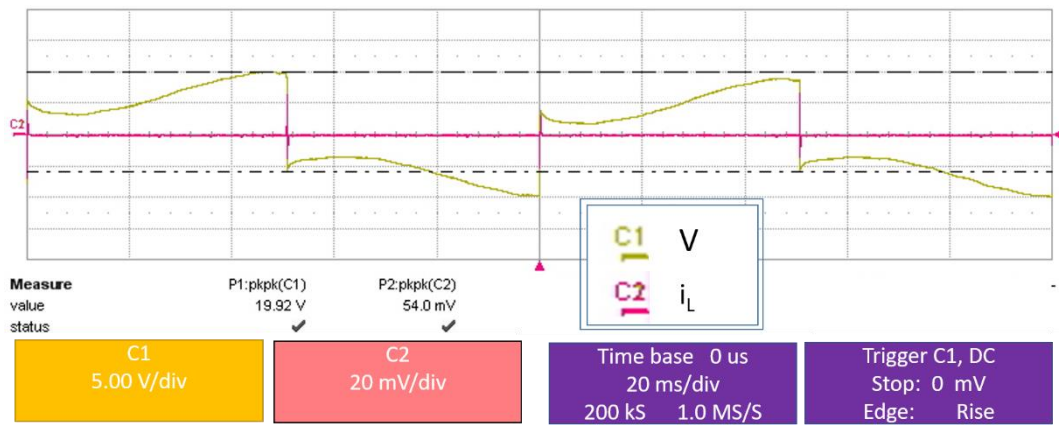
Table 7. Beam Parameters

	Description	Units
Beam Dimension	Spring Steel	
l (length)	75	Mm
w (width)	15	Mm
b (thickness)	0.5	Mm
Proof Mass ($l*w*b$)	20*10*5	Mm (per piece)
Proof Mass (mass)	12e-3	Kg
Piezoelectric	PZT-KA2	
Patch Dimension	(Eleceram Technology Co., Ltd.)	
l (length)	6	Mm
w (width)	15	Mm
b (thickness)	0.13	mm

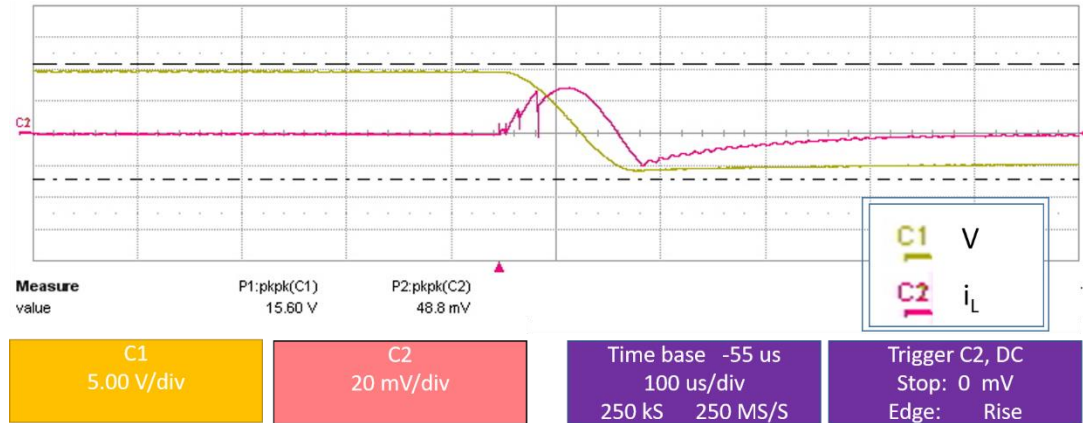
Lump Parameters	(Beam 1 + Proof mass)	
f_0	10.19	Hz
f_1	10.21	Hz
C_0	0.9e-9	F
M	25e-3	Kg
K	107	N/m
C	2.6e-2	N s/m
K_D	255.553	
K_E	254.5e	
Q_M	37.66	
k^2	0.0103	
Lump Parameters	(Beam 2 + Proof mass)	
f_0	10.496	Hz
f_1	10.512	Hz
C_0	0.86e-9	F
M	26e-3	Kg
K	80.644	N/m
C	6.183e-2	N s/m
KD	328.75	
KE	327.75	
Q_M	66.42	
k^2	0.0342	

Table 8. Component list used in the reed switch based SSH experiment

Component	Part No., Manufacturer	Component Value
Inductor	RL181S-104J-RC, Bourns	100 mH
Snubber Capacitance	N/A	68nF
Resistance	N/A	10~100k
NMOS:	2N7002, Diode Incorporated	See Datasheet
PMOS:	NDS0610, Fairchild	See Datasheet
SCR	P0130aa, STMicroelectronics	See Datasheet
Diode	BAT 54W, Infineon	See Datasheet
Reed Switch	RI-27A, Coto technology	See Datasheet



(a)



(b)

Figure 3-12 Reed switch applied on LF-P-SSHI without de-bouncing

(a) AC waveform (b) Close-up look of the LC resonance current flow on switching instance 0.03g, beam 1

3.3.2 Chatter Loss and the de-bouncers

3.3.2.1 Chatter Loss

The first experiment proved the LF-P-SSHI successful Figure 3-12 (a)), even with the chatter openings that caused the flaws on the current pulse Figure 3-12 (b). One can observe that there are two cuts in the current flow. The chattering caused the current flow to have sharp edges on the closing, and it is trivial that the interference would lower the current flow and reduce the harvested energy.

To understand the loss due to the chatter, power harvesting experiments are done. Resistors and capacitances are loaded with the rectifiers. Using both S-SSHI and P-SSHI, we investigated the chatter loss by adopting the reed switch without any snubbers.

We first look into the harvested energy of the externally powered P-SSHI and the reed switch only P-SSHI. Figure 3-13 shows the energy output performance of reed switch application without snubbing on both P-SSHI and S-SSHI. In the plot

legend, classic stands for the SEH, P-Reed is the P-SSHI using reed switch, P-External is the externally controlled P-SSHI, S-Reed is the series SSHI using reed switch. Driven on 0.07 g, The output power of the reed only P-SSHI is 41.09 μW , whilst the externally power output is 42.26 μW . The loss percentage of P-Reed is only 2.8%. For P-SSHI, One can find that the reed switch output is 42.77 μW , comparing to 46.59 μW of the externally powered. With loss percentage of 8.2%, higher than that of the P-SSHI. Both experiments show that the energy is enhanced from the SEH technique.

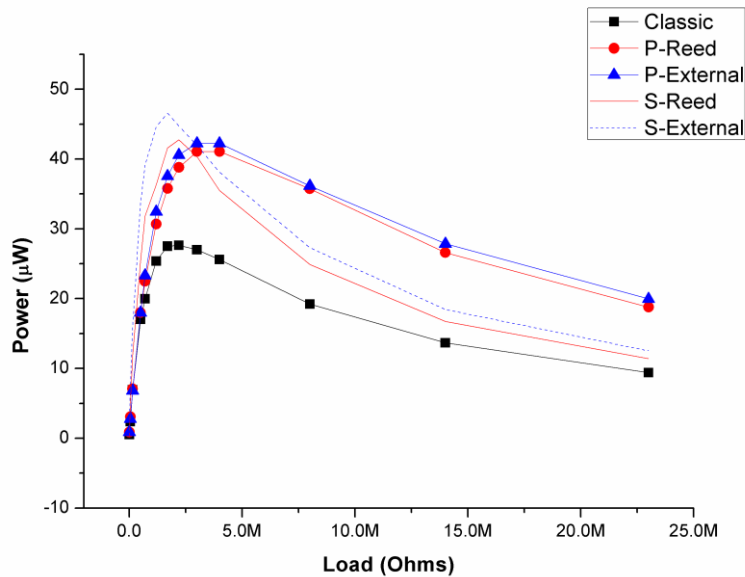
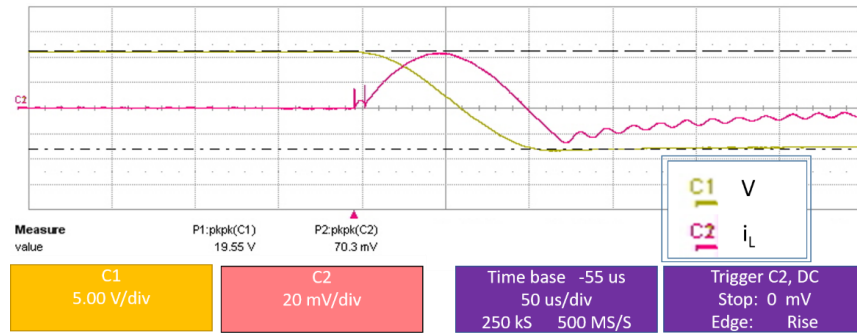


Figure 3-13 Energy loss due to switch chattering driven on 0.07 g, beam 1

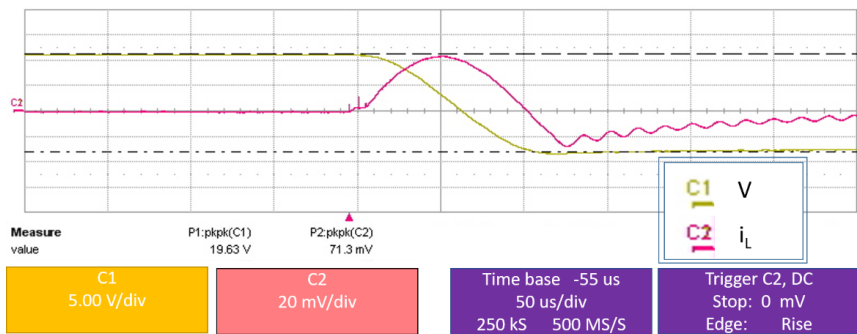
3.3.2.2 Filtering De-bouncers

Theoretically, avoiding the chattering may enable us to keep a stable current flow and achieve a better efficiency. Firstly the RC filter snubber was applied and tested as the first proposed methods. LF-P-SSHI was used to observe the current flow, as shown in Figure 3-14. Observing Figure 3-14 (a), we find a current reset on the beginning of the current flow, which is caused by the chattering. Despite the cut, the current flow was much smoother than that of the non-snubbed SSHI, shown in

Figure 3-12 (b). The peak current flow is also increased using RDR. Using RDI, the spikes are attenuated, while the current peak is slightly increased. One can also find that the reset was avoided with a small descend.



(a)



(b)

Figure 3-14 Current flow of filter snubbed LF-P-SSHI on switching

(a) RDR (b) RDI 0.03g, beam 1

However, when the load is added, the resistor on the snubber may share the energy that the piezoelectric element produces. Accordingly, the RDI was proposed as a replacement of RDR. The experiment for the harvesting efficiency is performed for the purpose of proving this thought. Both P-SSHI and S-SSHI were used in this experiment, which is shown as Figure 3-15 (a) and (b).

In spite of the successful snubbing, the RDR showed a lower power output comparing to the non-snubbed experiment. Results also show that the RDI had almost perfect performance, and the output curve overlaps with that of the externally

powered one on P-SSHI. For S-SSHI, the performance of the RDR is also poor. Taking account of the RDI, the optimal harvested energy is $44.52 \mu\text{W}$. The externally powered S-SSHI, the best output is $46.59 \mu\text{W}$. The loss of the RDI in SSHI is 4.44%, which is better than the non-snubbed version. However, the harvested energy quickly falls after the optimal load, and the output waveform also shows an unstable status, as shown in Figure 3-16.

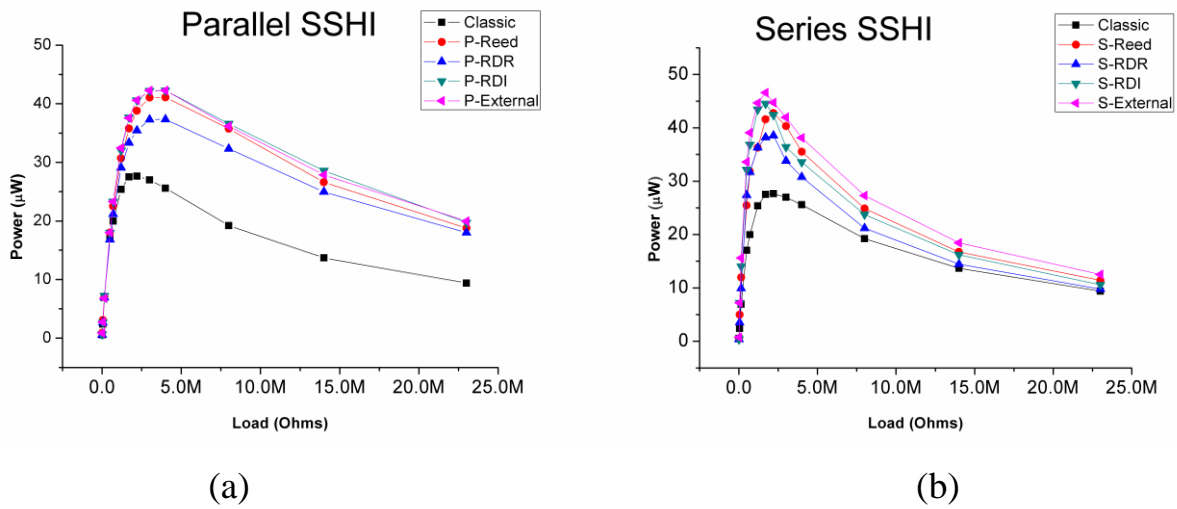


Figure 3-15 Power output experiments for filtered de-bouncers

(a) P-SSHI (b) S-SSHI, driven at 0.07g, beam 1

Plot Legend format: Prefix-Method (e.g. S-Reed)

Prefix: P (parallel) ; S (series)

Method: SEH (Classic); reed switch without snubber (Reed); Reed de-bounced on resistor (RDR);

Reed de-bounced on inductor (RDI); Externally powered switch (External)

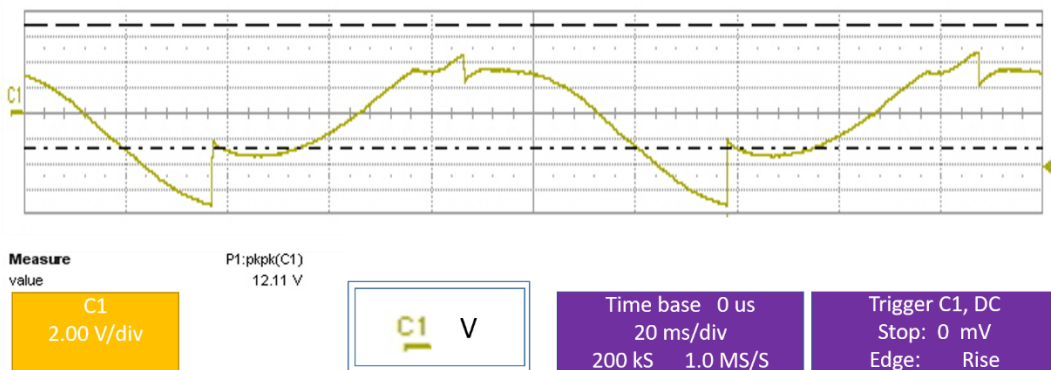


Figure 3-16 Piezo voltage output when high impedance is loaded at the RDI S-SSHI on $3M\Omega$, 0.07g, beam 1

3.3.2.3 SCR De-bouncer

SCR was then designed as another solution to prevent the unstable status in high impedance loads. Despite the lowered current peak, the SCR de-bouncer also showed a small ebb on the switch bounce, it is not as obvious as the fall on RDI in Figure 3-14 (b). One can also observe that the current kept at positive slope.

Experiment results in Figure 3-18 showed that the SCR overcame the high impedance loading problem of RDI on S-SSHI. Under 0.03g, the SCR output almost overlapped with the externally powered output. The experiment was done 3 times for the error bar.

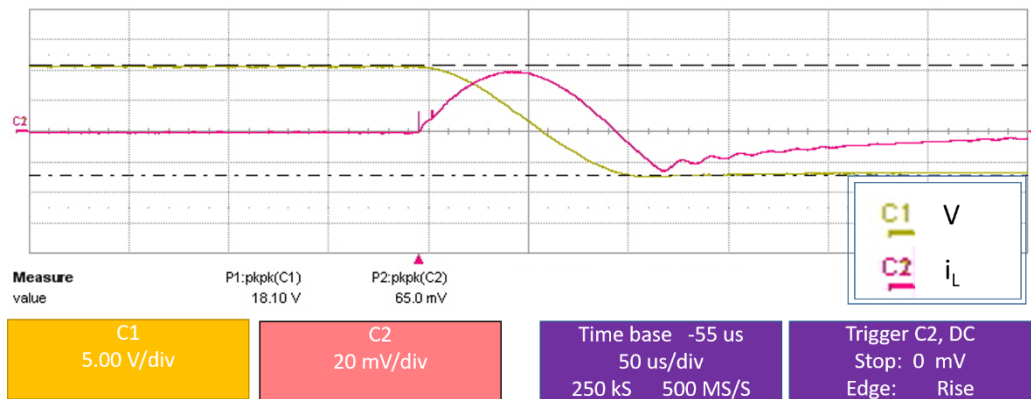


Figure 3-17 Current flow of SCR snubbed LF-P-SSHI on switching, 0.03g beam 1

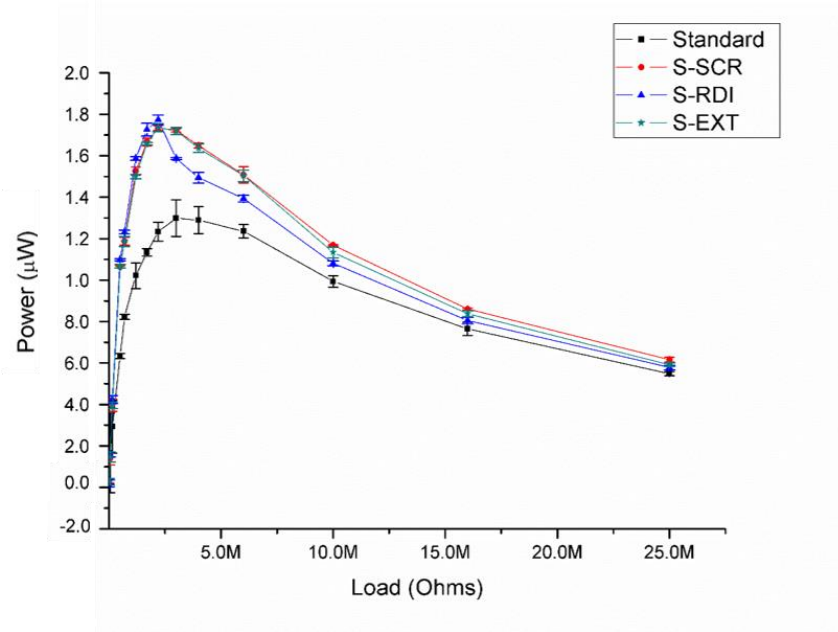


Figure 3-18 Output of SCR de-bounced comparing to other circuits
SEH, S-RDI, S-EXT on 0.03g, beam 2

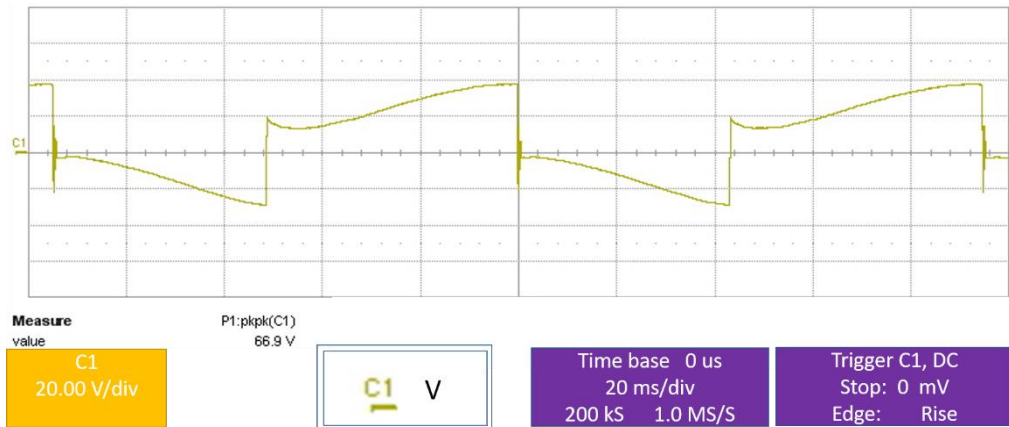


Figure 3-19 SCR malfunctioning waveform with overdriven voltage.
0.06 g, beam 2

Nonetheless, SCRs are current controlled components. Moreover, the SCR P0130AA we chose for this work was designed for low power, and therefore cannot withstand high inverse voltages. Thence, when the beam is driven with higher voltage output, the SCR breaks down and the SCR fails to stop the inversing current. Figure 3-19 shows that the LC resonance cannot be halted as what we desired when

driven in higher voltage inputs.

3.3.3 Loss due to switch delay

An experiment using externally powered switch was conducted to investigate the effect of switching phase difference. The theoretical curve equation can be derived from [88]. From which, the gain χ_{para} and χ_{series} for the affected output can be further expressed as the equations:

$$\chi_{para} = \begin{cases} \frac{P_{para,lead}}{P_{para,opt}} = \cos^2 \theta \\ \frac{P_{para,lag}}{P_{para,opt}} = \frac{[1 + \cos \theta - \gamma(1 - \cos \theta)]^2}{4} \end{cases} \quad (3.3.1)$$

$$\chi_{series} = \frac{P_{series,diff}}{P_{series,opt}} = \cos^2 \theta \quad (3.3.2)$$

Figure 3-20 shows the theoretical and experimental relationship between the phase difference and the normalized gain of the P-SSHI and S-SSHI. The plot is plotted from gain equations (3.3.1) and (3.3.2). From (3.3.1), one can understand that the lead and lag does not have a symmetric effect when applying P-SSHI. For S-SSHI, how the phase difference affect is symmetric. However, for the sake of reed switches, only phase lead is required to be considered.

Results shows that for P-SSHI, experimental results match that of the theoretical simulation. On the other hand, S-SSHI has a greater loss, which may also be attributed to the component loss, which showed to be higher in S-SSHIs as mentioned.

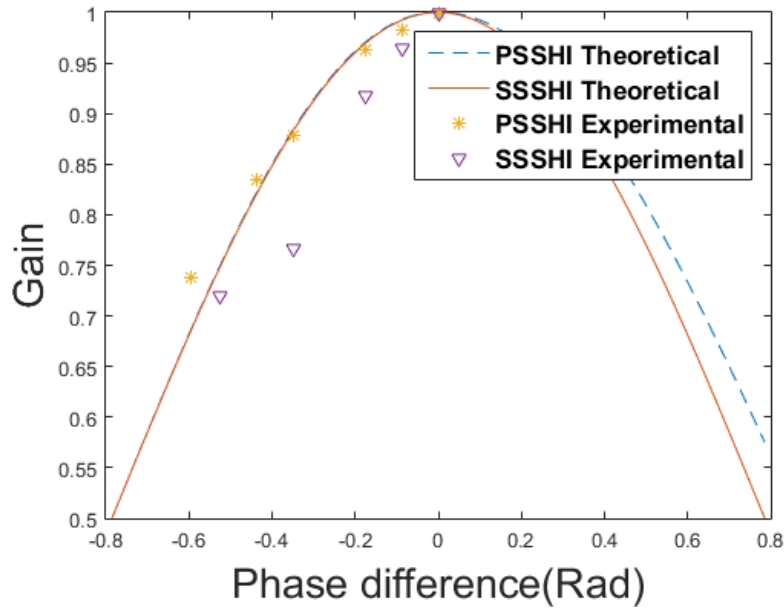
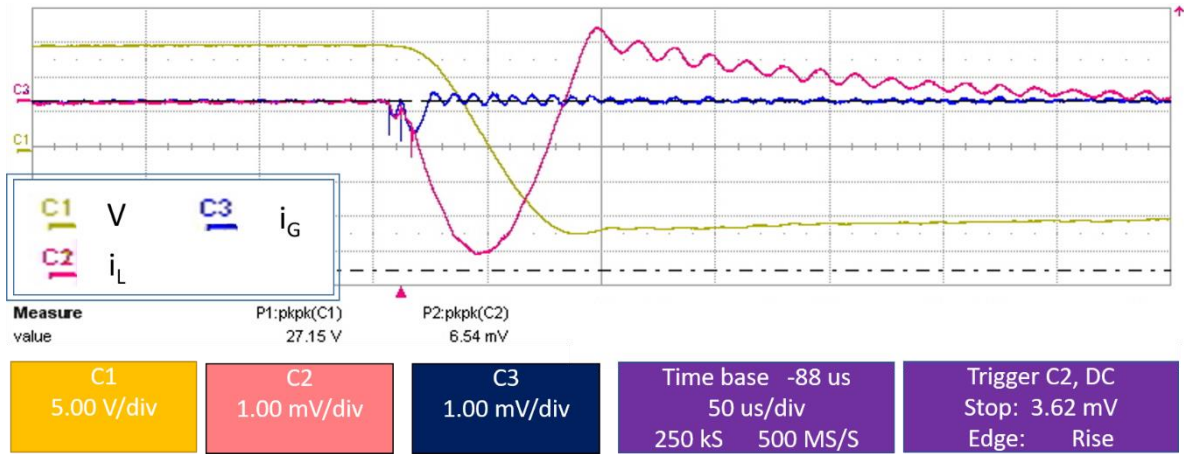


Figure 3-20 Phase difference relations to P-SSHI and S-SSHI gains.
Externally powered switches used.

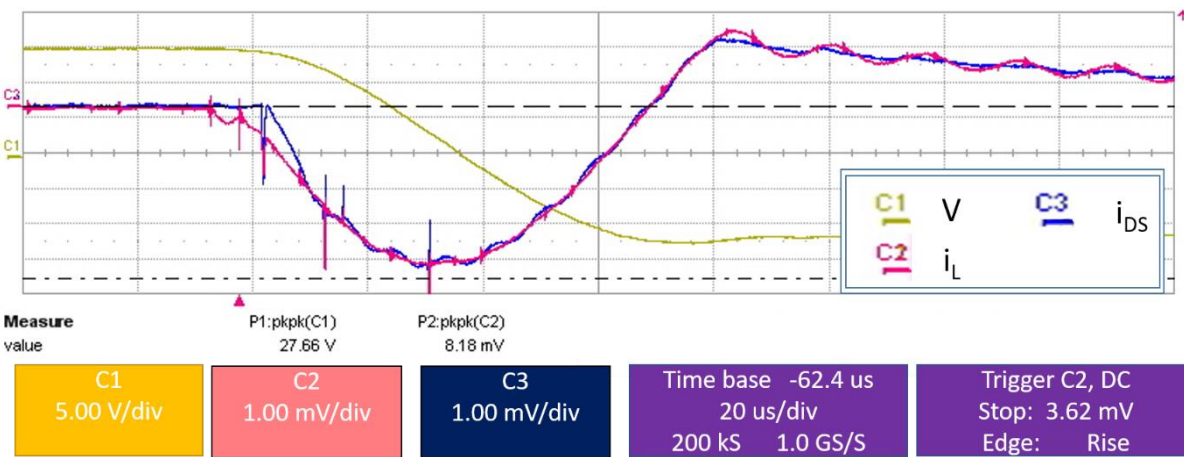
3.3.4 Working Mechanisms of De-bouncers

3.3.4.1 Snubbed Switches Working Mechanism

RC and LC de-bouncers are filters, and the configuration is similar, and so as their working mechanism of de-bouncing. LF-P-SSHI was used to observe the current flow, so that we can understand how the mechanism works. The current flowing through the gate and the terminals DS were tracked using Tektronix CT-2 probes, so as to understand the working mechanism of the configurations. Figure 3-21(a) shows the experiment results indicating that the MOSFET, will draw a small portion of the current initially (C3 of Figure 3-21 (a)), from the RDI capacitor to start the overall conduction, where I_{DS} is conducted (Figure 3-21 (b)). The total component loss can be calculated from the $i_G * R_G$ and $V_{DS}^2 * R_{DS} + V_{TH} R_{ON}$.



(a)



(b)

Figure 3-21 Voltage and current tracking of LF-P-SSHI using RDI

(a) C1 the voltage, C2 the total current, C3 the current into the gate of the MOSFET (b) C1 the voltage, C2 the total current, C3 the current through terminals DS of the MOSFET

4.3.4.2 SCR Working Mechanism

To investigate the SCR working mechanism, the current flowing into the SCR terminals G (I_G) and A (I_{AK}) were tracked. The two routes composed the total current, while the current flowing into the terminal G was fluctuating due to the chattering. The current was compensated by the route AK, which in summation created a smooth current which we aimed for. This implies that the component loss for the

SCR is mostly caused by the inner resistances of the SCR.

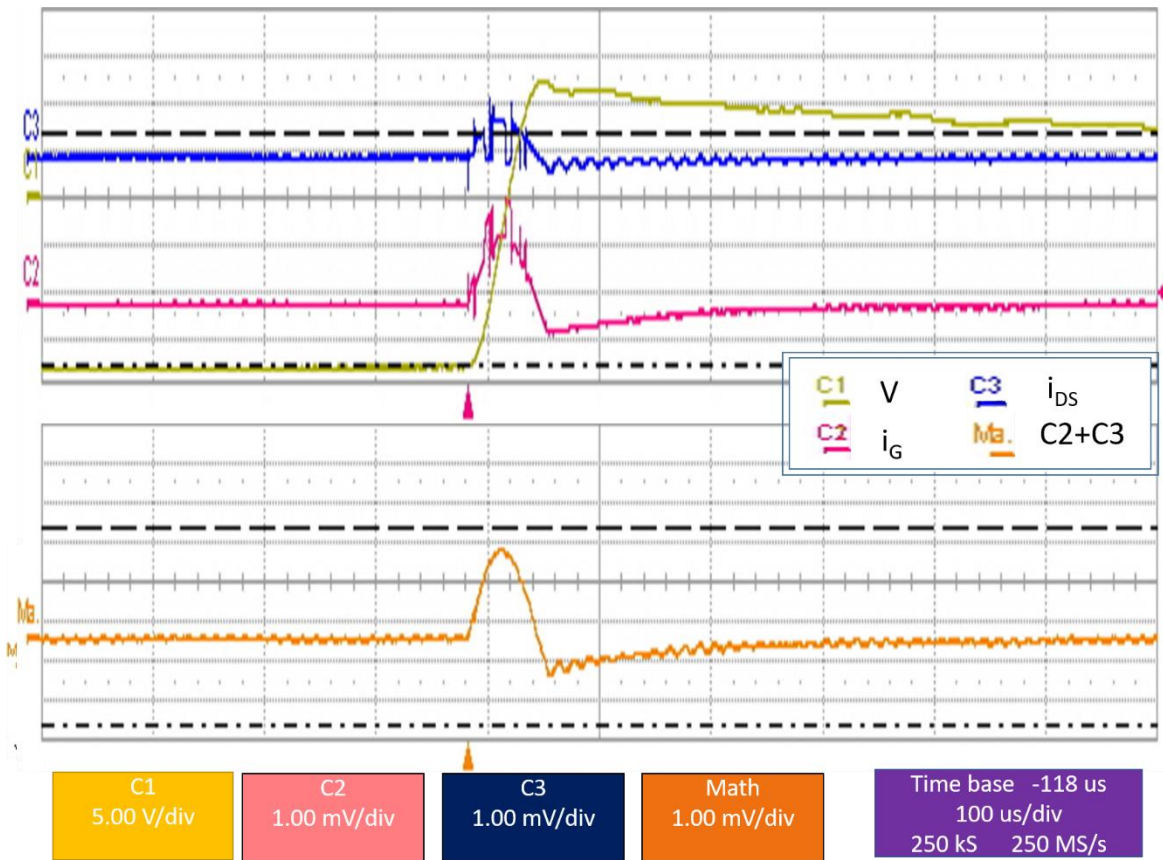


Figure 3-22 Voltage and current tracking of LF-P-SSHI using SCR

C1 is the voltage, C2 the current into the anode of the SCR, C3 the current into the gate terminal of the SCR, Ma the summation of C2 and C3, which sums up to be the overall passing current.

3.3.5 Low voltage driven S-SSHI

RDI was used for a low voltage test. Result is shown in the following Figure 3-23. Results showed that the S-SSHI was still working, while P-SSHI did not show a clear enhancement.

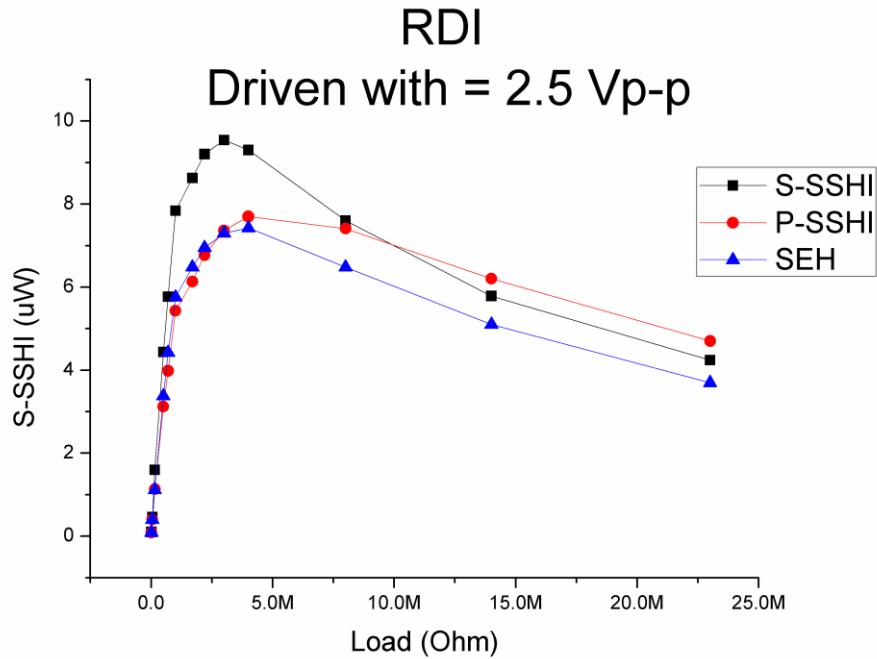


Figure 3-23 A low voltage driven experiment using RDI using piezoelectric voltage output was 2.5 V_{p-p}

3.4 Discussion

3.4.1 Chatter Loss on P-SSHI and S-SSHI

From the experiment results of Figure 3-13, the power loss from the reed-diode configuration in P-SSHI is around 1.17 μW , and its corresponding loss percentage is 2.8%, comparing to the power harvested from externally powered switching technique, which is 42.26 μW . The loss percentage can be briefly attributed to the chatter since both configurations have identical diodes to stop the reversing LC resonance. For S-SSHI on the other hand, the loss is 3.82 μW , in the total of 46.59 μW . Corresponding loss percentage is 8.2%, higher than that of the P-SSHI.

From the circuit configuration of P-SSHI and S-SSHI, we are able to understand that, when the switch is off, the current still flows through the rest of the circuit, identical to that of a SEH. However, for S-SSHI, when the circuit is off, the load is

not connected, and all the energy is saved in the inductor. When the switch launches, the circuit flow of P-SSHI is less than S-SSHI, and therefore, the loss due to the DCR of S-SSHI is much higher than P-SSHI.

3.4.2 Comparisons of the proposed switching methods

Experimentally, the three well performing designs are the reed-diode, SCR and RDI. Each of the designs has its own merit: With very limited voltage (i.e. lower than 2~3 volts) and low harvested power, the reed-diode configuration provides the best efficiencies due to its simplest components. When energy harvested is not enough, SCRs and RDIs do not perform ideally due to the characteristics of the electrically triggered switches. However, when enough power is supplied, both SCR and RDI work with efficiency that may reach 99% or more in P-SSHI and also performing with little loss in S-SSHI. When ultra low voltage is supplied, the SCR outperformed RDI in moderate power conditions because the MOSFET is voltage controlled. Moreover, when S-SSHI is operated in high voltage, the SCR meets its reverse breakdown and the mechanism is not favorable. On the other side, with high impedance loaded, the RDI is not able to collect enough energy to launch and the switching becomes unstable:

One can observe from Figure 3-18, we find that the SCR showed better stability when higher impedances are loaded, whilst the RDI show a drop in output right after the optimal impedance. However, it was also discovered in Figure 3-19 that when operated in high voltage input and low impedances on series SSHI, SCRs showed unwanted conduction due to the break down. One can attribute the malfunctioning to the V_{RG} of the SCR, that is, the maximum reverse voltage then can be applied across gate and cathode terminals without risk of destructing the PN junction GK. For P0130AA, V_{RG} is merely 8 V minimum, with the reversed gate current of 10 μ A.

In spite of the increased V_{RG} in the low operating current of piezoelectric energy harvesting circumstances, SCRs are still not feasible with high voltage applications.

Table 9 was created to give an idea of which configuration to choose under different operating situations.

Table 9. Performance of proposed methods under varying operating circumstances

Operating Situations	Reed-Diode	SCR-P0130AA	RDI-2N7002T1
Limited Voltage / Current	☺	☹	☹
Moderate Conditions	☹	☺	☺
High Voltage	☹	☹	☺
High Current*	☹	☺☺	☺☺

*Piezoelectric components do not provide high current flow continuously. High current flow is usually caused by the LC resonance on switching, usually on series SSHI with low impedance or SSHI without loads.

One should note that, when applying the hybrid-switch harvesting system to random force vibrations, where the displacement may not reach the PI zone, the switch cannot be turned on. In this situation, the S-SSHI is not activated and thereby no power can be harvested due to the energy block of the switch. Thus, P-SSHI can be applied despite the lower harvested power. As the switches are not working, SEH is still connected in P-SSHI, and the harvesting is still on. When the tip displacement

is large enough for trigger, P-SSHI will be launched, which will provide a better harvesting efficiency.

3.4.3 Designing the hybrid switched SSH system

The following text would give a discription design procedures for one who wishes to design a synchronized switching system using reed swtiches.

Before designing, one should consider the working circumstance: is it a steady condition? Or a flucuatating condition? With constant force and displacement, both P-SSHI and S-SSHI can be applied. However, when the system is operating under fluctuated condition and the deflection varies, P-SSHI is recommended. Although S-SSHI is able to provide a better power enhancement, P-SSHI is stable - even when the switch is not working, SEH is still on the line. When the system is well designed, one can even decide the triggering voltage of the P-SSHI. As the voltage does not reach the desired level, the SEH would continuously work.

For ultra low voltage applications such as open voltages of around 2~3 Vpp, it was observed that while the supplied voltage is lower than the fully switching threshold, the MOSFETs or SCRs used in filter snubbers cannot work in its linear state. This would result in a more severe component loss, and lower the inversion factor γ . In this occasion, SEH may provide a better efficiency comparing to the switching technique. Therefore, by targeting the input force, designing the beam and the distance between the reed switch and the tip, one can determine a targeting voltage for the switch to be triggerd. Another choice would be to apply the reed-diode pair method, to avoid excessive component losses.

To design the overall system, the operating frequency is firstly targeted according to the applying environment. With the operating frequency, the resonance of the device can be used to determine the beam dimension, and the proofmass used. To

apply the reed switches, the cantilever beam substrate should be able to withstand deformations at least exceeding the distance between the PI and the DO zone of the reed switch. Then, according to the substrate scale, a brief estimation of the beam dimension can be determined. Thereafter, the reed switches and magnet pairs can be decided. For instance, micro-sized or bulk sized, glass sealed or overmolded. For micro-sized cantilever beams such as [90-94], SMD packages are available. However, the operating power range should be considered, so that the break down voltage and current of the components should not be met. The determination of the operating magnet can be done by referencing the closing force in newtons (N) for the reed switch, usually provided in the datasheet. Some datasheet provides operating ranges in units of Tesla (T). Also it is worth noting that some magnets are designed for reed switching as a pair. When the beam substrate and the magnet, serving meanwhile as a proofmass, is chosen, the main beam dimension and thus the actual operating frequency can then be precisely designed, considering the operating force and the responding tip deflection. With the knowledge of the tip deflection, we are able to determine favorable switching ranges, including the optimal switching distance and also the available phase difference margin.

Afterwards, the switching distance are to be determined by the magnet-reed switch pair, depending on the shape and size of the PI zone, which is dominated by together the sensitivity of the reed switch and the magnetic field strength. For switches with overlapping PI zones, overlapping areas should be averted so as to prevent from false signals. Another important point of consideration is the hysteresis time, or the distance between the PI and DO zone. To be conservative, the on switching period should not reach or exceed 50% of the duty cycle so that the switches would not conduct simultaneously. This means that the DO zone should not cover all the range of the tip displacement when operating in small displacements, or

short circuit would be caused. Considering the time lead effect, we can calculate the theoretical optimal power output, with constant driving force, and further derive corresponding the deflection by referencing [71]. Considering the acceptable loss, the phase lead can be determined. By converting the phase θ to the distance d , the equations below can be obtained to design the reed location:

$$P_{u,para,reed} = \begin{cases} \frac{R_L \omega_R \alpha^2 [u_M + d - \gamma(u_M - d)]^2}{[\pi + R_L \omega_R C_0 (1 - \gamma)]^2}, u_M \geq d \\ P_{u,SEH,u_M}, u_M < d \end{cases} \quad (3.4.1)$$

$$P_{u,series,reed} = \begin{cases} \frac{4R_L \omega_R^2 \alpha^2 (1 + \gamma)^2}{[\pi(1 - \gamma) + 2R_L \omega_R C_0 (1 + \gamma)]^2} d^2, u_M \geq d \\ 0, u_M < d \end{cases} \quad (3.4.2)$$

Lastly, the operating conditions as mentioned in the Table 9 can then help to decide which hybrid switch method can be used.

3.4.4 Comparison to the original smart switch considering the phase difference

The reed switch provides a leading phase difference, considered as the negative switch delay in [88]. On the other hand, the smart switch results in a phase lag caused by the threshold voltage of the comparator. The phase lead of the reed switch can be determined by the location of the pull in zone. As represented as eq. (3.2.1). The electrical phase lag can be calculated using eq. (2.2.5), which yields:

$$1 - \frac{(V_{EB} + V_D)}{V_{PZT}} = \cos(\theta) \quad (3.4.3)$$

To at least achieve identical harvested power comparing to the smart switch, the simplified equations in eq. (3.3.1)-(3.3.2) can be used to obtain the electrical loss due to the switching delay of the smart switch. According to eq. (3.3.2), the harvested power of the reed switch is identical to that of the smart switch when the phase differences are identical. Therefore, we can obtain for symmetrical results.

$$1 - \frac{(V_{EB} + V_D)}{V_{PZT}} = \frac{d}{u_M} \quad (3.4.4)$$

By this equation, one can obtain the targeted distance between the PI zone and the tip of the base with reference to a smart switch. Where d is the targeted PI zone distance.

For P-SSHI, the harvested power of the reed switch can be found identical to that of the SEH with different quantity of phase lag:

$$\cos^2 \theta_{Lead} = \frac{[1 + \cos \theta_{Lag} - \gamma(1 - \cos \theta_{Lag})]^2}{4} \quad (3.4.5)$$

Where, taking eq. (3.4.3) in to account, one can obtain θ_{Lag} , the lagging phase difference caused by the comparator threshold. And therefore d , the distance between the zero displacement of the tip and the PI zone can be determined using the equation from eq. (3.2.1) after the calculation of θ_{Lead} :

$$d = \frac{[1 + \cos \theta_{Lag} - \gamma(1 - \cos \theta_{Lag})]}{2} u_M \quad (3.4.6)$$

By then we can determine also the location of the PI zone for P-SSHI, referencing to the optimal harvested power of the smart switch, neglecting the PN junction losses.

Chapter 4. Magnetically Connected Array

This section introduces the magnetically connected array as a solution to increase the working bandwidth of the piezoelectric energy harvesting systems. Different from the conventional electrical connecting or the physically binding methods, mechanical force of magnetic repulsive force is used. By this mean, the three beams are mechanically connected, with no physical contacts with each other. The proposed method also creates a new type of MDOF structure. Comparing to the commonly seen MDOF structures where a major structure carries several small structures, the proposed method provides the possibility of multiple systems with similar sized cantilever beams. This structure is also similar to stoppers, which is also used for bandwidth expansion.

In this chapter, the design concept is firstly described. Then, the theoretical model and simulation of the interfered results between the beams are proposed. Experiment results are then presented.

4.1 Design concepts

The initial intension was to provide a non-contact stopper by using magnets to expand the bandwidth. However, magnets do not create nonlinear step changes as conventional stoppers, the major beam interferes with the other beams. When the side beams are on resonance, the displacement of the side beams would also strike the middle beam. In consequence, the resonance of each beam would affect the other and cause a new peak output.

To investigate, simulation on only the interaction between two beams are firstly performed. The two-beam configuration is shown in Figure 4-1(a). Then, another

side beam was added into the simulation, physical configuration shown in Figure 4-1(b). By designing the distance between the multiple beams and also the resonance of the beams. The beam in the middle would give outputs with three peaks, in consequence of the other two vibrating beams. Moreover, if the peaks are close together, the bandwidth should be expanded.

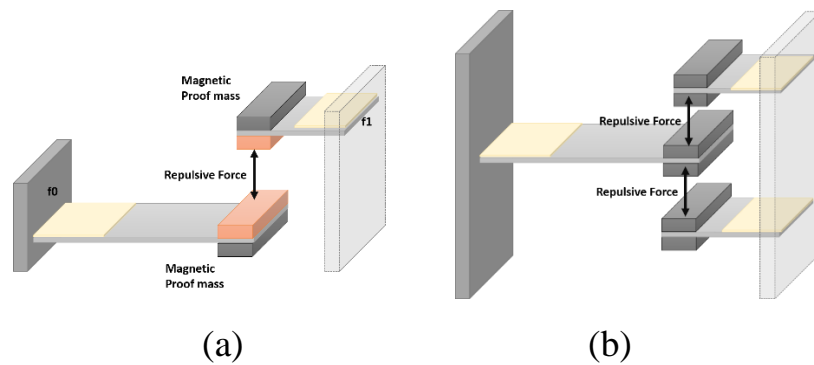


Figure 4-1 Design concept of the magnetically connected beams
(a) two beams, (b) three beams

4.2 Theoretical Assumption and Simulation

For further experiments and simulation parameter references, simple cantilever beams patched with piezoelectric materials were made. The beam substrate is based on spring-steel, with two different aspect ratios. The tips are loaded with magnetic proof-masses on both sides. Beam parameters are listed in Table 10. The lump parameters are experimentally measured and listed in Table 11. The magnet used and its parameters are listed in Table 12.

Table 10. Geometric parameters of the applied beams.

	Main Beam	Side Beams
Length (mm)	77	46
Width (mm)	15	15
Thickness (mm)	0.3	0.3

Mass w/ proof mass (mg)	3.7	23.6 (Upper) 23 (lower)
-------------------------	-----	----------------------------

Table 11. Parameters of the beams applied in experiment and simulation.

	Middle Beam	Side Beams	Units
f_0	18.64	13.02	Hz
f_1	18.69	13.05	Hz
C_0	4.5e-8	9e-9	F
M	4.10e-3	2.36e-2	Kg
K	54.59	158.80	N/m
η	6.74e-3	2.62e-2	N s/m
K_D	187.15	217.75	
K_E	186.15	216.75	
Q_M	71.55	34.13	

Table 12. Parameters of Magnets used in the experiment and simulation.

	Magnet Factors	Units
Br	0.83	T
Am	25	mm ²
L	6	mm
R	5	mm
μ_0	1.256e-6	H m ⁻¹

4.2.1 Interaction between 2 Beams

To set up the simulation, the beams are firstly modeled in to MCK models. Then the repulsive connecting forces, as show in Figure 4-1, has to be modeled. Referencing [55], the repulsive force between the two MCK systems can be represented as an additional non-linear spring with coefficient k_{12} for inserted between the systems 1 and 2, as shown in Figure 4-2 (a). The schematic of the beam movement behavior is as Figure 4-2 (b). The magnetic force can be derived from (1.3.3), whilst the spring formula k_{12} can be obtained from (1.3.4). The diagram shows the MCK model for magnetic force interaction between beam 1 and beam 2 in corresponding to the tip displacements x_1 , x_2 and the distance D_{12} , which represents the vertical distance between the two cantilever beams. The distance d_{12} , which

decides the force, is the summation of x_1 , x_2 , and D_{12} .

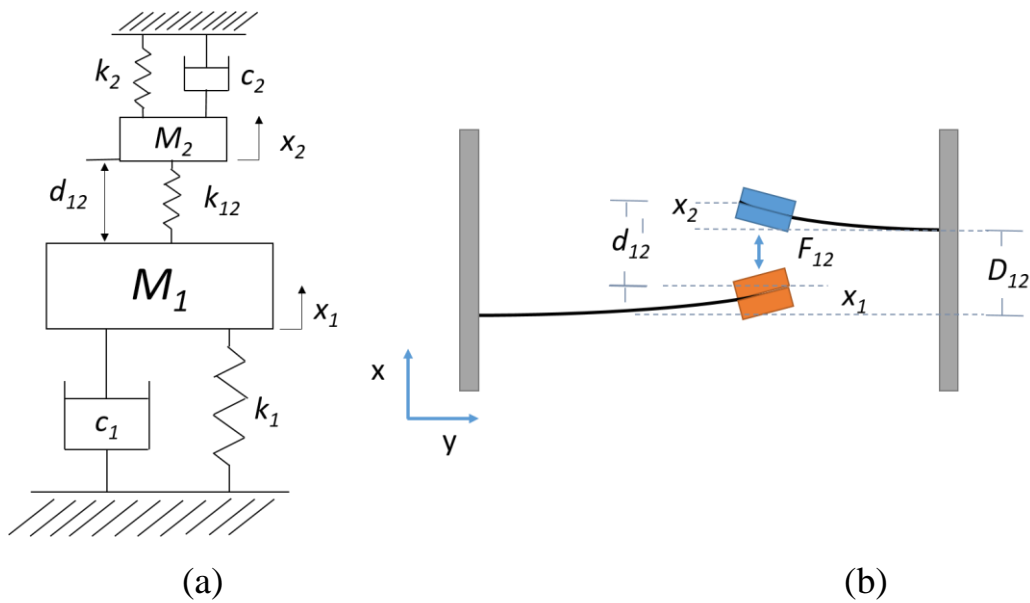


Figure 4-2 Magnetic interaction between two beams

(a) Modeling by two MCK systems connected with a spring (b) Schematic diagram

The interaction between the systems is first plotted into a block diagram in Figure 4-3 (a). This block diagram is then implemented in Power Sim[®] (PSIM), component plot as shown in Figure 4-3 (b). To make the simulation easier, the interacting force F_{12} is considered instead of the spring coefficient. Afterwards, Matlab[®] was used to do the sweep simulation of frequency and varying D_{12} is executed to observe the responding tip voltage output.

Unlike the simple step change for the spring constant in stoppers, when two magnets draw near, e.g. on the resonance of one beam, the force in between increases rapidly with the change of d_{12} . The variation trend of the coefficient k_{12} was firstly investigated, to compare with that of the simple step change. Figure 4-4 shows the simulation results of the k_{12} when constant force is given, and the vibrating frequency is set at the resonance of beam 1, and off the resonance of beam 2. Where the two beams are set 1 cm apart. One can observe the force curve which has a rapid

gradient that we can nearly assume as a pulse force as the beams draw near, e.g. on the maximum tip displacement. Therefore, the other beam which is not resonating would be forced to deform due to these pulsing forces.

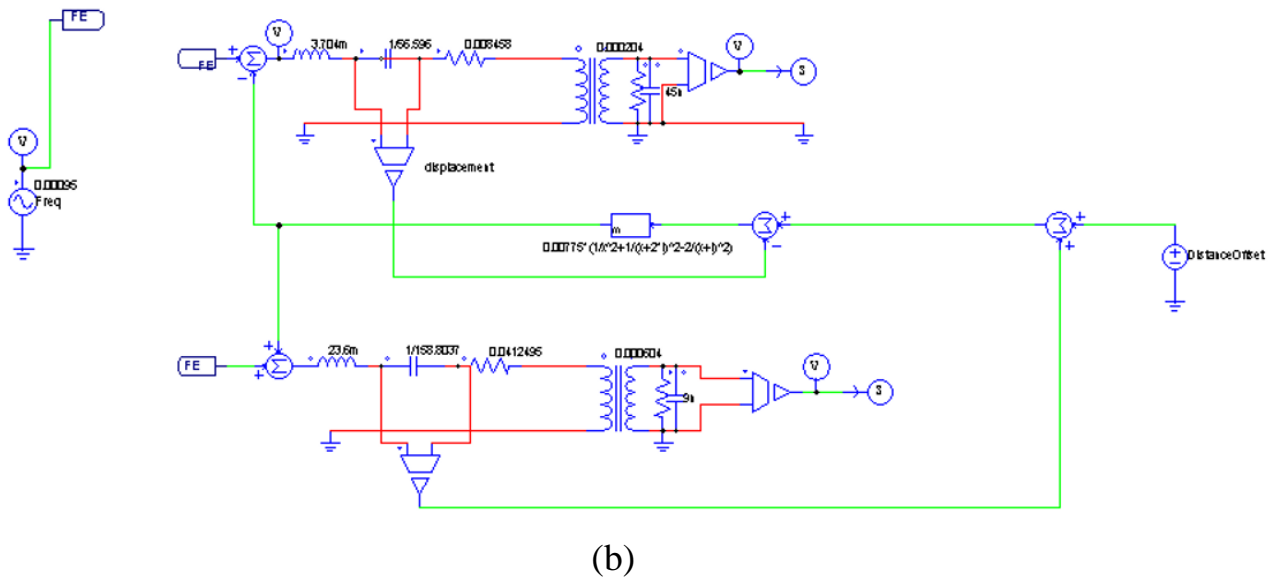
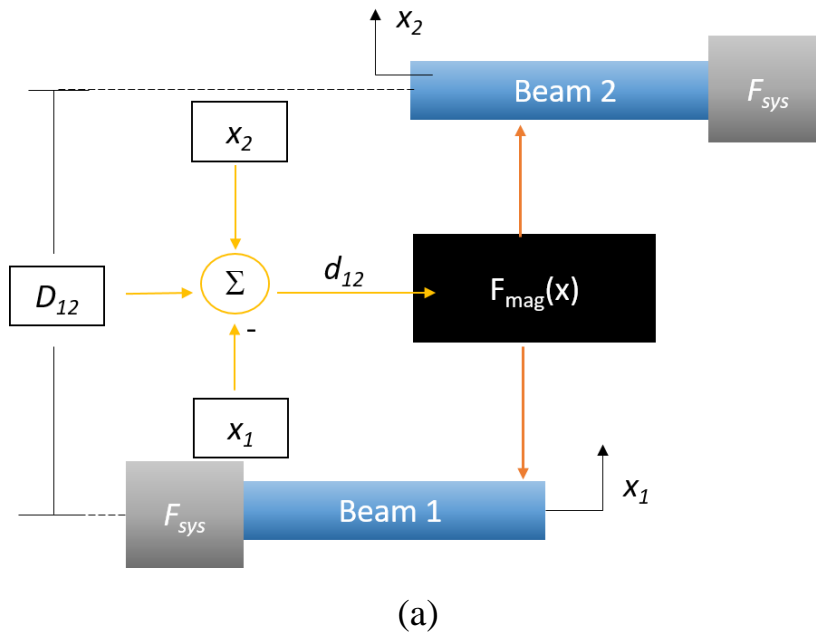


Figure 4-3 Implementation of the MCK model for simulation

(a) block diagram (b) PSIM model

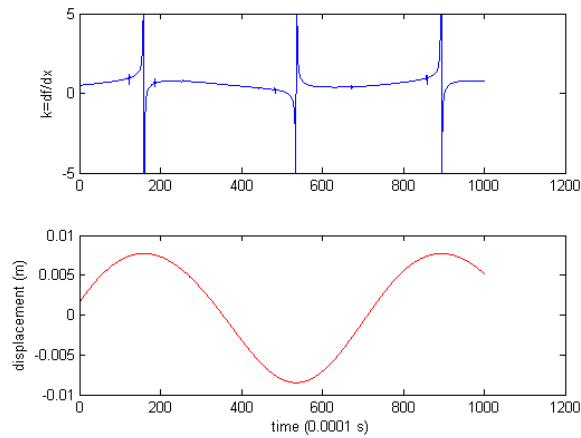
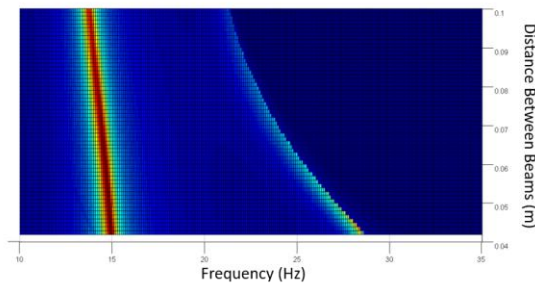


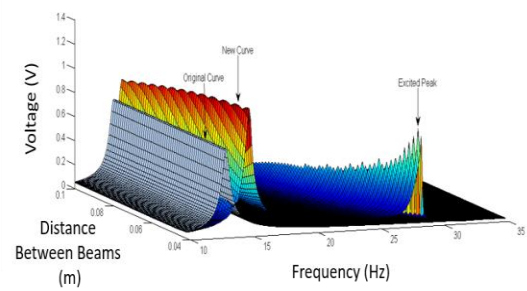
Figure 4-4 Simulation of the magnetic spring coefficient between beam 1 and 2, k_{12} corresponding to the changing distances between the magnets d_{12} . Displacement on the lower refers to u_1 , on resonance of beam 1

The 3D plot outcome shows the shift of the resonating frequency of beam 1 (lower frequency) gets higher as the distance between the beams comes close. Observing the excited peak influenced by beam 2, when the distance between the two beams decreases, both the voltage intensity and the peaking frequency increases. It can be more clearly observed in Figure 4-5 (b), where we can see that the original curve is lower than that of the influenced one, and the only peaking voltage is on the resonance unchanged.

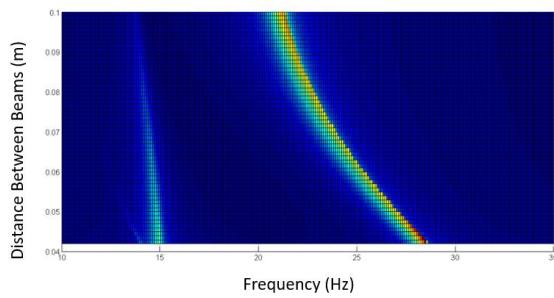
Beam 2, with a higher resonating frequency, its response is plotted in Figure 4-5 (c) and (d). The natural frequency lies between the excited peak and the newly induced resonance. Dimensions and parameters of the beam are given in Table 10 and Table 11.



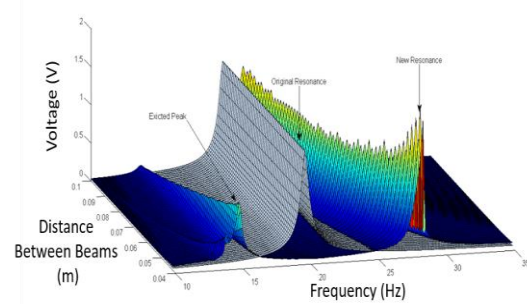
(a)



(b)



(c)



(d)

Figure 4-5 Simulation results of the 2 beam interaction

(a) beam 2, frequency shift on voltage intensity (b) beam 1, 3D plot of the voltage output responding to the frequency- D_{12} sweep. The natural frequency response of the beam represented by grey colored regions. (c) beam 2, frequency shift on voltage intensity (d) beam 2, 3D plot of the voltage output responding to the frequency- D_{12} sweep. The natural frequency response of the beam represented by grey colored regions.

4.2.2 Interaction between 3 Beams

With three beams, symmetric alignment and asymmetric alignment can be discussed. When aligned in symmetric configuration, we mean that the side beams below and above are identical in all dimensions including its shape, size, and also the distance between the middle beam. Ideally, the response is expected to be similar to that of the two beams, but with a doubled k coefficient. Two voltage peaking

frequencies are expected. If three voltage peaking frequencies are desired, asymmetric design can be considered: the side beams should be set in different distances to the main beam. To reduce complexity, identical beam parameters are used for the two side beams.

Similarly, the three-beam configuration is as shown in Figure 4-6 (b). The MCK models of the three beams is plotted in Figure 4-6 (a). Figure 4-6 (c) shows the block diagram for setting up the PSIM – Matlab simulation. By tuning the distances D_{12} and D_{13} , we aim to create two additional peaks beside the resonance frequency of the middle beam, close enough to merge the three together. Figure 4-7 shows the Power SIM simulation configurations.

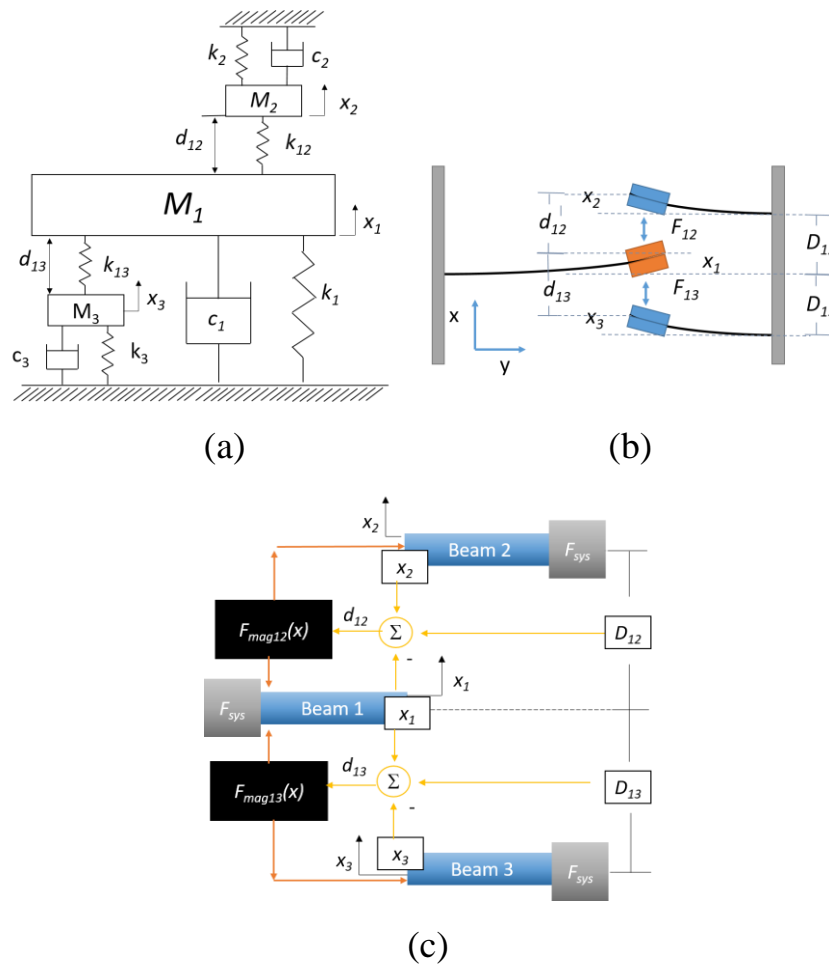


Figure 4-6 Interactions between three beams

(a) MCK model (b) schematic (c) block diagram

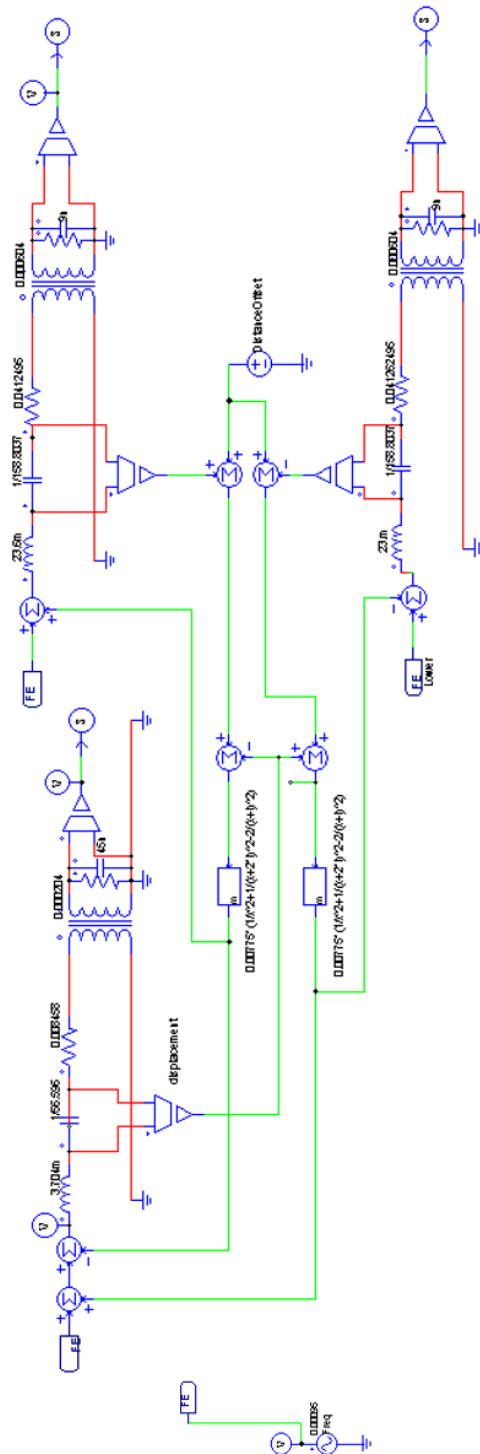


Figure 4-7 PSIM Simulation diagram for 3 beams

4.2.2.1 The Symmetric Alignment

To create the symmetric alignment, the two side beams are set with identical parameters. Then, we set D_{12} and D_{13} in Figure 4-6 to be identical so that the system is symmetric. The middle beam is designed to have a different resonance frequency, which is lower than that of the two. It was predicted that, the optimal effect would appear when only two targeting resonance frequency f_0 and $2f_0$ exist. By the simulation, we can visualize the optimal distance between the beams and how the resonance frequency is influenced by the magnetic force.

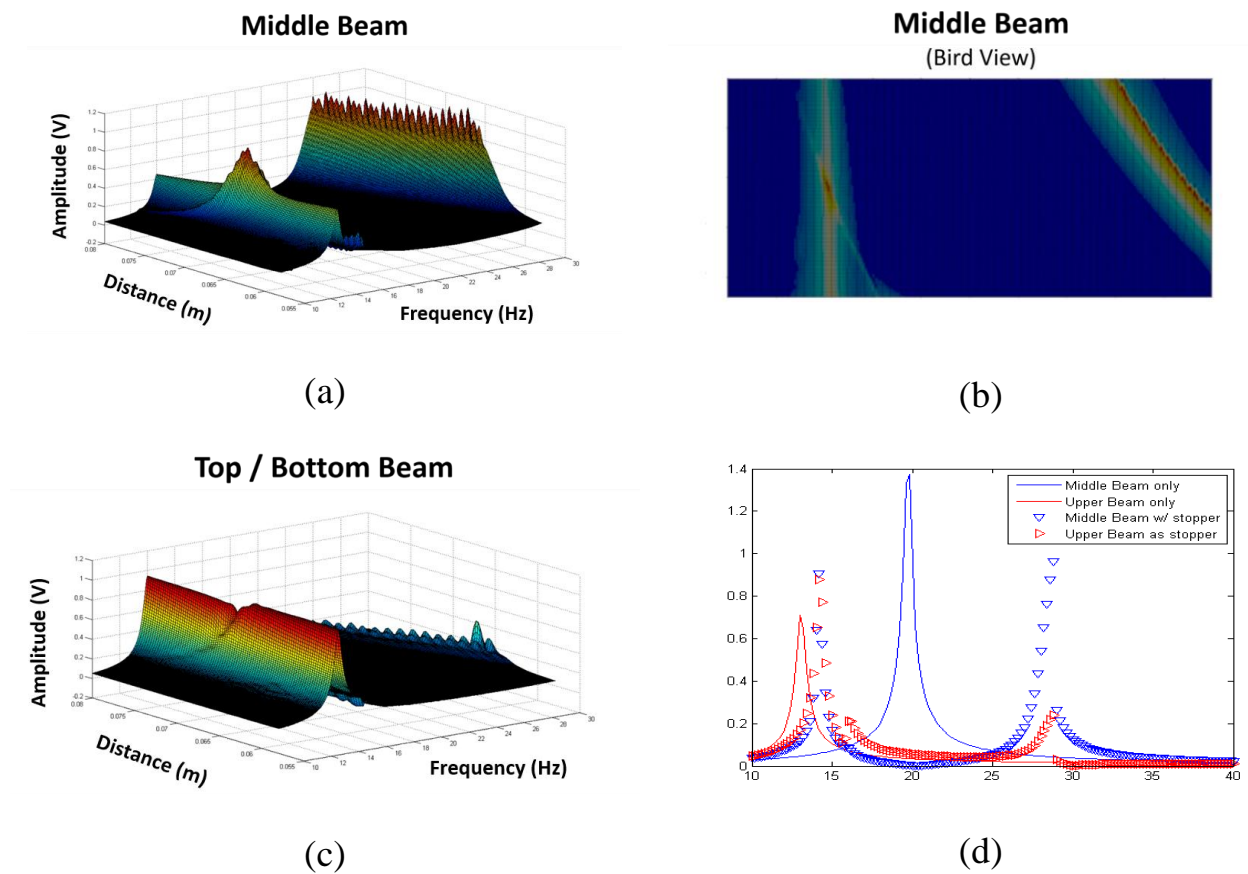


Figure 4-8 Simulation results for the symmetric 3-Beam alignment

- (a) 3D plot of the middle beam
- (b) Frequency-Distance plot of middle beam
- (c) 3D plot of the side beams
- (d) Voltage-Frequency plot on $D_{12}=0.072m$ separate and combined

From the 3D plot Figure 4-8 (a), one can observe that there is an additional voltage peak similar to that of the two-beam alignment. However, it is noteworthy that there exists an optimal distance which the influence is the highest. To compare, we look to the 3D plot showing the output of the side beams (Figure 4-8 (c)), there is a small valley on its resonance, where we could clearly inference it from the damping when interacting with the middle beam - that the energy is transferred to the middle beam. Another difference can be observed in Figure 4-8 (b), one can observe that the resonance frequency of the middle beam does not shift with the distance as much as the 2-beam alignment. A cross section of the 3D plot on the highest voltage of the middle beam, where the distance between the beams is 0.072m, is plotted on Figure 4-8 (d). From this plot, the depression of the middle beam output after installing the stopper can be observed. Two peaks for each beam were created, one up leveraged by the new natural frequency of the upper beam, and the other frequency slightly raised from the middle beam. On the other hand, the side beam is slightly enhanced, and also stricken by the resonance frequency of the middle beam. The middle beam, with is designed with higher displacement, and thus it also pushes the two side beams to a higher displacement level comparing to their own resonance.

Dirac Response

The Dirac response was also simulated, by providing a pulse force into the system, the ring down of the middle beam was observed, with or without the top/bottom beams. Results in Figure 4-9 showed that the ring amplitude was increased, and the ring time was prolonged. By integrating the power with time within the first 10 seconds, the single beam has an output of 1.0907 nJ. While installed in the structure, the output is 1.43 nJ, which is a 1.31 fold enhance.

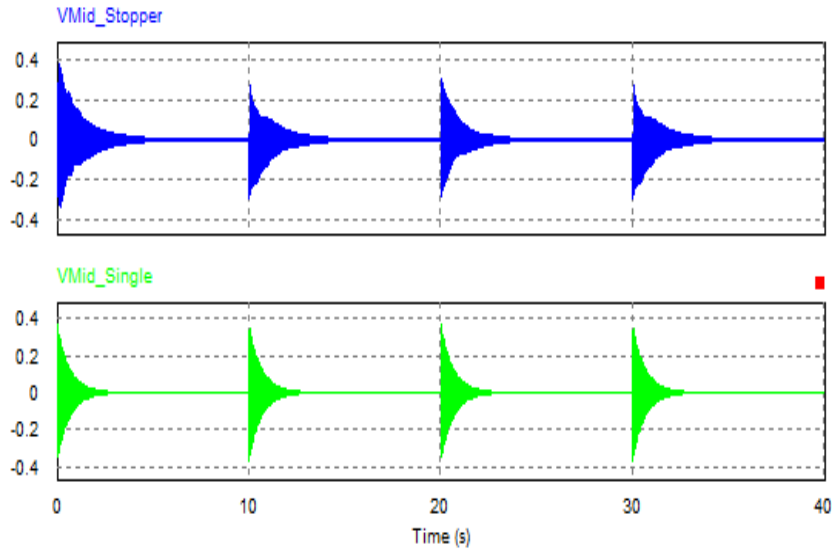


Figure 4-9 Simulation result of the Dirac response

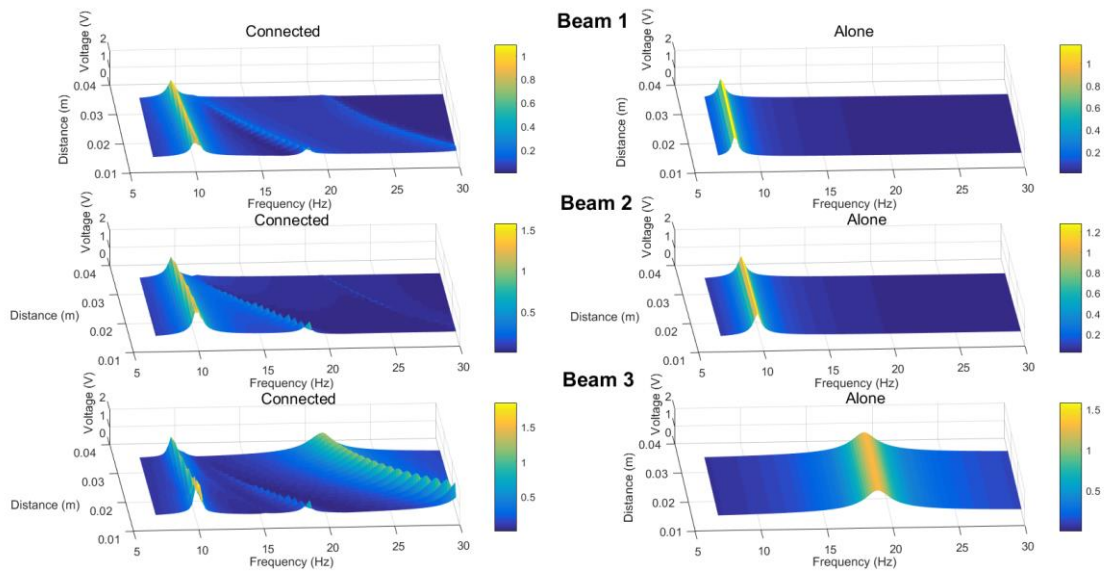
4.2.2.2 The Asymmetric Alignment

When three beams are set with different resonance frequency or distance, it is possible for us to design an output curve with three peaks. Thereby, the variables can be the resonance frequency and also the distance. To slightly tune the resonance in experiment, one can alter the resonance frequency by simply adding additional proof masses on the tip of the beam. Another method is to relocate the proof masses.

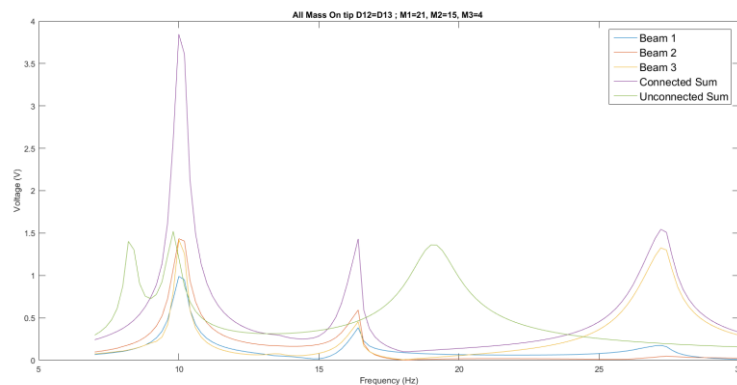
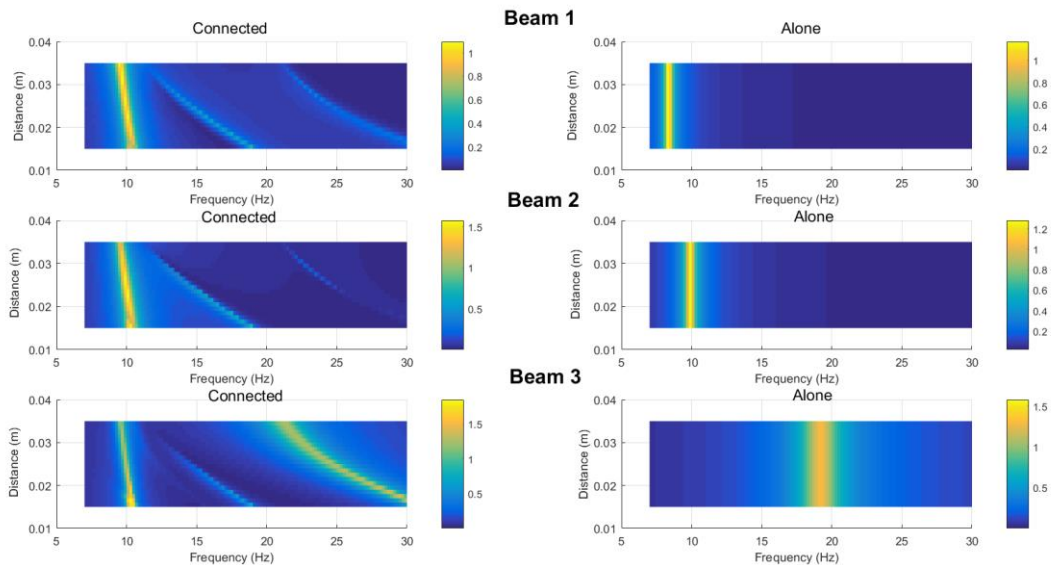
Firstly, to keep the simulation simple, the distances of D_{12} and D_{13} are kept identical, whereas the proof mass is adjusted to tune the resonance frequency. As an example simulation and to distribute the resonance frequency, the M value of each beam are: 21, 15, and 4 g, based on the spring steel beam structure of the middle beam, which is 75x15x0.5 mm in length, width and thickness. The simulation results are shown in Figure 4-10. On the left, the connected beam output are shown, whilst on right the Figure 4-10 (a) shows the 3D plot showing the resonance shift and amplitude change corresponding to the different inter-beam distances. From Figure 4-10 (b) one can have a bird view of the frequency shift.

For a clear vision of the effect in the middle beam, it is cross-sectioned in $D_{I2}=0.02$ m, and shown in Figure 4-10 (c). The “unconnected sum” curve indicates the voltage summation of the beams when they are not magnetically connected. M-Connected Sum, on the other hand, is the sum of the voltage output from the magnetically connected beams. The first resonance has a strong influence on all three beams, while the second, dominated by beam 2, is observed weaker. From which, one can observe that the middle beam (Beam 1, loaded with 21 g proof mass) is subjected to both side beams (Beam 2, proof mass 15 g, and Beam 3, loaded with 4 g), but the influenced output was relatively low compared to resonance 1. The third resonance was dominated by the beam 3. Observing the output, beam 2 and beam 3, which are smaller in mass, is unable to provide a higher influence comparing to beam 1.

Operating with beam 1 with a small mass and beam 2 and 3 with a higher could solve the problem. However, beam 1 would own a higher frequency comparing to the other 2, and much higher when sandwiched between the two beams. The operating frequencies would be too far to be considered.



(a)



(b)

(c)

Figure 4-10 Simulation results for asymmetrically aligned 3 beam array

(a) 3D plot of frequency – distance –voltage where $m_1=21$, $m_2=15$, $m_3=4$, $g=0.1g$, and identical beam lengths (b) Bird view showing the frequency shift (c) cross section of $D_{12}=D_{13}=0.02m$

To avoid the problem mentioned, and to create an evenly distributed output, another configuration was designed. The beams have their proof mass kept identical. As shown in Figure 4-11, the proof mass of beam 1 was moved to the middle of the beam, keeping identical beam length. In this way, beam 2 and 3 has enlarged force exerted to beam 1, which is considered shortened. On the other hand, beam 1 has its force reduced. Simulation results are shown in Figure 4-12. Figure 4-12 (a) shows

the 3D plot of the three beams, connected and operated alone. From the right of Figure 4-12 (b), one can observe that the resonance frequency of beam 1 shifted, and became higher than beam 2 when they are operated separately. This enables beam 2 to dominate the first resonance, and beam 1 the second. From the cross section plot shown in Figure 4-12 (c), one can observe that the amplitude of each resonance is more evenly distributed.

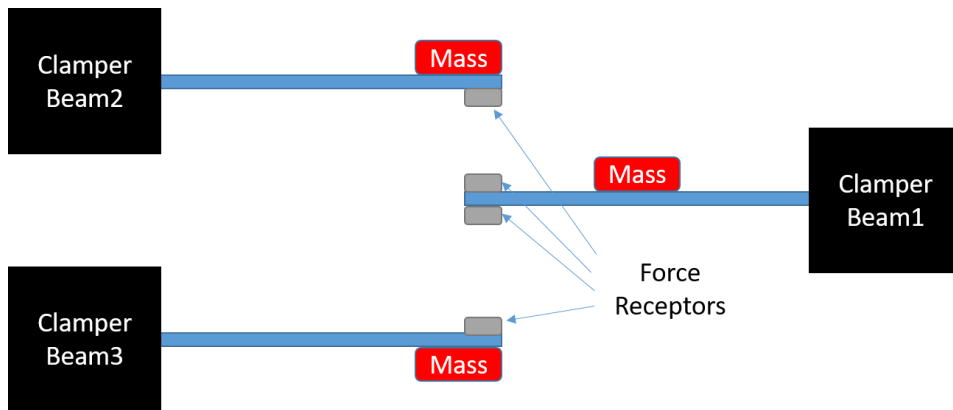
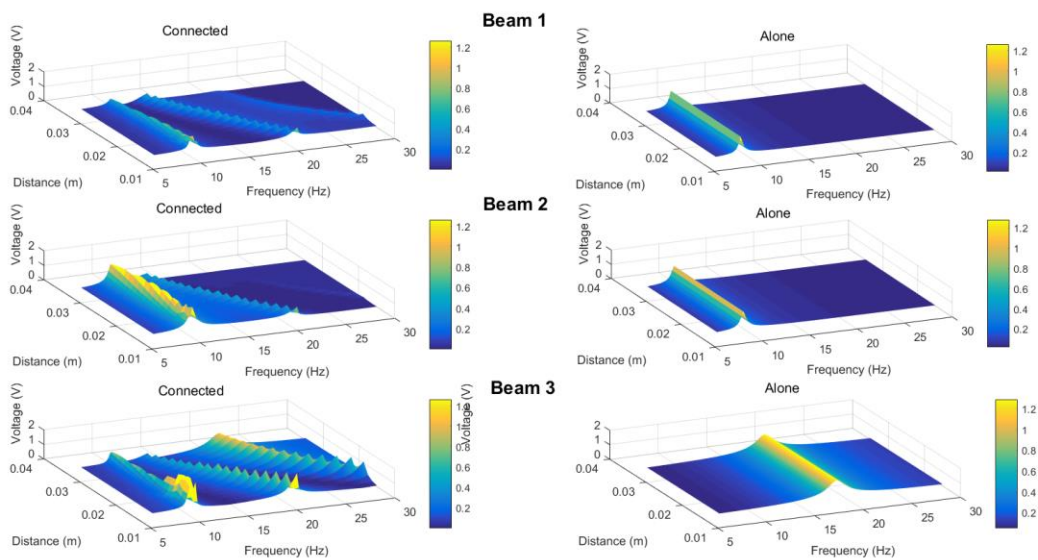
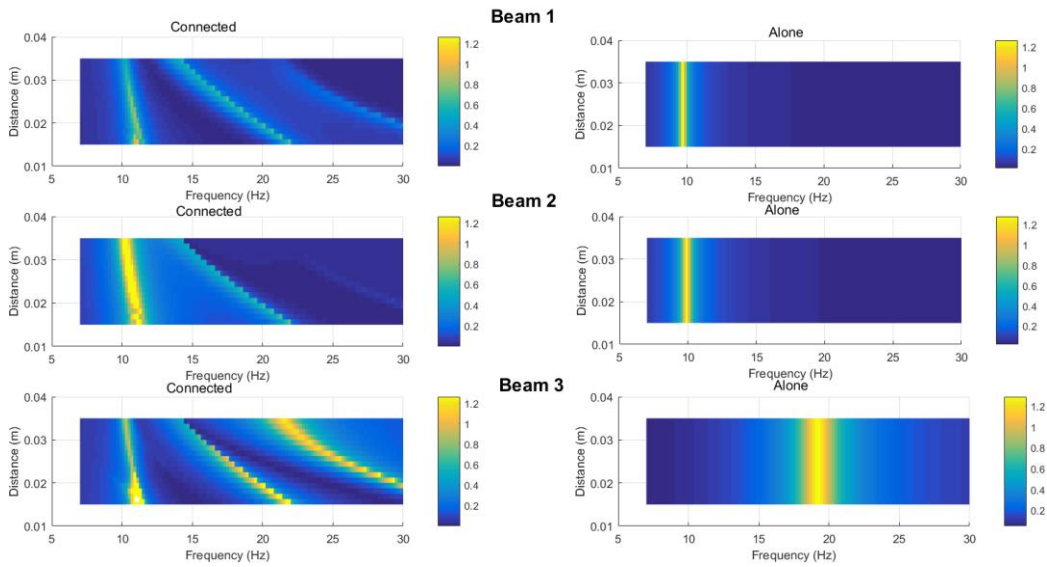


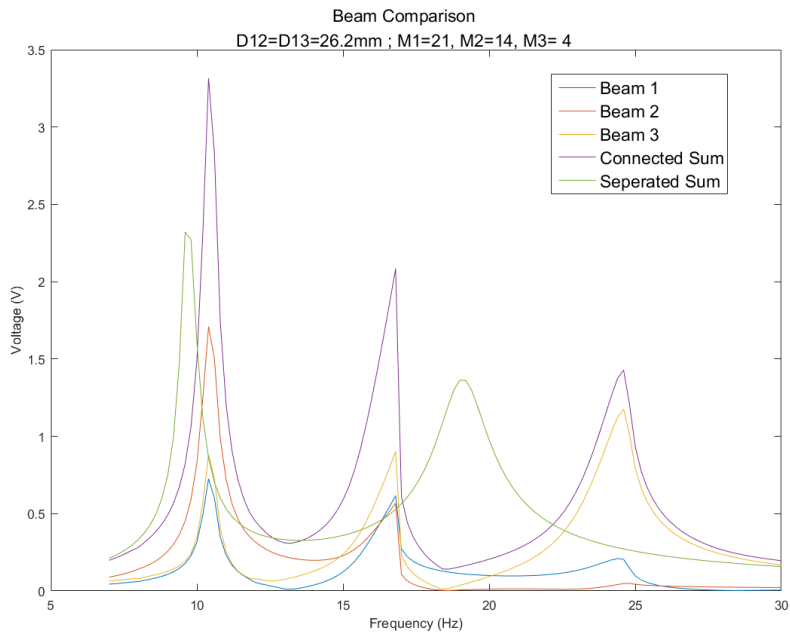
Figure 4-11 A new configuration for 3-beam alignments



(a)



(b)



(c)

Figure 4-12 Simulation results for the modified beam 1

(a) 3D plot of frequency – distance –voltage where $m_1=21$, $m_2=15$, $m_3=4$, $g=0.1g$, m_1 placed 25 mm from the tip and displacement $=D_{12}=D_{13}$ (b) Bird view showing the frequency shift (c) cross section of $D_{12}=D_{13}=0.0262m$

To shift the location of different peaks, in our example, we could also fix D_{13} ,

for example on $D_{13}=0.035\text{m}$, and move only D_{12} . In this way, one can define the operating bandwidth, as shown in Figure 4-13. The first and third resonance is relatively stable comparing to the shifting second resonance.

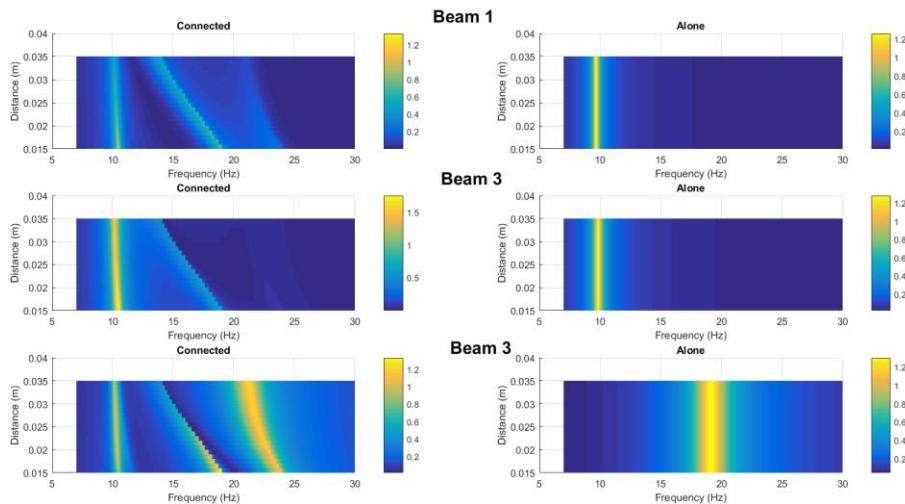


Figure 4-13 Bird view of frequency – distance –voltage for one fixed distance where $m_1=21$, $m_2=15$, $m_3=4$, $g=0.1\text{g}$ showing the frequency shift when D_{13} is fixed, m_1 placed 25 mm from the tip.

To bring the resonance closer, with $m_1 =14$ g, $m_2=10$ g, $m_3=4\text{g}$, the cross section on $D_{12} =D_{13}=35$ mm is shown as Figure 4-14. The overall output is increased, while the bandwidth is also increased.

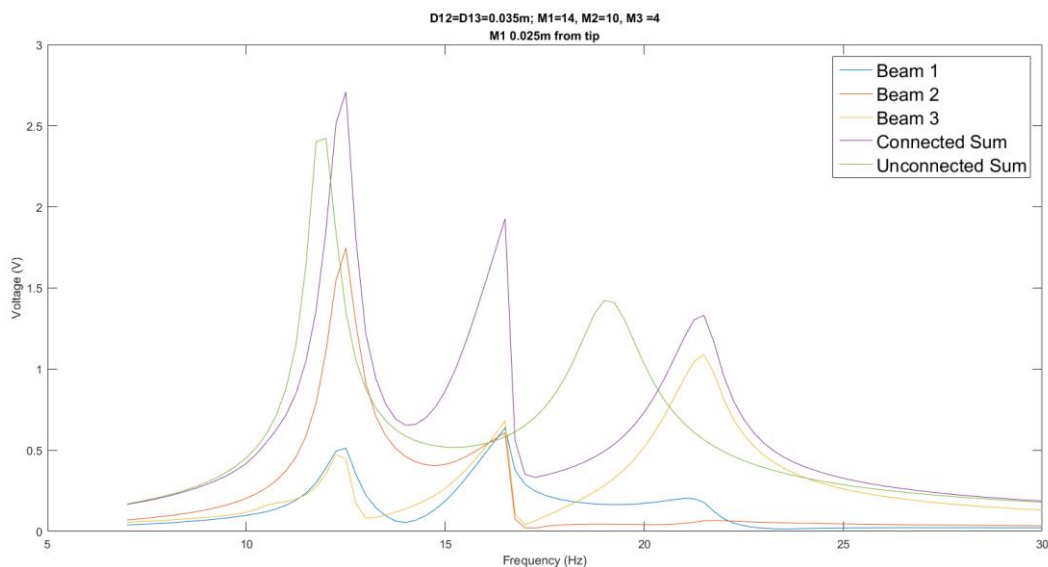


Figure 4-14 Cross section of $D_{12}=D_{13}=0.035$ m;
 $m_1=14$, $m_2=10$, $m_3=4$, m_1 placed 35 mm from tip. Driven on 0.1g.

4.3 Experiment

4.3.1 Experiment Setup

Spring steels were used as the substrate of the beams. The bonded piezoelectric patches on beam were PZT-KA-2 patches from Elecceram Technology Co., Ltd. The experiment setup is depicted in Figure 4-15, arrow pointing to the data flow direction. A shaker was used to provide vibration to the overall system, which consisted of three beam clampers, installed on threaded rods, in vertical, to provide Y directional rails. An X rail was also designed so that it can be easily tuned according to the beam length. A Data Acquisition Card from National Instrument (NI-DAQ) was used as an interface to instantly provide driving signals and record responding outputs in to the laptop. Beam outputs were directed to the DAQ card, and in the same time an oscillator for human observation. The driving signals from the DAQ card were to be amplified through a power amplifier so that there would be enough driving power for the shaker. To manipulate the NI-DAQ card, an NI-LabVIEW program is designed, to perform in-situ driving, monitoring, recording, and quick analyzing.

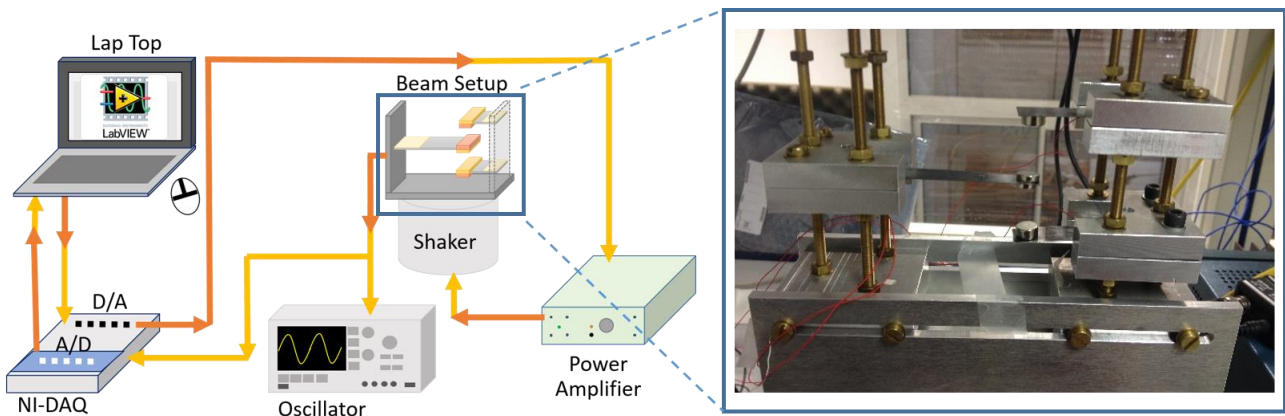
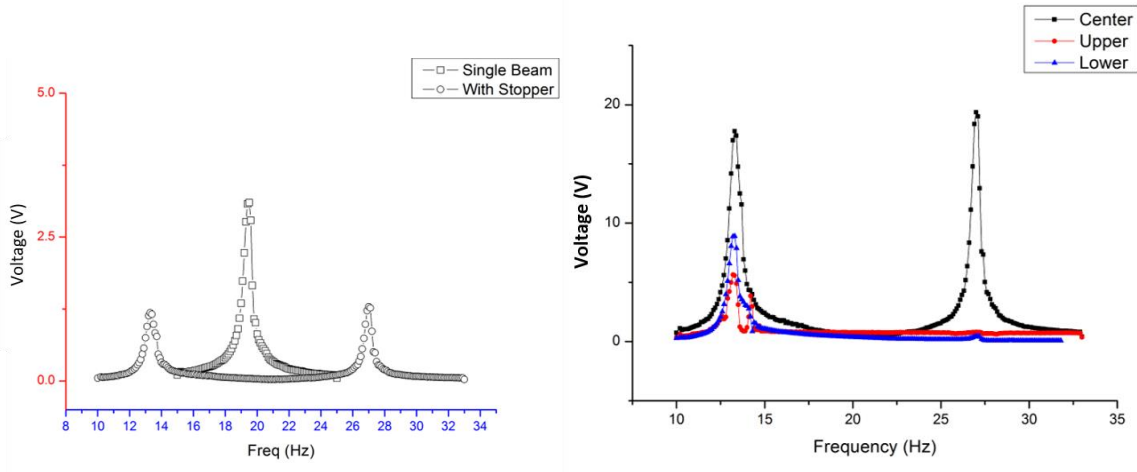
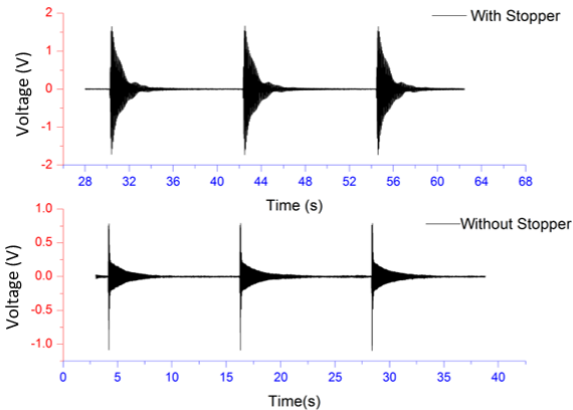


Figure 4-15 Experiment setup for magnetic connected beam array

4.3.2 Experiment results for symmetric alignment of 3 beams



(a) (b)



(c)

Figure 4-16 . Experimental results symmetric 3 beam alignment

(a) single middle beam with middle beam within the configuration of stopper beams (b) Voltage output responses with respect to a frequency scan (c) the transient response to pulse force inputs, (top) middle beam output

With beam 2 and 3 identical, the mass of 23.62g each, larger than that 3.7 g of beam. As shown in Figure 4-16 (a), the middle beam has its resonance raised to 26.8 Hz, and it is influenced by the two beams on the lower frequency, which is 13.5 Hz.

With this configuration, beam 2 and 3 holds a lower resonance, which strikes the middle beam. Beam 2 and 3 are heavy loaded and therefore the displacements are less affected by the light-weighted beam 1, Figure 4-16 (c). On the other hand, the displacement of beam 1 is also restricted by the heavier beam 2 and 3, resulting in the reduction of voltage output (Figure 4-16 (b)). Results in this experiment showed that, the two peaks were 13.3 Hz apart, and the bandwidth was not integrated to wide-band, the ringing was prolonged as the simulation results in Figure 4-9. When the system is applied with Dirac drive, the ringing amplitude was greatly enhanced by the additional beams due to the frequency harmonic match of the devices. This characteristic is ideal for up conversion and also non-periodic applications.

4.3.3 Experiment results for asymmetric alignment

For the asymmetric alignment, three identical beams made of spring-steel is made. The beams are also designed with the identical aspect ratio. In the experiment, different proof masses are loaded. As a standard, identical proof masses using 7.3g are used for defining the lump parameters for each beam. The beam parameters obtained from the experiment are listed below in Table 13. All experiments done in this section are driven under 0.04g.

Table 13. Beam Parameters for asymmetric 3-beam experiment

	Description	Units
Beam Dimension	Spring-Steel	
l (length)	75	Mm
w (width)	15	Mm
b (thickness)	0.5	Mm

Proof Mass 1 ($l*w*b$)	20*10*5	mm ³ (per piece)
Proof Mass 1	7e-3	Kg
Proof Mass 2 ($\phi*b$)	10*7	Mm
Proof Mass 2 (mass)	3e-3	Kg
Proof Mass 3 ($\phi*b$)	5*2	Mm
Proof Mass 3 (mass)	3e-4	Kg
Piezoelectric	PZT-KA2	
Patch Dimension	(Eleceram Technology Co., Ltd.)	
l (length)	6	Mm
w (width)	15	Mm
b (thickness)	0.13	Mm
Lump Parameters	(Beam 1' + Proof mass 7.3 g)	
f_0	11.54	Hz
f_1	11.58	Hz
C_0	9.65e-9	F
M	10.1e-3	Kg
K	53.46	N/m
η	2.52e-2	N s/m
K_D	145	
K_E	144	

Q_M	29.12
k^2	0.0069

Lump Parameters	(Beam 2' + Proof mass 7.3g)	
f_0	12.09	Hz
f_1	12.13	Hz
C_0	8.23e-9	F
M	10.5e-3	Kg
K	60.99	N/m
η	1.79e-2	N s/m
K_D	151.87	
K_E	150.88	
Q_M	44.68	
k^2	0.0066	

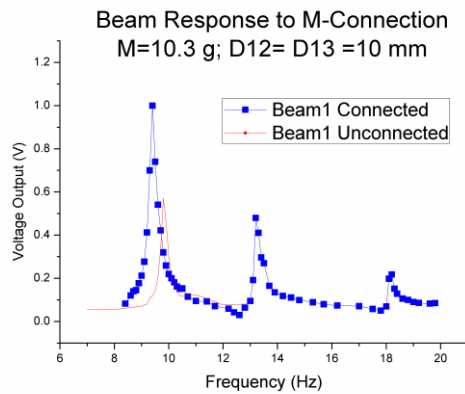
Lump Parameters	(Beam 3' + Proof mass 7.3g)	
f_0	11.94	Hz
f_1	12.10	Hz
C_0	10.72e-9	F
M	10.8e-3	Kg
K	62.12	N/m
η	2.23e-2	N s/m
KD	46.67	
KE	45.67	

Q_M	36.72
k^2	0.0214

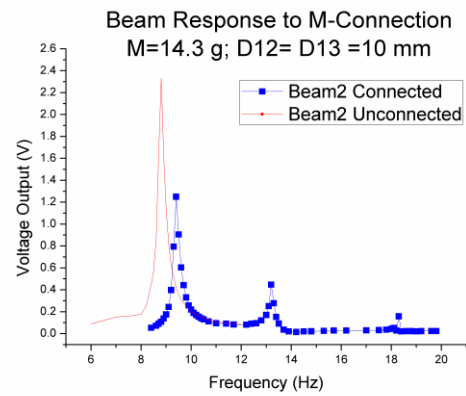
4.3.3.1 Original Configuration

The first experiment was performed with identical beam lengths and distances in between $D_{12}=D_{13}=10$ mm, and the different proof masses of 10.3, 14.3, and 8.27 g were loaded for beam 1, 2 and 3. The results are shown in Figure 4-17 (a-d). When separate beams are tested, the natural resonance of each beam is 9.7, 8.4, and 10.5 Hz each, for Beam 1, 2 and 3. As shown in Figure 4-17(a-c), when connected, the new resonance becomes 9.4, 13.2 and 18.2 Hz, in ascending order (not in beam order). Beam 1, subjected to both beam 2 and 3, has three peaking outputs. Observing beam 2 and beam 3, one can indicate that the first resonance is attributed to beam 2, and the second to beam 3. Observing the output of beam 2 and 3, we can also discover the coupling of beam 3 is much higher than that of the beam 2.

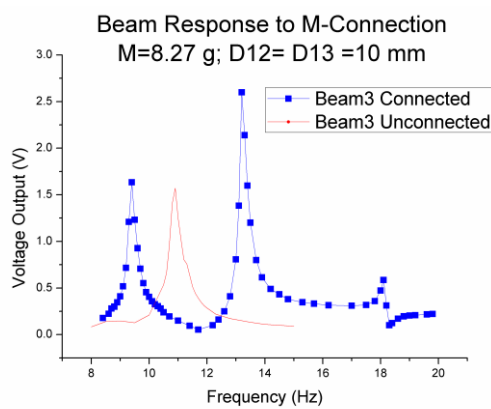
To compare the beams, the tip displacement is used instead of the voltage output since each beam has a different voltage / tip displacement ratio. Figure 4-17 (d) shows the displacement summation of the 3 beams when they are operated separately in the red line. The blue curve with box indicates the summation of the tip displacements from the magnet connected (M-Connection, as noted in the figure) beams. Results show that the displacement is enhanced, whilst the operating band not merged together. It is also noteworthy that the total displacement between the second and third peak is kept above 0.5mm.



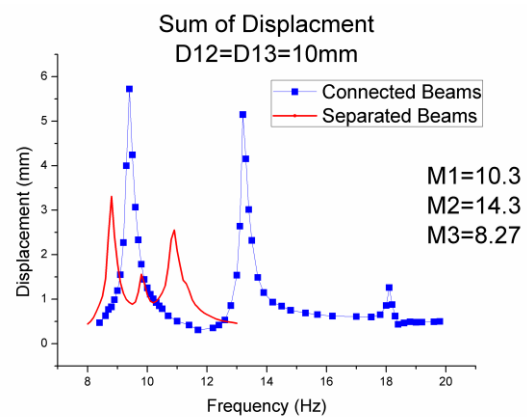
(a)



(b)



(c)



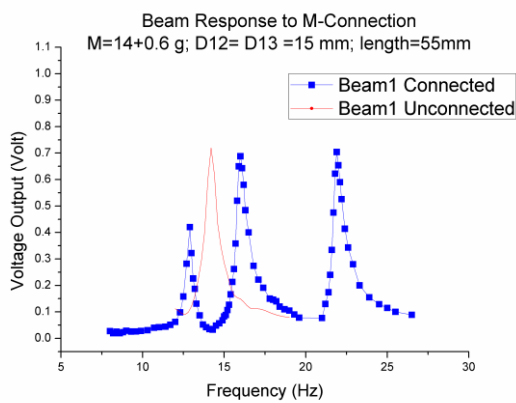
(d)

Figure 4-17 Experiment results of identical distances between beams. $D_{12}=D_{13}=10\text{mm}$. Voltage output is correspondent to the scanning frequency. (a) Beam 1 loaded with 10g, connected using magnetic forces and operated separately. (b) Beam 2 loaded with 14.3g, connected using magnetic forces and operated separately. (c) Beam 3 loaded with 8.27 g connected using magnetic forces and operated separately. (d) Sum of the voltage output of Beam 1-3, connected together or operated separately. Driven on 0.04g.

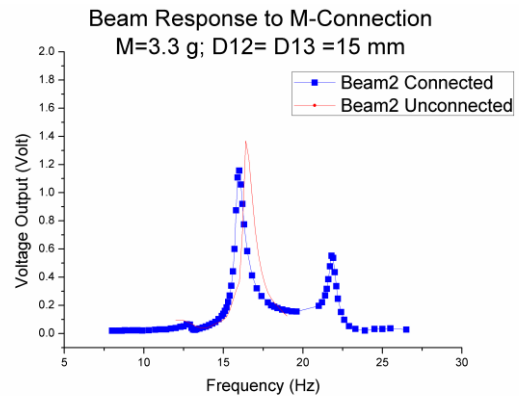
4.3.3.2 Modified configuration with proof masses shifted to the middle

The second configuration (shown in Figure 4-11) was used to increase the

coupling of the beams and to draw the resonating frequencies closer: beam 1 was loaded with a proof mass of 14 g, 2 cm away from the tip of the beam, and the tip was loaded with a pair of small magnets with the mass of only 0.3 g each. The magnets on tip serve as the force receptor, which can enhance the force exerted to the beam by using the lever principle. Placing the major proof mass in the middle of the beam can be assumed as a shorter beam. Thus, to keep the resonance frequency low, the proof mass was set much greater than the other two. To suit the resonance frequency of beam 1, the proof masses of beam 2 and 3 are set smaller so that the resonance is raised. Beam 2 is loaded with 3.3 g, while beam 3 with 6 g. D_{12} and D_{13} is set to be 1.5 cm. Results show that beam 2 and beam 3 also was affected by beam 1, and the voltage in between the peak was elevated. The first two peaks were drawn closer. Within the bandwidth, the total displacement level did not drop below 0.4 mm. The comparison of beam 1 before connection and after connection can be found in Figure 4-18 (a). As for beam 2 and 3, they can be found in Figure 4-18 (b) and (c), respectively. The voltage of the 3 beams were summed and then compared, before and after the magnetic connection. The voltage was also elevated, with however the three operating bandwidth also apart.



(a)



(b)

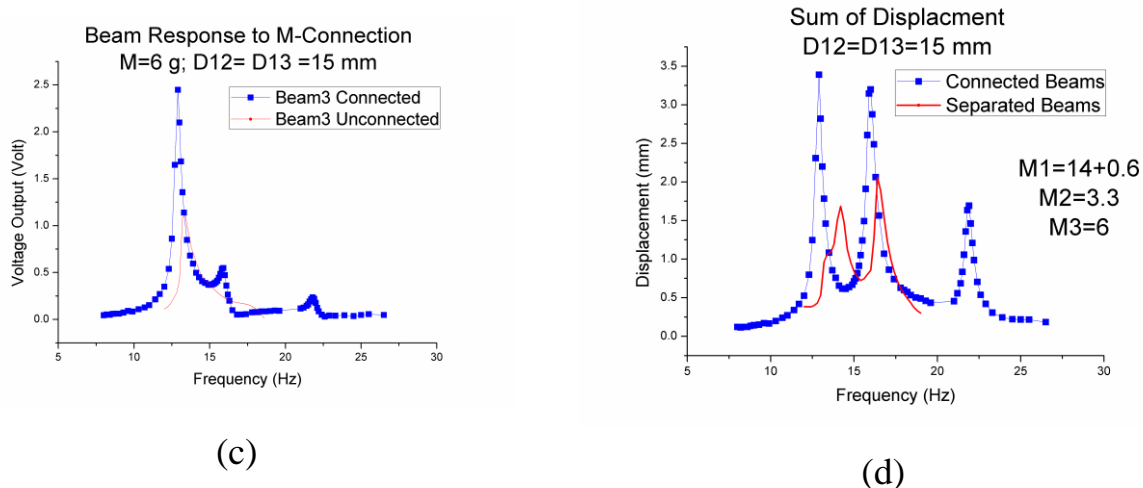


Figure 4-18 Experiment results of identical distances between beams. $D_{12}=D_{13}=15\text{mm}$.

Voltage output is correspondent to the scanning frequency. (a) Beam 1 loaded with 21g, 2 cm away from the tip, connected using magnetic forces and operated separately. Two small magnets of 0.3 g are used as the force receptor (b) Beam 2 loaded with 3.3g on tip, connected using magnetic forces and operated separately. (c) Beam 3 loaded with 8.27 g on tip, connected using magnetic forces and operated separately. (d) Sum of the voltage output of Beam 1-3, connected together or operated separately. Driven on 0.04g.

The third experiment shortens Beam 2 and 3 are then also shorten, in the way identical to the previous experiment. The proof masses are shifted to 25 mm away from the tip, 21.3 and 14.3 g are loaded for beam 2 and 3 each. The quality factor of beam 2 and beam 3 are lowered when they are operated separately. As consequence, the voltage output was also decreased. During this experiment, beam 1 is loaded with a relatively small mass, which is different from the experiment afore. Results are shown in Figure 4-19. Figure 4-19 (a) shows that beam 1, which is suppressed by the two heavier beams, provided a relatively low energy output when it is connected with the other beams. Beam 2. Figure 4-19 (b) shows that the output voltage of beam 2 is greatly enhanced. The voltage output between peak 1 and 2 was kept above 0.8 V between the two peaks of 13.1Hz and 16.4 Hz. Beam 3 has its displacement enhanced, as shown in Figure 4-19 (c). To compare the improvement, the

displacement of all three beams are then summed. Figure 4-19 (d) shows the summation results, one can observe that the overall displacement is enhanced, in spite of the band width separation.

Results showed that, despite the quality factor of beam 2 and 3 are raised again, the voltage output was greatly enhanced. Observing Figure 4-19 (d), with similar 1st and 2nd peak voltages of Figure 4-18 (d), the valley displacement in between peak 1 and 2 was increased from 0.6 mm to 2.2 mm.

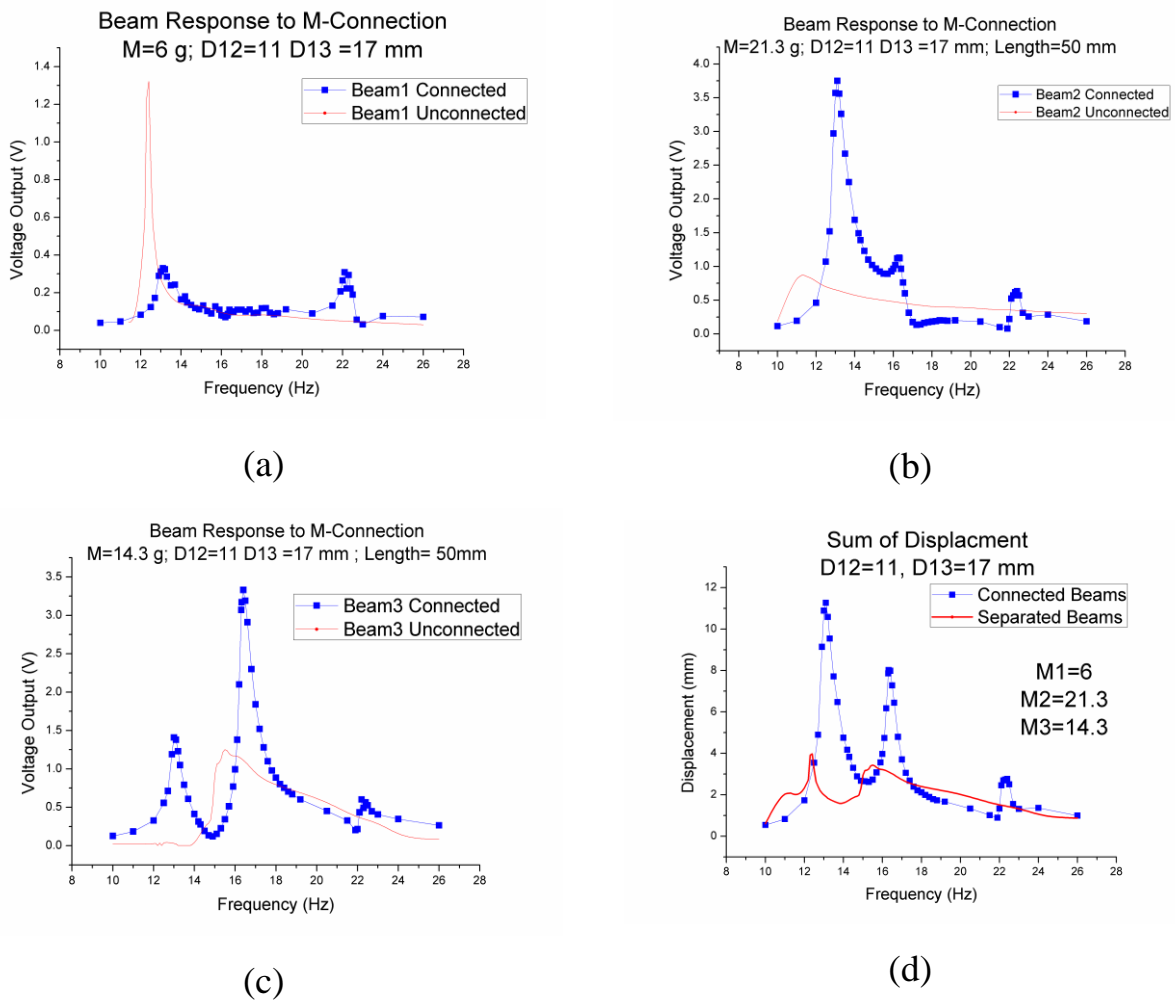
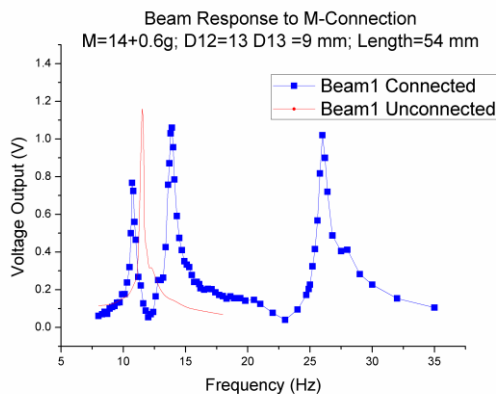


Figure 4-19 Experiment results of identical distances between beams. $D_{12}=11\text{mm}$, $D_{13}=17\text{mm}$. Voltage output is correspondent to the scanning frequency. (a) Beam 1 loaded with 6g, on tip, connected using magnetic forces and operated separately. (b) Beam 2 loaded with 21.3g, 25mm from tip, connected using magnetic forces and operated separately. (c) Beam 3 loaded with 14.3 g, 25mm from tip, connected using magnetic forces and operated separately. (d) Sum of the voltage

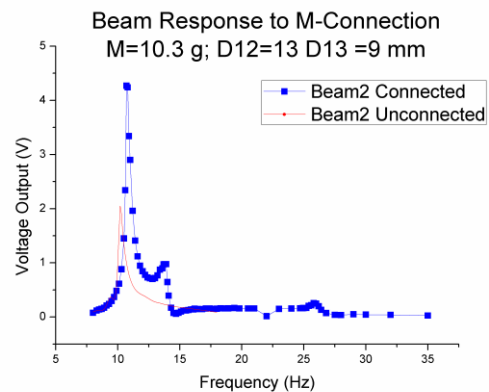
output of Beam 1-3, connected together or operated separately. Driven on 0.04g.

Pulling Close the Resonance

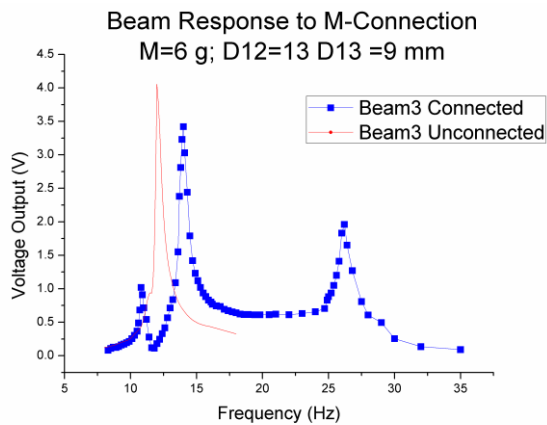
The subsequent experiment is performed with $D_{12}=13$ and $D_{13}=9$ mm. Beam 1 is loaded with 14g, 21mm away from the tip. Two receptors are also used in this configuration. Similar to that of the experiment 2, beam 2 and 3 are loaded with less weight: 10.3 g and 6 g, each. Results shown in Figure 4-20. Figure 4-20(a) shows that, in this setup, beam 1 is not enhanced in voltage, but it is able to provide all three peaking voltages outputs similar to its original output. Beam 2 has its voltage output enhanced by the striking of the other beams in the first peak frequency, as shown in Figure 4-20 (b). The output between the first two peaks (10.7Hz, 13.9Hz) is kept above 0.7 volts. As for beam 3, shown in Figure 4-20 (c), the peak output was reduced, but the overall range is also increased. The output between the second and third peak (13.9Hz, 26.5Hz) was also kept above 0.6 V. Figure 4-20 shows the sum of the beam tip displacements, connected and separated. As one can observe, not only the displacement is enhanced in Figure 4-20 (d), between the peaks of 10.7 and 26.5 Hz, the total displacement was kept above 1.24mm, which is the lowest point.



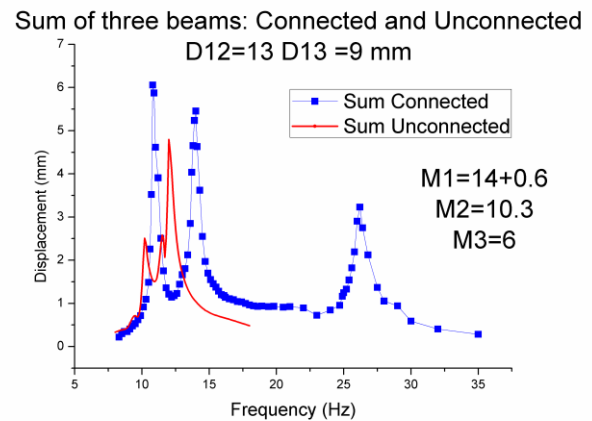
(a)



(b)



(c)



(d)

Figure 4-20 Experiment results of identical distances between beams. $D_{12}=11\text{mm}$, $D_{13}=17\text{mm}$. Voltage output is correspondent to the scanning frequency. (a) Beam 1 loaded with 6g, on tip, connected using magnetic forces and operated separately. (b) Beam 2 loaded with 21.3g, 25mm from tip, connected using magnetic forces and operated separately. (c) Beam 3 loaded with 14.3 g, 25mm from tip, connected using magnetic forces and operated separately. (d) Sum of the voltage output of Beam 1-3, connected together or operated separately. Driven on 0.04g.

To draw the first two peaks near, a 7g proof mass was added to beam 1, increasing the new proofmass of beam 1 to 21g. The pair of 0.3 g receptor is also used. Figure 4-21(a) shows the affected result of beam one with the blue boxed curve. Comparing to the unconnected beam, The voltage level is kept, but two other peaks are also created. The output level of beam 2 is elevated, the second peak in the plot, is partially merged with the first, as shown in Figure 4-21(b). As shown in Figure 4-21 (c), three voltage peaks can also be found in the output of beam 3. Similar to the previous result of Figure 4-20 (d), the displacement level of a single peak is kept, while additional resonance is created.

The first and second peaks are drawn near as expected, creating a bandwidth

similar to the sum of the beam displacement when driven separately. The displacement of the second peak was also higher than the beams operated separately, not to mention the additional third peak voltage. Between the three peaks, the total displacement of the interfered beams was kept above 1.54 mm.

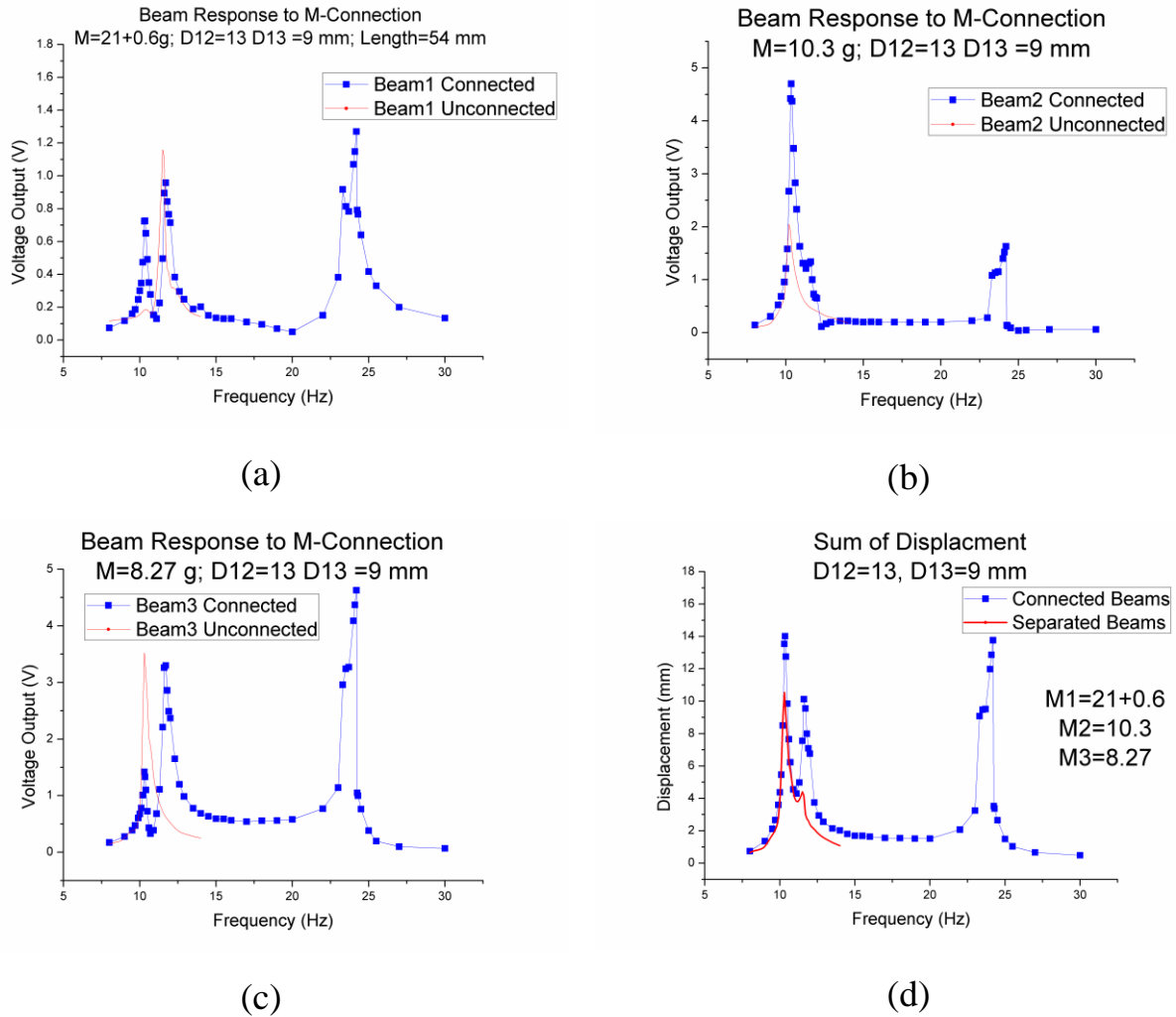
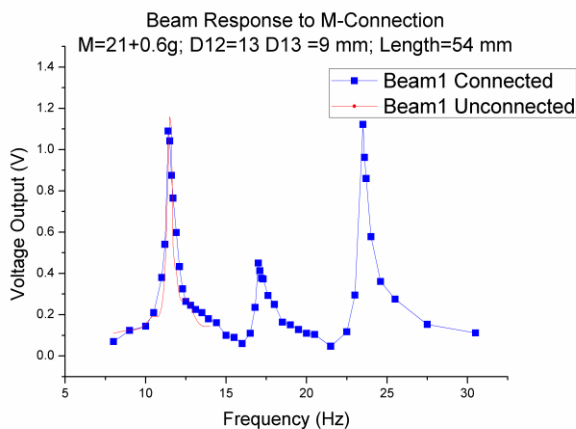


Figure 4-21 Experiment results of identical distances between beams. $D_{12}=13\text{mm}$, $D_{13}=9\text{mm}$. Voltage output is correspondent to the scanning frequency. (a) Beam 1 loaded with 21g, 21 mm from tip, connected using magnetic forces and operated separately. (b) Beam 2 loaded with 10.3g, on tip, connected using magnetic forces and operated separately. (c) Beam 3 loaded with 8.27 g, on tip, connected using magnetic forces and operated separately. (d) Sum of the voltage output of Beam

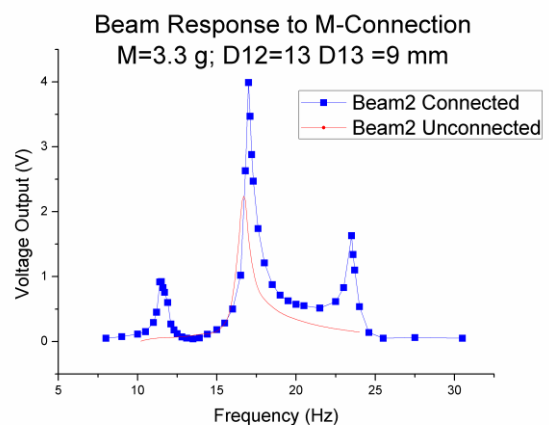
1-3, connected together or operated separately. Driven on 0.04g.

Evenly Distributing the Resonance

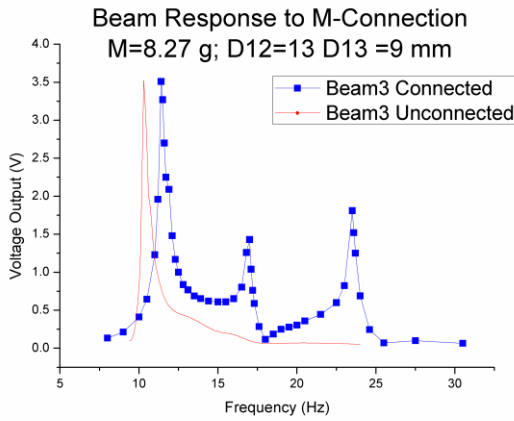
The last experiment was done to evenly disperse the peak voltages. Beam 1 and 3 are kept identical to the experiment of Figure 4-21, while the proof mass of beam 2 is reduced to 3.3g. This brings the first resonance peak to the middle, from 10.35 Hz to 17 Hz. Figure 4-22 shows the results of the last experiment. Beam 1, indicated in Figure 4-22 (a), is affected by beam 3, forming the first peak. The second peak was lower, due to the small proof mass of the second beam. And third, the resonance of its own. One can also observe that, comparing to its original output when not connected, the new output creates also new peaks for beam 1. Beam 2, with its new resonance frequency at 16.8Hz, is also affected by the other beams. Between the peaks of 17Hz and 23.5Hz, the voltage level was also kept above 0.51 V. Beam 3, shown in Figure 4-22(c), has also non-falling output between 11.4 Hz and 17Hz, the voltage is kept above 0.61V. As for the displacement, Figure 4-22 (d) shows that the overall displacement is kept above 1.56 mm, between the peak frequencies 11.4 and 23.5. Comparing to the beams operated separately, the total displacement is not only increased, the lowest displacement between the peaks are also elevated.



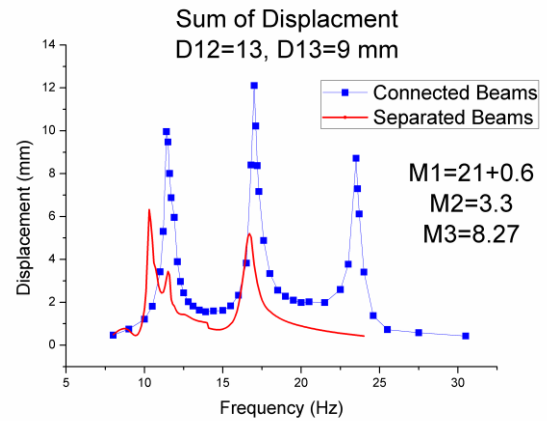
(a)



(b)



(c)



(d)

Figure 4-22 Experiment results of identical distances between beams. $D_{12}=131\text{mm}$, $D_{13}=9\text{mm}$.

Voltage output is correspondent to the scanning frequency. (a) Beam 1 loaded with 21g, 21 mm from tip, connected using magnetic forces and operated separately. (b) Beam 2 loaded with 3.3g, on tip, connected using magnetic forces and operated separately. (c) Beam 3 loaded with 8.27 g, on tip, connected using magnetic forces and operated separately. (d) Sum of the voltage output of Beam 1-3, connected together or operated separately. Driven on 0.04g.

5.4 Discussion

For the 3-beam configurations, experiment showed similar trend to the simulation. However, the ideal output of connecting all bandwidths was not realized, accusing to the selection of the magnets. The mass of the magnets cannot be easily selected with identical magnetic flux. The only way to tune the resonance frequency and not altering the force is to shift the location of the magnets. Adding magnets of different size can alter the proof mass but the magnetic force of different piece is not constant. Therefore, it is difficult for one to control the mass and the magnetic force to be identical to the optimized solution of the simulation.

Experimentally, the output voltage enhanced in some beams are much higher than what we obtained in the simulation. During simulation, when the distances between the beams are placed too close, severe electric signal oscillation occurs, and the output is out of scale. However, in practical experiments, the mechanical

structure hinders the device from over swinging, with however increased output levels. The overall power was able to be increased in most configurations, which is similar to the results of the simulation.

Experiment for different mass distributions on the three beams was performed. A massive beam 1 would cause the effects of beam 2 and 3 to be small on beam 1. Beam 2 and 3 will be efficiently induced by the beam 1. But the influenced peaking frequencies from beam 2 and 3 on beam 1 will also be limited. Vice versa, if beam 2 and 3 are too massive comparing to beam 1, the displacement of beam 1 affecting beam 2 and 3 was limited. As the new solution shown in Figure 4-11, the proof mass was moved to the middle of the beam 1, while the tip, is mounted with a force receptor. This would enable beam 1 to receive an enlarged force, keeping the displacement. On the other hand, despite the force applied to the beam 2 and 3 are reduced, the displacement of beam 1 was enlarged mechanically by the beam.

When it comes to the bandwidth, it is difficult to assign to the output because the output shape does not have a standard. However, observing each beam with connection, additional voltage peaks with considerable levels are created. One should also note that, the up-levered valley outputs between the 3 peaks, enables a better chance of usable power.

Chapter 5. Conclusion and Future work

5.1 Hybrid Switches

A mechanical-electrical hybrid self-powered SSH technique was proposed using reed switch. The proposed switch serves also as a displacement detector to enable the switch driving in the SSH technique. Among the various proposed methods, three are considered the most feasible for practical use.

Compared to the electric self-powered switching techniques which create additional impedances and also power losses, the triggering of the switch is mechanical. However, there are still some factors that induce losses: the chattering. The energy cost of the chattering is determined by the characteristics of the switch and also the arrangement of the SSH technique. P-SSHI showed lower loss of $1.17\mu\text{W}$ out of the optimal power harvested from externally powered $42.26\mu\text{W}$. For S-SSHI, the loss is $3.82\mu\text{W}$ loss out of $46.59\mu\text{W}$. Even with a higher loss, the power output of the S-SSHI is still higher than that of the P-SSHI.

The hybrid switch is also hindered from its mechanical characteristics, displacements too high or too low causes energy losses. One most important defect is that, when the system is connected in S-SSHI and the displacement is not reaching the PI zone, zero energy can be harvested. In case of random displacements, P-SSHI can be considered. When the displacement is over-driven, the switching time difference should be considered. Of a switching difference of 0.6 rad , more than 30% of energy loss can be caused in both S-SSHI and P-SSHIs.

5.2 Magnetically Connected Arrays

The M-MDOF creates different peak outputs in a singular beam. Despite the optimal operating frequency is still depending on the beams, the output in between is also up-levered. By which, it also sidesteps the highly stressed structure in the MDOF designs where a mother system carries multiple child systems. Comparing to the mother-child system, the multiple beams can also provide resonance frequencies closer to each other.

As a beam array, the circuitry for interface circuits should be highly concerned for the best efficiency. In previous works, researchers find that different connections will affect the output characteristics of multiple beam connection. Thus, another

connecting circuit was referenced to connect the multiple beams together without interference between the beams.

Experiment results also showed that the overall output power was increased using the magnetically connected beam array using the asymmetric configuration.

For practical applications, the symmetric three-beam design has also shown the experiment result of prolonged ringing. It indicates a promising characteristic for up-converting methods and also random excitations in longer time gaps (lower than 1 Hz), which can also be further more discussed.

5.3 Summary (Impact)

In this work, two new techniques were proposed. The techniques are simple, easy to perform, but efficient. First, the non-contact SSH switch based on reed switch was proposed. This new switch configuration can be driven in ultra-low power conditions, such as 1~2 μW . Under the low power supplied condition, the switch with LC and SCR debouncers showed high efficiency of more than 99% comparing to the active driven S-SSHI. Secondly, a new broadband technique inheriting the merits of MDOF and beam array is proposed. The technique greatly enhanced the output voltage of the beam array, and is also able to create broader output ranges in a single beam. The technique was also found to enhance beam ringing, which is an optimistic choice for up conversion or pulse driven applications. Moreover, comparing to MDOF designs, the stress is relieved for that the device does not have mother-child structure, while all three beams are connected together via magnetic force.

5.4 Future Work

5.4.1 The hybrid switches on miniaturized systems

As our ultimate goal is to apply the system in to Micro-PEH systems. The SCR hybrid switch method presented in section 4.1.3.3 was then applied on a micro-energy harvesting system for a preliminary experiment for the future work.

The micro-piezoelectric harvester is a stainless steel based device, fabricated by aerosol deposition to create a film of 10 μm [95]. The device is fabricated with the process proposed in [10], with a relatively low power output of approximately 10.56 μW unrectified. The low output enabled us to inspect and assure the method's feasibility to be applied in limited energy resources. P-SSHI was used in this experiment, with 59170 sub-miniaturized over-molded reed switches up and below the beam. Small magnets were bonded on the tungsten proof mass below the beam, and also on the top of the beam. The P0130AA SCR was used to snub the chattering. Results show that the SSHI correctly works even with a low voltage output of the piezoelectric device, which is 5.2 V_{p-p} . With the piezoelectric output of 5.2 V peak to peak, the P-SSHI was able to lever the voltage to 22 V_{p-p} .

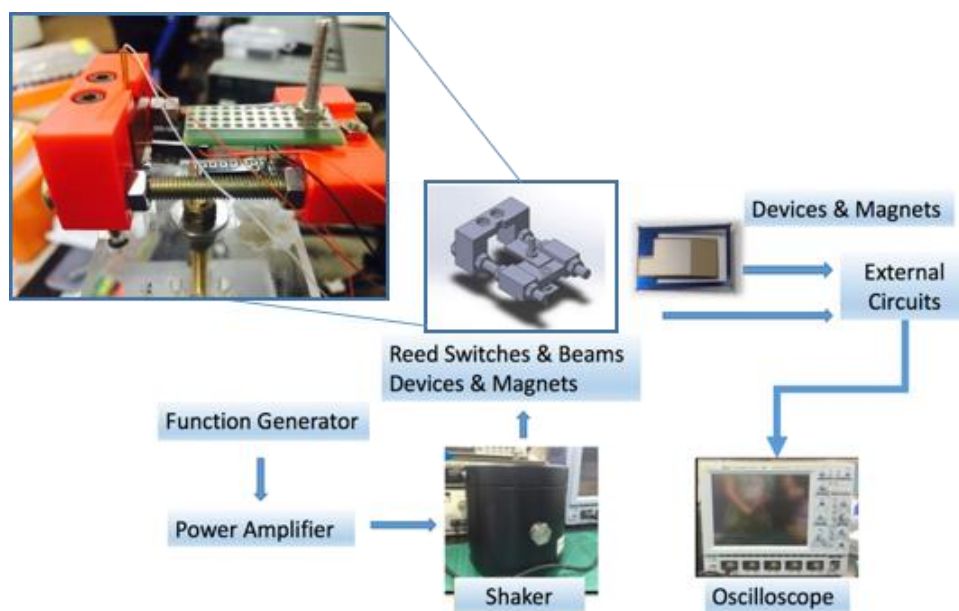


Figure 5-1 Experiment setup of the Micro PEH with reed switch SSH

The power experiment result showed that the output power from the reed switch based P-SSHI was 8.53 μW , in comparison to the power output of 6.63 μW of the SEH. The driving conditions are under the resonance frequency of 91.4Hz, on acceleration of 1.302g. The beam displacement amplitude was 1.6 mm peak. With the optimal load of the device 300 k Ω , and the AC power output (unharvested) of 10.56 μW . This experiment showed the feasibility of our proposed technique under ultra low energy conditions.

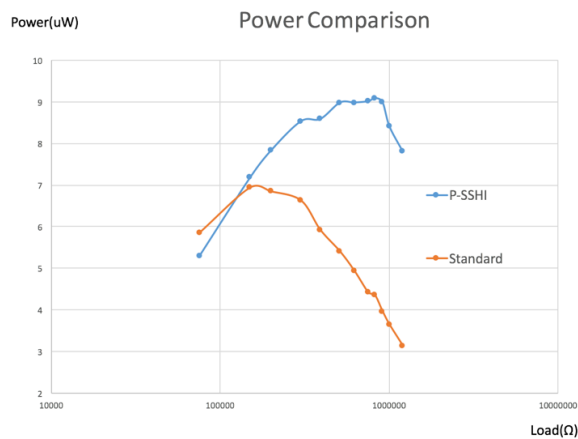
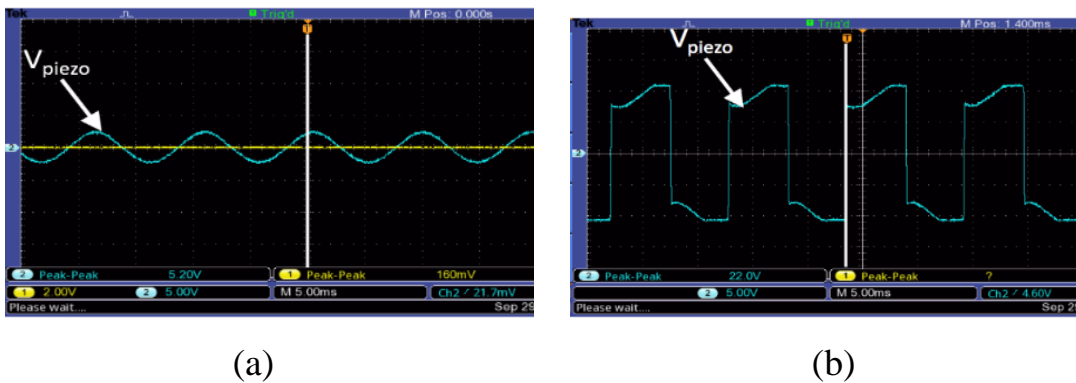


Figure 5-2 Experiment results of SCR P-SSHI using micro piezoelectric energy harvester
 (a)SEH waveform (b) P-SSHI waveform (c) comparison of harvested power

It is proved successful when the hybrid switch is applied in P-SSHI. However,

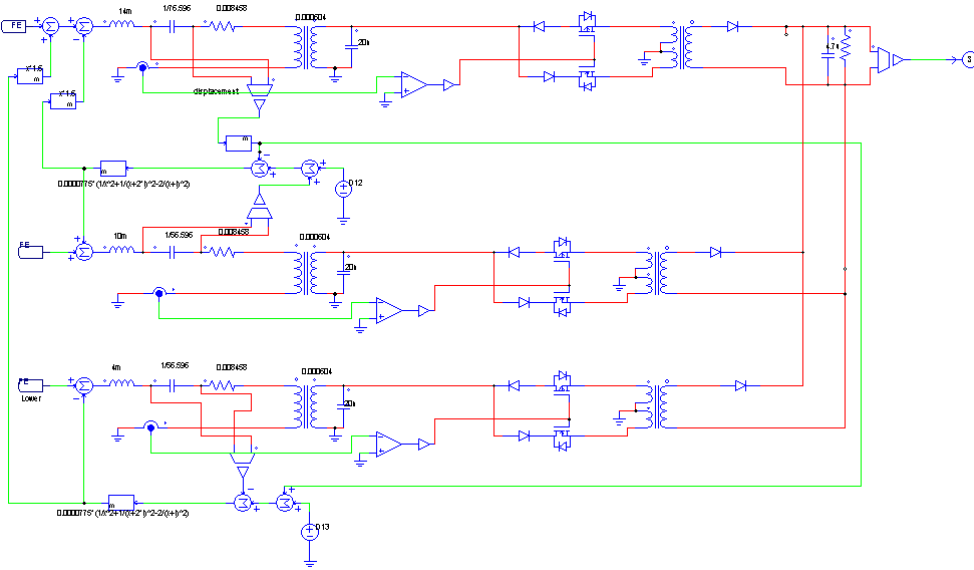
detailed studies for system packaging and circuitry losses are yet to be investigated.

5.4.2 Magnetically connected beam arrays

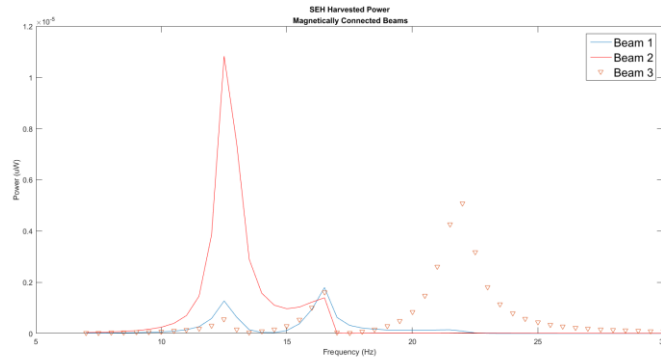
Despite the experiment showed some difference to the simulation, the trend is similar. Discussions for different mass ratios or beams with different quality factors may also improve the performance of the setup. In the future, the design can also be miniaturized for micro-PEHs. On bulk or miniaturized systems, the prolonged ring time of the beams can be also furthermore studied, for the sake of random frequency excitations and also up-conversion applications.

To combine the output power for the beam array, the circuit referencing [96] was proposed, the power of simulation Figure 4-14 was applied with the OSECE circuit to sum up the harvested energy. The OSECE circuit was operated separately and also combined as the Figure 5-3(a) shown below. Results are shown in Figure 5-3(b). Results showed that the current-based summing circuit suffers from some losses, and that the peaking frequencies does not appear on the OSECE harvested power. SEH was used as a comparison standard. Observing the results SEH, the multiple beam effects were kept, while on OSECE, the optimal power only shows on the tuned resonance, but not the other peak voltages. There are several possibilities that may lead to this result and can be further discussed: Firstly, the SSH techniques, which is based on extracting the natural resonance frequency may not be sufficient for passively driven system like what was proposed in this work.

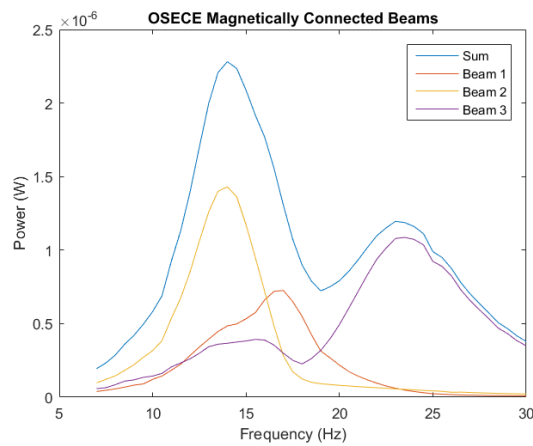
Another possibility can be referred to the simplified model of the system may not be precise enough to resemble the non-linearity. Further experiments for circuitry can be performed to understand.



(a).



(b)



(c)

Figure 5-3 Circuit simulation for summing up the harvested power

(a) circuit diagram of the magnetically connected beams, using the circuit proposed by [96] (b) SEH harvested power (c) OSECE harvested power

Table of abbreviations

IoT	Internet of Things
MDOF	Multi-Degree of Freedom
TE	Thermal Electric
SEH	Standard Energy Harvesting
SSH	Synchronized Switch Harvesting
PEH	Piezoelectric Energy Harvester
MEMS	Micro-electro-mechanical-systems
SSD	Synchronized Switch for Damping
SSHI	Synchronized Switch Harvesting on Inductance
SECE	Synchronous Electric Charge Extraction
SSDCI	Synchronized Switching and Discharging to a storage Capacitor through an Inductor
DSSH	Double Synchronized Switch Harvesting
LF-P-SSHI	Load Free Parallel SSHI
P-SSHI	Parallel SSHI
S-SSHI	Series SSHI
PI	Pull-in
DO	Drop-out
SCR	Silicon Controlled Rectifier
RDR	Reed De-bounced on Resistor
RDI	Reed De-bounced on Inductor
SP-SSHI	Self-Powered SSHI

REFERENCES

1. Gas, A.f.t.S.o.P.O. 2007 [cited 2007; Available from: https://aspo-ireland.org/newsletter/en/pdf/newsletter73_200701.pdf.
2. Evans, D. *The Internet of Things How the Next Evolution of the Internet Is Changing Everything*. 2011.
3. Energy, S.H. *What is a "Smart Home"?* [cited 2017 13, Sept]; Available from: <http://smarthomeenergy.co.uk/what-smart-home>.
4. Thomas, S. *Energy Harvesting Market by Source, System & Application Forecast 2017-2024*. 2017. 4.
5. Coporation, C. *Energy Harvesting & Storage*. 2017; Available from: <http://www.cymbet.com/design-center/energy-harvesting.php>.
6. Roundy, S., et al., *Improving power output for vibration-based energy scavengers*. IEEE Pervasive Computing, 2005. **4**(1): p. 28-36.
7. Saravanakumar, B. and S.-J. Kim, *Growth of 2D ZnO Nanowall for Energy Harvesting Application*. The Journal of Physical Chemistry C, 2014. **118**(17): p. 8831-8836.
8. Cho, H., J. Park, and J.Y. Park, *Micro-fabricated flexible PZT cantilever using d33 mode for energy harvesting*. Micro and Nano Systems Letters, 2017. **5**(1): p. 20.
9. Minh, L.V., et al., *Vibrational micro-energy harvesters utilizing Nb-doped Pb(Zr,Ti)O₃ films on stainless steel substrates*. Journal of Physics: Conference Series, 2016. **773**(1): p. 012003.
10. Lin, S.-C. and W.-J. Wu, *Piezoelectric micro energy harvesters based on stainless-steel substrates*. Smart Materials and Structures, 2013. **22**(4): p. 045016.
11. *Small Size PV*. 2017; Available from: <http://www.solarnovus.com/machine-vision-aids-photovoltaic-manufacturing-N833.html>.
12. *Large Scale PV*. Available from: http://www.jc-solarhomes.com/PV/Photovoltaic_Discoveries.htm.
13. Mouis, M., et al., *Thermal Energy Harvesting*, in *Beyond-CMOS Nanodevices I*. 2014, John Wiley & Sons, Inc. p. 135-219.
14. *What is thermal energy harvesting?* 2015 [cited 2017 14, Sept]; Available from: <http://www.europanthermodynamics.com/news/what-is-thermal-energy-harvesting>.
15. Vyas, R., et al. *A battery-less, energy harvesting device for long range scavenging of wireless power from terrestrial TV broadcasts*. in *Microwave*

- Symposium Digest (MTT), 2012 IEEE MTT-S International*. 2012. IEEE.
16. Wu, Z., et al., *An energy harvesting bracelet*. Applied Physics Letters, 2017. **111**(1): p. 013903.
 17. Crovetto, A., F. Wang, and O. Hansen, *Modeling and optimization of an electrostatic energy harvesting device*. Journal of Microelectromechanical Systems, 2014. **23**(5): p. 1141-1155.
 18. Sterken, T., et al. *Harvesting energy from vibrations by a micromachined electret generator*. in *Solid-State Sensors, Actuators and Microsystems Conference, 2007. TRANSDUCERS 2007. International*. 2007. IEEE.
 19. Lo, H.-w. and Y.-C. Tai, *Parylene-based electret power generators*. Journal of Micromechanics and Microengineering, 2008. **18**(10): p. 104006.
 20. 李, 柏.B.L., *Piezoelectric MEMS cantilever power generators for vibration energy harvesting*, in *Engineering Science and Ocean Engineering*. 2010, National Taiwan University. p. 109.
 21. Guyomar, D. and M. Lallart, *Recent progress in piezoelectric conversion and energy harvesting using nonlinear electronic interfaces and issues in small scale implementation*. Micromachines, 2011. **2**(2): p. 274-294.
 22. Yang, Y. and L. Tang, *Equivalent Circuit Modeling of Piezoelectric Energy Harvesters*. Journal of Intelligent Material Systems and Structures, 2009. **20**(18): p. 2223-2235.
 23. Tang, L. and Y. Yang, *A multiple-degree-of-freedom piezoelectric energy harvesting model*. Journal of Intelligent Material Systems and Structures, 2012. **23**(14): p. 1631-1647.
 24. Liu, J.-Q., et al., *A MEMS-based piezoelectric power generator array for vibration energy harvesting*. Microelectronics Journal, 2008. **39**(5): p. 802-806.
 25. Huan, X., H. Yuantai, and W. Qing-Ming, *Broadband piezoelectric energy harvesting devices using multiple bimorphs with different operating frequencies*. Ultrasonics, Ferroelectrics, and Frequency Control, IEEE Transactions on, 2008. **55**(9): p. 2104-2108.
 26. Lars-Cyril Julin Blystad, E.H.a.S.H., *Simulation of a MEMS Piezoelectric Energy Harvester Including Power Conditioning And Mechanical Stoppers*. Proceedings of PowerMEMS 2008+ microEMS2008, 2008.
 27. Giusa, F., et al., *"Random Mechanical Switching Harvesting on Inductor": A novel approach to collect and store energy from weak random vibrations with zero voltage threshold*. Sensors and Actuators A: Physical, 2013. **198**: p. 35-45.
 28. Liu, H., et al., *Investigation of a MEMS piezoelectric energy harvester system with a frequency-widened-bandwidth mechanism introduced by mechanical*

- stoppers*. Smart Materials and Structures, 2012. **21**(3): p. 035005.
29. Soliman, M., et al., *A wideband vibration-based energy harvester*. Journal of Micromechanics and Microengineering, 2008. **18**(11): p. 115021.
 30. Liu, H., et al., *Piezoelectric MEMS-based wideband energy harvesting systems using a frequency-up-conversion cantilever stopper*. Sensors and Actuators A: Physical, 2012. **186**(Supplement C): p. 242-248.
 31. Ferrari, M., et al., *Improved energy harvesting from wideband vibrations by nonlinear piezoelectric converters*. Sensors and Actuators A: Physical, 2010. **162**(2): p. 425-431.
 32. Ando, B., et al., *Nonlinear mechanism in MEMS devices for energy harvesting applications*. Journal of Micromechanics and Microengineering, 2010. **20**(12): p. 125020.
 33. Liu, W., et al., *Self-powered nonlinear harvesting circuit with a mechanical switch structure for a bistable generator with stoppers*. Sensors and Actuators A: Physical, 2014. **216**(Supplement C): p. 106-115.
 34. Liu, W.Q., et al., *Novel piezoelectric bistable oscillator architecture for wideband vibration energy harvesting*. Smart Materials and Structures, 2013. **22**(3): p. 035013.
 35. Mann, B.P. and B.A. Owens, *Investigations of a nonlinear energy harvester with a bistable potential well*. Journal of Sound and Vibration, 2010. **329**(9): p. 1215-1226.
 36. Harne, R.L. and K.W. Wang, *A review of the recent research on vibration energy harvesting via bistable systems*. Smart Materials and Structures, 2013. **22**(2): p. 023001.
 37. Jang, S.-J., et al., *Design of a 2DOF Vibrational Energy Harvesting Device*. Journal of Intelligent Material Systems and Structures, 2011. **22**(5): p. 443-448.
 38. Kim, I.-H., et al., *Broadband energy-harvesting using a two degree-of-freedom vibrating body*. Applied Physics Letters, 2011. **98**(21): p. 214102.
 39. Xiao, H., X. Wang, and S. John, *A multi-degree of freedom piezoelectric vibration energy harvester with piezoelectric elements inserted between two nearby oscillators*. Mechanical Systems and Signal Processing, 2016. **68**(Supplement C): p. 138-154.
 40. Wang, H.-y., et al., *A 2DOF hybrid energy harvester based on combined piezoelectric and electromagnetic conversion mechanisms*. Journal of Zhejiang University SCIENCE A, 2014. **15**(9): p. 711-722.
 41. Zhu, Y., S. Moheimani, and M. Yuce. *A 2-DOF wideband electrostatic transducer for energy harvesting and implantable applications*. in *Sensors, 2009 IEEE*. 2009. IEEE.

42. Cornwell, P., et al., *Enhancing power harvesting using a tuned auxiliary structure*. Journal of Intelligent Material Systems and Structures, 2005. **16**(10): p. 825-834.
43. Wu, H., et al., *Development of a broadband nonlinear two-degree-of-freedom piezoelectric energy harvester*. Journal of Intelligent Material Systems and Structures, 2014. **25**(14): p. 1875-1889.
44. Wu, H., et al., *A novel two-degrees-of-freedom piezoelectric energy harvester*. Journal of Intelligent Material Systems and Structures, 2013. **24**(3): p. 357-368.
45. Shih, Y.S., *Design and Fabrication of Piezoelectric MEMS Generator Based on Stainless Steel Substrates*, in *Engineering Science and Ocean Engineering*. 2012, National Taiwan University. p. 1-85.
46. Tao, K., et al., *A novel two-degree-of-freedom MEMS electromagnetic vibration energy harvester*. Journal of Micromechanics and Microengineering, 2016. **26**(3): p. 035020.
47. Kulah, H. and K. Najafi, *Energy scavenging from low-frequency vibrations by using frequency up-conversion for wireless sensor applications*. IEEE Sensors Journal, 2008. **8**(3): p. 261-268.
48. Lee, D.G., et al. *Novel Micro Vibration Energy Harvesting Device using Frequency Up Conversion*. in *Solid-State Sensors, Actuators and Microsystems Conference, 2007. TRANSDUCERS 2007. International*. 2007.
49. Wickenheiser, A.M. and E. Garcia, *Broadband vibration-based energy harvesting improvement through frequency up-conversion by magnetic excitation*. Smart Materials and Structures, 2010. **19**(6): p. 065020.
50. Peters, C., et al., *A closed-loop wide-range tunable mechanical resonator for energy harvesting systems*. Journal of Micromechanics and Microengineering, 2009. **19**(9): p. 094004.
51. Roundy, S. and Y. Zhang. *Toward self-tuning adaptive vibration-based microgenerators*. in *Proc. SPIE*. 2004.
52. Wu, X., et al., *A frequency adjustable vibration energy harvester*. Proceedings of PowerMEMS, 2008: p. 245-248.
53. Eichhorn, C., F. Goldschmidtboeing, and P. Woias, *Bidirectional frequency tuning of a piezoelectric energy converter based on a cantilever beam*. Journal of Micromechanics and Microengineering, 2009. **19**(9): p. 094006.
54. Leland, E.S. and P.K. Wright, *Resonance tuning of piezoelectric vibration energy scavenging generators using compressive axial preload*. Smart Materials and Structures, 2006. **15**(5): p. 1413.
55. Vinod, R.C., et al., *A vibration energy harvesting device with bidirectional resonance frequency tunability*. Smart Materials and Structures, 2008. **17**(1): p. 015035.

56. Zhu, D., et al., *Closed loop frequency tuning of a vibration-based micro-generator*. 2008.
57. Aboulfotouh, N.A., M.H. Arafa, and S.M. Megahed, *A self-tuning resonator for vibration energy harvesting*. *Sensors and Actuators A: Physical*, 2013. **201**: p. 328-334.
58. Xu, Z., et al., *A Novel Tunable Multi-Frequency Hybrid Vibration Energy Harvester Using Piezoelectric and Electromagnetic Conversion Mechanisms*. *Applied Sciences*, 2016. **6**(1): p. 10.
59. Lesieutre, G.A., G.K. Ottman, and H.F. Hofmann, *Damping as a result of piezoelectric energy harvesting*. *Journal of Sound and Vibration*, 2004. **269**(3): p. 991-1001.
60. Ottman, G.K., et al., *Adaptive piezoelectric energy harvesting circuit for wireless remote power supply*. *IEEE Transactions on power electronics*, 2002. **17**(5): p. 669-676.
61. Ottman, G.K., H.F. Hofmann, and G.A. Lesieutre, *Optimized piezoelectric energy harvesting circuit using step-down converter in discontinuous conduction mode*. *IEEE Transactions on Power Electronics*, 2003. **18**(2): p. 696-703.
62. Richard, C., et al. *Semi-passive damping using continuous switching of a piezoelectric device*. in *1999 Symposium on Smart Structures and Materials*. 1999. International Society for Optics and Photonics.
63. Guyomar, D., et al., *Toward energy harvesting using active materials and conversion improvement by nonlinear processing*. *IEEE transactions on ultrasonics, ferroelectrics, and frequency control*, 2005. **52**(4): p. 584-595.
64. Lefeuvre, E., et al., *A comparison between several vibration-powered piezoelectric generators for standalone systems*. *Sensors and Actuators A: Physical*, 2006. **126**(2): p. 405-416.
65. Lallart, M., et al., *High efficiency, wide load bandwidth piezoelectric energy scavenging by a hybrid nonlinear approach*. *Sensors and Actuators A: Physical*, 2011. **165**(2): p. 294-302.
66. Liang, J. and W.H. Liao, *Improved Design and Analysis of Self-Powered Synchronized Switch Interface Circuit for Piezoelectric Energy Harvesting Systems*. *IEEE Transactions on Industrial Electronics*, 2012. **59**(4): p. 1950-1960.
67. Lefeuvre, E., et al., *Piezoelectric energy harvesting device optimization by synchronous electric charge extraction*. *Journal of Intelligent Material Systems and Structures*, 2005. **16**(10): p. 865-876.
68. Wu, W., et al., *Modeling and experimental verification of synchronized discharging techniques for boosting power harvesting from piezoelectric transducers*. *Smart Materials and Structures*, 2009. **18**(5): p. 055012.

69. Lallart, M., et al., *Double synchronized switch harvesting (DSSH): A new energy harvesting scheme for efficient energy extraction*. IEEE transactions on ultrasonics, ferroelectrics, and frequency control, 2008. **55**(10).
70. Shen, H., et al., *Enhanced synchronized switch harvesting: a new energy harvesting scheme for efficient energy extraction*. Smart Materials and Structures, 2010. **19**(11): p. 115017.
71. Guyomar, D., et al., *Energy Harvesting from Ambient Vibrations and Heat*. Journal of Intelligent Material Systems and Structures, 2009. **20**(5): p. 609-624.
72. Richard, C., D. Guyomar, and E. Lefeuvre, *Self-powered electronic breaker with automatic switching by detecting maxima or minima of potential difference between its power electrodes*. FR2005/003000, publication number: WO/2007/063194, 2007.
73. Mickaël, L. and G. Daniel, *An optimized self-powered switching circuit for non-linear energy harvesting with low voltage output*. Smart Materials and Structures, 2008. **17**(3): p. 035030.
74. Lallart, M., et al., *Self-powered circuit for broadband, multimodal piezoelectric vibration control*. Sensors and Actuators A: Physical, 2008. **143**(2): p. 377-382.
75. Chen, C.H., et al. *A series-SSHI-Phi interface circuit for piezoelectric energy harvesting with 163% improvement in extracted power at off-resonance*. in *2016 IEEE Asian Solid-State Circuits Conference (A-SSCC)*. 2016.
76. Shen, H., et al., *Adaptive synchronized switch harvesting: A new piezoelectric energy harvesting scheme for wideband vibrations*. Sensors and Actuators A: Physical, 2015. **226**(Supplement C): p. 21-36.
77. Junrui, L. and L. Wei-Hsin. *An improved self-powered switching interface for piezoelectric energy harvesting*. in *Information and Automation, 2009. ICIA '09. International Conference on*. 2009.
78. Chen, Y.Y., et al. *Self-powered piezoelectric energy harvesting device using velocity control synchronized switching technique*. in *IECON 2010 - 36th Annual Conference on IEEE Industrial Electronics Society*. 2010.
79. Wu, Y., et al., *Nonlinear vibration energy harvesting device integrating mechanical stoppers used as synchronous mechanical switches*. Journal of Intelligent Material Systems and Structures, 2014. **25**(14): p. 1658-1663.
80. Liu, H., J. Liang, and C. Ge, *A mechatronic power boosting design for piezoelectric generators*. Applied Physics Letters, 2015. **107**(14): p. 141902.
81. Maiorca, F., et al., *Diode-less mechanical H-bridge rectifier for "zero threshold" vibration energy harvesters*. Sensors and Actuators A: Physical, 2013. **201**: p. 246-253.
82. Lien, I. and Y. Shu, *Array of piezoelectric energy harvesting by the equivalent*

- impedance approach*. Smart Materials and Structures, 2012. **21**(8): p. 082001.
83. Lin, H., et al., *Analysis of an array of piezoelectric energy harvesters connected in series*. Smart Materials and Structures, 2013. **22**(9): p. 094026.
 84. Chen, Y.-Y. and D. Vasic. *Energy harvesting of two cantilever beams structure: interfacing circuit discussion*. in *SPIE Smart Structures and Materials+ Nondestructive Evaluation and Health Monitoring*. 2015. International Society for Optics and Photonics.
 85. Richard, C., D. Guyomar, and E. Lefeuvre, *Self-powered electronic breaker with automatic switching by detecting maxima or minima of potential difference between its power electrodes*. 2007: FR.
 86. Lallart, M., et al., *Self-Powered Circuit for Broadband, Multimodal, Piezoelectric Vibration Control*. Sensors and Actuators A : Physical, 2008. **143**(2): p. 277-382.
 87. Junrui, L. and L. Wei-Hsin, *Improved Design and Analysis of Self-Powered Synchronized Switch Interface Circuit for Piezoelectric Energy Harvesting Systems*. Industrial Electronics, IEEE Transactions on, 2012. **59**(4): p. 1950-1960.
 88. Lallart, M., Y.-C. Wu, and D. Guyomar, *Switching delay effects on nonlinear piezoelectric energy harvesting techniques*. Industrial Electronics, IEEE Transactions on, 2012. **59**(1): p. 464-472.
 89. Electronics, M. *Basic Electrical Parameters of Reed Switch Products* 2016.
 90. Dongna, S., et al., *The design, fabrication and evaluation of a MEMS PZT cantilever with an integrated Si proof mass for vibration energy harvesting*. Journal of Micromechanics and Microengineering, 2008. **18**(5): p. 055017.
 91. Liu, H., et al., *Piezoelectric MEMS Energy Harvester for Low-Frequency Vibrations With Wideband Operation Range and Steadily Increased Output Power*. Journal of Microelectromechanical Systems, 2011. **20**(5): p. 1131-1142.
 92. Roundy, S. and P.K. Wright, *A piezoelectric vibration based generator for wireless electronics*. Smart Materials and Structures, 2004. **13**(5): p. 1131.
 93. Lee, B.S., et al., *Piezoelectric MEMS generators fabricated with an aerosol deposition PZT thin film*. Journal of Micromechanics and Microengineering, 2009. **19**(6): p. 065014.
 94. Shun-Chiu, L. and W. Wen-Jong, *Piezoelectric micro energy harvesters based on stainless-steel substrates*. Smart Materials and Structures, 2013. **22**(4): p. 045016.
 95. Ya Shan Shih, P.L.W., Dejan Vasic, and Wen Jong Wu, *Implementing Micro Piezoelectric Synchronized Switched Harvesting with Reed Switch*, in *International Conference on Adaptive Structures and Technologies*. 2016: Lake George, NY, USA.

96. Y.Y. Chen, D.V., Y.P. Liu, F. Costa, *Study of a Piezoelectric Switching Circuits for Energy Harvesting with Bistable Broadband Technique by Work-cycle Analysis*. *Journal of Intelligent Materials Systems & Structures*, 2013. **24**(2): p. 180-193.